Method development for scanning electrochemical microscopy and its application for material characterization

Dissertation

Zur Erlangung des Doktorgrades der Naturwissenschaften (Dr. rer. nat.)
der Fakultät für Chemie und Pharmazie
der Universität Regensburg

vorgelegt von

Christian Iffelsberger

aus Münsing

14. Juni 2018

Die vorgelegte Dissertation entstand in der Zeit von Juni 2014 bis Juni 2018 am Institut für Analytische Chemie, Chemo- und Biosensorik der naturwissenschaftlichen Fakultät IV-Chemie und Pharmazie - der Universität Regensburg.

Die Arbeit wurde angeleitet von: Prof. Dr. Frank-Michael Matysik
Das Promotionsgesuch wurde eingereicht am: 14. Juni 2018

Termin des Kolloquiums: 27. Juli 2018

Dem Prüfungsausschuss saß Prof. Dr. Arno Pfitzner vor. Erstgutachter war Prof. Dr. Frank-Michael Matysik, Zweitgutachter war Assoc. Prof. RNDr. Vlastimil Vyskočil, Ph.D. und Drittprüfer war PD Dr. Hans-Heiner Gorris.

Für meine Eltern

Ich danke allen Personen, die mich auf dem Weg zur Promotion begleitet und unterstützt haben. Danke, für die stete Förderung und die vielen Diskussionen in allen Lebenslagen!

List of content

List of publications

Peer reviewed articles

Imaging of localized enzymatic peroxidase activity over unbiased individual gold nanowires by scanning electrochemical microscopy

Preety Vatsyayan, Christian Iffelsberger, Carmen C. Mayorga-Martinez and Frank-Michael Matysik,
Analytical Methods 8 (2016) 6847-6855

Abstract

Scanning electrochemical microscopy (SECM) in constant-height mode was used to image individual gold nanowires (AuNWs, 2-3 μm long and ~140 nm diameter). High-resolution negative and positive feedback current images of individual AuNWs immobilized on glass and gold-coated glass slides, respectively were recorded with a Wollaston-based platinum disk ultramicroelectrode (UME) of radius 300 nm at 0.3 V probe potential using ferrocene methanol as mediator. The negative and positive feedback current responses were dependent on the effective recycling of mediator on the unbiased AuNWs.

Scanning electrochemical microscopy with forced convection introduced by high-precision stirring

Christian Iffelsberger, Preety Vatsyayan and Frank-Michael Matysik,
Analytical Chemistry 89 (2017) 1658–1664

Abstract

In the present report the well-known advantages of hydrodynamic mass transport in electrochemical systems are used in combination with scanning electrochemical microscopy (SECM). The hydrodynamic SECM system integrates a high-precision stirring device into the experimental setup. The well-defined stirring of the SECM electrolyte results in steady-state diffusion layer characteristics in the vicinity of large substrate electrodes operated in

chronoamperometric measuring mode. For a range of rotation frequencies of a rotating cylinder the thickness and the stability of the diffusion layer was studied by hydrodynamic SECM in the substrate generation/tip collection (SG/TC) as well as in the competition mode using ferrocene methanol as redox mediator. Different UME probe dimensions ranging from Pt diameters of 20 µm down to 0.6 µm were used. The smallest probe with 0.6 µm electrode diameter was found most suitable for these studies due to the almost convection-independent amperometric response associated with sub-µm electrodes. Additionally, preliminary studies of hydrodynamic SECM imaging of a 2 mm Pt disk electrode surface in the SG/TC mode based on in-situ produced hydrogen as mediator are presented. Comparative images measured in the conventional positive feedback mode in quiescent solution show that hydrodynamic SECM offers attractive complementary information.

Development and characterization of electrochemical flow cells for hydrodynamic scanning electrochemical microscopy

Timo Raith, Stefan Wert, Christian Iffelsberger and Frank-Michael Matysik

Accepted for publication.

Monatshefte für Chemie (Chemical Monthly).

Abstract

In the frame of the contribution, the effects of forced convection on scanning electrochemical microscopy (SECM) experiments are presented. The convection is generated by a flow of the mediator solution through electrochemical flow cells, developed especially for this purpose. A description of the mandatory design aspects of the experimental flow cell setups is included.

Using a macroscopic working electrode, the flow of the SECM electrolyte leads to the formation of a stable diffusion layer during chronoamperometric measurements in contrast to a growing diffusion layer in quiescent solution. To characterize the effects of the forced convection, the diffusion layer around an inserted platinum substrate electrode was investigated utilizing chronoamperometric measurements and hydrodynamic SECM imaging. Mathematical simulations using COMSOL Multiphysics were computed in order

to investigate the flow profile generated by the flowing mediator solution in the area of the substrate electrode. The flow profile predicted by the simulations was compared to probe line scans in feedback mode.

In summary, two different cell design prototypes of an electrochemical flow cell for SECM were developed and characterized. Both enable steady-state diffusion layer characteristics at a macroscopic working electrode offering interesting possibilities for future applications.

Detection and imaging of reactive oxygen species associated with the electrochemical oxygen evolution by hydrodynamic scanning electrochemical microscopy

Christian Iffelsberger, Timo Raith, Preety Vatsyayan, Vlastimil Vyskočil and Frank-Michael Matysik

Electrochimica Acta 281 (2018) 494-501

Abstract

Hydrodynamic scanning electrochemical microscopy (SECM) was applied for the characterization of Pt and boron-doped diamond (BDD) macroelectrodes operated in a potential region producing reactive oxygen species (ROS) during oxygen evolution reaction (OER). Forced convection introduced by high-precision stirring enabled the formation of a stable diffusion layer of electrochemically produced species and tip-substrate voltammetry was used for the detection of different ROS species produced during OER at BDD. Hydrodynamic SECM imaging in substrate generation/tip collection mode revealed local differences in the production of the ROS species across the BDD electrode surface.

Complementary analytical imaging techniques for the characterization of pretreated carbon fiber reinforced plastics

Stefan Viehbeck, Christian Iffelsberger and Frank-Michael Matysik

Composite Part A 113 (2018) 32–39

Abstract

In this work the complementary characterization of pretreatment techniques for adhesive bonding of carbon fiber reinforced plastics (CFRP) is presented. Industrial CFRP plates were

pretreated with laser, plasma and corundum blasting abrasive techniques followed by chemical activation. The combined use of atomic force microscopy and chemical force microscopy enabled the characterization of the surface morphology and the specific adhesion force between a chemically functionalized cantilever and the pretreated surfaces simulating the adhesive bond. Complementary measurements with scanning electrochemical microscopy and X-ray photoelectron spectroscopy supported the experimental findings and delivered additional information about the chemical structure of the surfaces. A comparison of experimental data of mechanical tensile shear strength measurements and the applied analytical methods revealed a valid correlation of microscopic and macroscopic techniques.

Non-Peer reviewed article

Trends in der elektrochemischen Rastermikroskopie

Christian Iffelsberger, Timo Raith, Patrick J. Hanekamp, Preety Vatsayayan und Frank-Michael Matysik, chrom+food FORUM 4 (2017) 20-22

Conference contributions

Oral presentations

ANAKON 2017, 3.-6.4.2017, Tübingen

Scanning electrochemical microscopy with forced convection introduced by high-precision stirring

Christian Iffelsberger and Frank-Michael Matysik

In electroanalytical chemistry, the introduction of forced convection into the electrochemical system is a common and elegant way of enhancing the analytical performance. It gives a lot of advantages such as a quickly attained steady state, a greater current or a higher precision. In the past, several techniques and methods for the convective mass transport were developed. These methods are often called hydrodynamic methods. [1]

Scanning electrochemical microscopic (SECM) measurements are usually performed in a static solution with the movement of the probe as the only origin for convection [2]. The absence of forced convection can be a serious limitation in several experimental studies, for example using the so-called substrate generation/tip collection (SG/TC) mode. The growing diffusion layer above a potentiostatically controlled large substrate electrode results in poor reproducibility of tip collection SECM measurements. In order to overcome this limitation, we added a high precision stirrer to the electrochemical cell to establish a steady- state diffusion layer and to control the thickness of the diffusion layer of the substrate electrode.

In this contribution, we present the home-built set up for the hydrodynamic SECM and its experimental characterization, especially in the context of the shape of the steady-state diffusion layers with respect to the rotation speed of the stirrer. The hydrodynamic characteristics within the electrochemical cell are verified by computer simulation. The application of this novel technique for imaging of reactive chemical species will be included.

Literature:

[1] A.J. Bard, L.R. Faulkner, Electrochemical methods: Fundamentals and applications, Vol. 2. Wiley, New York, 1980.

[2] A.J. Bard, M.V. Mirkin, Scanning electrochemical microscopy, 2nd edition, CRC Press Boca Raton, 2012.

Electrochemistry 2016, 26.-28.9.2016, Goslar, Germany

Scanning electrochemical microscopy with forced convection

Christian Iffelsberger and Frank-Michael Matysik

In electroanalytical chemistry, the introduction of forced convection into the electrochemical system is a common and elegant way for enhancing the analytical performance. It is associated with advantages such as considerably increased mass transport under steady-state conditions. In the past, several techniques and methods for convective mass transport were developed. These methods are often called hydrodynamic methods [1].

Scanning electrochemical microscopic (SECM) measurements are usually performed in a static solution with the movement of the probe as the only origin for convection [2]. The absence of forced convection can be a serious limitation in several experimental studies, for example using the so-called substrate generation/tip collection (SG/TC) mode. The growing diffusion layer above a potentiostatically controlled large substrate electrode results in poor reproducibility of tip collection SECM measurements. In order to overcome this limitation, we added a high precision stirrer to the electrochemical cell to establish a steady-state diffusion layer and to control the thickness of the diffusion layer of the substrate electrode.

In this contribution, we present the home-built set up for the hydrodynamic SECM and its characterization. Highly reproducible SECM experiments under forced convection will be shown using SG/TC or competition measuring modes.

Literature:

[1] A.J. Bard, L.R. Faulkner, Electrochemical methods: fundamentals and applications. Vol. 2. Wiley, New York, 1980.

[2] C. Combellas, M. Fermigier, A. Fuchs, F. Kanoufi, Scanning electrochemical microscopy. Hydrodynamics generated by the motion of a scanning tip and its consequences on the tip current, Anal. Chem., 2005, 77, 7966-7975.

10. Interdisziplinäres Doktorandenseminar, 28.2-1.3 2016, Berlin

Scanning electrochemical microscopy for the characterization of micro-structured electrode surfaces

Christian Iffelsberger, Preety Vatsyayan and Frank-Michael Matysik

Scanning electrochemical microscopy (SECM) is a scanning probe technique where an ultramicroelectrode (UME) is used as probe to image the morphology and the chemical activity of a substrate by scanning across its surface. The technique is attractive for the investigation of the heterogeneity of electrochemically active electrode surfaces. In order to image electrode surfaces with a spatial resolution in the sub-µm range the careful preparation of small probes with comparable dimensions is required [1].

In this work we present our results using SECM in constant height mode as tool for the characterization of different micro-structured electrodes, like interdigitated thin film electrodes and carbon film electrodes [2]. To understand the overall context, a short overview of SECM instrumentation and principles is included.

Literature:

[1] S. Bergner, P. Vatsayayan, F.-M. Matysik, Recent advances in high resolution scanning electrochemical microscopy of living cells–a review, Anal. Chim. Acta, 2013, 775, 1-13.

[2] V. Vyskočil, J. Barek, Voltammetric DNA biosensor based on a microcrystalline natural graphite–polystyrene composite transducer, Procedia Chemistry, 2012, 6, 52–59.

Poster presentations

11th Biosensors & Bioanalytical Microtechniques in Environmental, Food & Clinical Analysis (BBMEC), 26.-30.9.2015, Regensburg, Germany

PbO_2 modified screen-printed titanium as a novel electrode material for bioanalytical studies

Christian Iffelsberger, Marija Grundmann, Vlastimil Vyskočil and Frank-Michael Matysik

ANAKON 2015, 23.-26.3 2015, Graz, Austria

PbO_2 modified screen-printed titanium as a novel electrode material for bioanalytical studies

Christian Iffelsberger, Marija Grundmann, Vlastimil Vyskočil and Frank-Michael Matysik

Electrochemistry 2014, 22-24.9 2014, Mainz, Germany

High-resolution scanning electrochemical microscopy for the characterization of electrode structures

Christian Iffelsberger and Frank-Michael Matysik

15th International Conference on Electroanalysis (ESEAC), 2014, 11–15.6.2014, Malmö, Sweden

High-resolution scanning electrochemical microscopy for the characterization of thin and thick film electrode materials

Christian Iffelsberger, Vlastimil Vyskočil, Jiri Barek and Frank-Michael Matysik

Declaration of collaborations

Most of the theoretical and experimental works presented in this thesis were carried out solely by the author. Some of the results, however, were obtained in collaboration with other researchers and individuals. In accordance with § 8 Abs. 1 Satz 2 Punkt 7 of the Ordnung zum Erwerb des akademischen Grades eines Doktors der Naturwissenschaften (Dr. rer. nat.) an der Universität Regensburg vom 18. Juni 2009, this section details the nature of these collaborations. The following list describes these collaborations in the sequence of their appearance in this thesis.

4.1 UME characterization

Wollaston-based UMEs were fabricated and characterized in collaboration with Preety Vatsyayan. Focused ion beam milling, SEM imaging and PAC fitting was done in collaboration with Patrick J. Hanekamp. All other work steps of the UME fabrication and characterization was solely performed by the author.

4.2 Scanning Electrochemical Microscopy with Forced Convection Introduced by High-Precision Stirring

The experimental work was solely performed by the author. Preety Vatsyayan was involved with discussions. The work was done under supervision of Prof. Dr. Frank-Michael Matysik.

4.3. Numerical simulation and characterization of the convection for hydrodynamic scanning electrochemical microscopy

Numerical simulations were carried out solely by the author. Moritz Wetzel performed the electrochemical measurements under the guidance of the author.

4.4 Detection and imaging of reactive oxygen species associated with the electrochemical oxygen evolution by hydrodynamic scanning electrochemical microscopy

Timo Raith, Preety Vatsyayan and Vlastimil Vyskočil were involved with discussions and with writing. The artwork was done in collaboration with Thomas Herl. Scanning electron

microscopy was performed in collaboration with Korbinian Pürckhauer. All other experimental work was solely performed by the author. The work was done under supervision of Prof. Dr. Frank-Michael Matysik.

4.5 Imaging of localized enzymatic peroxidase activity over unbiased individual gold nanowires by scanning electrochemical microscopy

The experimental work and writing were carried out in collaboration with Preety Vatsyayan. Gold nanowires were synthesized and characterized by Carmen C. Mayorga-Martinez with support from Professor Merkoçi research group (Catalan Institute of Nanotechnology, Barcelona, Spain). The work was done under supervision of Prof. Dr. Frank-Michael Matysik.

4.6 Complementary analytical imaging techniques for the characterization of pretreated carbon fiber reinforced plastics

Experimental work including AFM, CFM, XPS, macroscopic tests and optical microscopy was done in collaboration with Stefan Viehbeck. The measurements and experiments with the SECM were done solely by the author. Stefan Viehbeck and the author contributed equally towards the conception of the project, sample preparation and writing. The work was done under supervision and guidance of Prof. Dr. Frank-Michael Matysik.

List of abbreviations

Abbreviation	Meaning	Value /unit
A	Electrode area	[m^2]
a	Electrode radius	[m]
a_i	Activity of species i	
AFM	Atomic force microscopy	
AuNP	Gold-nanoparticle	
AuNW	Gold-nanowire	
BDD	Boron-doped diamond	
C	Capacity	[F]
CE	Counter electrode	
CFRP	Carbon fiber reinforced plastic	
CFM	Chemical force microscopy	
c	Concentration	[mol L^{-1} = M]
CV	Cyclic voltammetry	
d	Tip-to-substrate distance	[m]
D	Diffusions coefficient	[cm^2 s^{-1}]
DC	Dual current	
DNA	Desoxyribonucleic acid	
E	Potential	[V]
E^0	Standard potential	[V]
$E^{0'}$	Formal standard potential	[V]
e^-	Electron	
e	elementary charge	[1.60218 $\cdot 10^{-19}$ C]
EDC	N-(3-Dimethylaminopropyl)-N'-ethylcarbodimide hydrochloride	
E_{start}	Starting potential	[V]
E_{vertex}	Vertex potential	[V]
F	Faraday constant	[9.64853$\cdot 10^{-4}$ C mol^{-1}]
FcMeOH	Ferrocene methanol (Hydroxymethylferrocene)	
$FcMeOH^+$	oxidized species of ferrocene methanol	
FIB	Focused ion beam	
Fig.	Figure	
f_{rot}	Rotational speed	[s^{-1}]
F_v	Volume force vector	[N]
HRP	Horseradish peroxidase	
I	Current	[A]
I_M	Measured current	[A]
I_∞	Current measured in bulk phase	[A]
i	a) Index for certain species	

	b) Unit vector	
I_C	Non-Faradaic current	[A]
I_D	Mass transport limited current	[A]
I_F	Faradaic current	[A]
I_l	Diffusion limited current	[A]
I_L	Limiting current	[A]
ID	Inner diameter	[m]
J	Flux	[mol cm^{-2} s^{-1}]
k	a) Reaction rate	[mol $m^{-2}s^{-1}$]
	b) Unit vector	
k_r	Electrochemical reaction rate	[mol s^{-1}]
l	Unit vector	
L	Normalized tip-to-substrate distance	
MPTES	(3-mercaptopropyl)triethoxysilane	
n	Amount of substance	[mol]
N	Number of repetitions	
NHE	Normal hydrogen electrode	
NHS	N-hydroxysuccinimide	
O	oxidized species	
N_I	Normalized feedback current	
OD	Outer diameter	
OER	Oxygen evolution reaction	
PAC	Probe approach curve	
PEEK	Polyether ether ketone	
PTFE	Polytetrafluoroethylene	
Q	Charge	[C]
R	a) Universal gas constant	[8.31447 J mol^{-1} K^{-1}]
	b) Resistance	[Ω]
	c) Reduced species	
RE	Reference electrode	
r_g	Radius of ultramicroelectrode tip	[m]
RRDE	Rotating ring disc electrode	
ROS	Reactive oxygen species	
SECM	Scanning electrochemical microscope	
SECCM	Scanning electrochemical cell microscope	
SEM	Scanning electron microscope	
SG/TC	Substrate generation/tip collection mode	
SHE	Standard hydrogen electrode	
SPB	Sodium phosphate buffer	
T	Temperature	[K]
t	Time	[s]
TEM	Transmissions electron microscopy	

TG/SC	Tip generation/substrate collection	
ToF-SIMS	Time of flight-secondary ion mass spectrometry	
TSV	Tip-substrate voltammetry	
u	Velocity vector	[m s^{-1}]
UME	Ultramicroelectrode	
WE	Working electrode	
XPS	X-ray photoelectron spectroscopy	
X, Y, Z	Axis in three-dimensional Cartesian space	
x, y, z	Distances in three-dimensional Cartesian space	[m]
z	Stochiometric number	
β	Correction function	
δ	Diffusion layer thickness	[m]
μ	a) Chemical potential	
	b) Dynamic viscosity	[Pa s]
υ	Flow velocity	[m s^{-1}]
υ_A	Velocity of the stirrer surface	[m s^{-1}]
ρ	Fluid density	[kg m^{-3}]
ϕ	Electric potential	[V]

1. Introduction

The scanning electrochemical microscope (SECM) was developed by Bard and coworkers in the late 80's. It is a scanning probe technique where a small electrode is used as probe [1,2]. Since then it has evolved to a versatile and powerful electroanalytical tool [3]. Today SECM has many applications in biology, material science and for kinetic studies of chemical reactions [3–5]. It is used to generate images which provide analytical information on the topography of the scanned substrate and its local (electro)chemical reactivities with a high resolution in a noninvasive way [6]. It is also used to characterize and modify surfaces and to study interactions of chemical compounds [6–10]. The substrate in SECM is usually fixed in an electrochemical cell and immersed in an electrolyte solution. The diversity of these substrates ranges from organic to inorganic materials [11], living cells or liquid/liquid interfaces to just name a few examples [11–17]. Analogous to other scanning probe techniques the local resolution depends on the size of the probe and ranges from tens of µm to a few nm in SECM [18–20].

Even though amperometry [6] is the commonly used measuring technique, SECM can be operated with a number of different electroanalytical techniques, like voltammetry [21], potentiometry [22] or by the use of an alternating current [22–26]. The versatility of the SECM is however reflected in the number of different modes of operation developed with time [27–31]. Some prominent examples of measuring modes are the feedback mode, the generation/collection mode and the redox competition mode. The feedback mode is the most common mode and is used for imaging the topography and electrochemical activity of the substrate [32]. The generation/collection mode includes a variety of experiments in which the signal mediating chemical species is generated in-situ at the substrate or the tip and respectively collected at the tip or the substrate at a diffusion-limited rate [33]. In the redox competition mode, the tip and the substrate compete for the same mediator species. This mode is used to study corrosion and the catalytic activity of a surface. In addition to recent developments in operational modes, continuous instrumental developments including novel probes, substrate holders, the precise control of environmental parameters like temperature or the surrounding atmosphere led to increased possible applications of the SECM [10,34–37]. The combination of the SECM with other techniques like atomic force microscopy (AFM), scanning ion

conductance microscopy, optical and fluorescence microscopy etc. increased the amount of accessible information obtained with SECM [38–45].

The priority of this work was the application of the SECM for studies involving the formation of highly reactive and unstable chemical species produced alongside the electrochemical solvent combustion at substrate electrodes of diameters greater than or equal to 2 mm. As a model system, the generation of reactive oxygen species (ROS) during the electrochemical oxygen evolution reaction (OER) in the substrate generation/tip collection mode was chosen. Preliminary studies identified the application of hydrodynamics as the most promising strategy to overcome the limitation of a transient signal caused by diffusion during imaging in the generation/collection mode. The application of forced convection to generate hydrodynamics in SECM required the construction of suitable experimental equipment in collaboration with the mechanical, electrical and glassware workshops of the University of Regensburg. The integration of these additional units into the present setup of SECM as well as the characterization of the effects of forced convection on the different measurement modes were an important part of this work. The progress of the project required a detailed characterization of the hydrodynamic conditions within the electrochemical cell with numerical simulations performed with COMSOL Multiphysics. The modified SECM was later used to study the evolution of ROS at macroscopic Pt and boron-doped diamond electrodes during OER. The classical application of the SECM to image and characterize novel materials was a second fundamental aspect which was also addressed in this work. For all objectives of this work the fabrication of high-quality ultramicroelectrodes was a prerequisite, thus a detailed account of the same is also included.

References

[1] J. Kwak, A.J. Bard, Scanning electrochemical microscopy. Apparatus and two-dimensional scans of conductive and insulating substrates, Anal. Chem. 61 (1989) 1794–1799.

[2] A.J. Bard, F.R. Fan, D.T. Pierce, P.R. Unwin, D.O. Wipf, F. Zhou, Chemical imaging of surfaces with the scanning electrochemical microscope., Science 254 (1991) 68–74.

[3] M.V. Mirkin, W. Nogala, J. Velmurugan, Y. Wang, Scanning electrochemical microscopy in the 21st century. Update 1: Five years after, Phys. Chem. Chem. Phys. 13 (2011) 21196–212.

[4] D. Polcari, P. Dauphin-Ducharme, J. Mauzeroll, Scanning electrochemical microscopy: A comprehensive review of experimental parameters from 1989 to 2015, Chem. Rev.

116 (2016) 13234–13278.
[5] S. Bergner, P. Vatsyayan, F.-M. Matysik, Recent advances in high resolution scanning electrochemical microscopy of living cells-a review, Anal. Chim. Acta 775 (2013) 1–13.
[6] A.J. Bard, M.V. Mirkin, Scanning electrochemical microscopy, 2nd edition,CRC Press, Boca Raton, 2012.
[7] T.J. Stockmann, J.-M. Noël, S. Ristori, C. Combellas, A. Abou-Hassan, F. Rossi, F. Kanoufi, Scanning electrochemical microscopy of Belousov–Zhabotinsky reaction: How confined oscillations reveal short lived radicals and auto-catalytic species, Anal. Chem. 87 (2015) 9621–9630.
[8] A. Fiorani, S. Rapino, G. Fioravanti, G. Valenti, M. Marcaccio, F. Paolucci, Local desorption of thiols by scanning electrochemical microscopy: patterning and tuning the reactivity of self-assembled monolayers, J. Solid State Electrochem. 20 (2016) 1037–1042.
[9] D. Zhan, L. Han, J. Zhang, Q. He, Z.-W. Tian, Z. Tian, Electrochemical micro/nano-machining: principles and practices, Chem. Soc. Rev. 46 (2017) 1526–1544.
[10] M. Zhou, Y. Yu, P. Blanchard, M.V. Mirkin, Surface patterning using diazonium ink filled nanopipette, Anal. Chem. 87 (2015) 10956–10962.
[11] S. Bergner, P. Palatzky, J. Wegener, F.-M. Matysik, High-resolution imaging of nanostructured Si/SiO_2 substrates and cell monolayers using scanning electrochemical microscopy, Electroanalysis 23 (2011) 196–200.
[12] E.R. Scott, H.S. White, J.B. Phipps, Scanning electrochemical microscopy of a porous membrane, J. Memb. Sci. 58 (1991) 71–87.
[13] S. Bergner, J. Wegener, F.-M. Matysik, Monitoring passive transport of redox mediators across a confluent cell monolayer with single-cell resolution by means of scanning electrochemical microscopy, Anal. Methods 4 (2012) 623–629.
[14] S. Bergner, J. Wegener, F.-M. Matysik, Simultaneous imaging and chemical attack of a single living cell within a confluent cell monolayer by means of scanning electrochemical microscopy, Anal. Chem. 83 (2011) 169–174.
[15] C. Wei, A.J. Bard, M.V. Mirkin, Scanning electrochemical microscopy. 31. Application of SECM to the study of charge transfer processes at the liquid/liquid interface, J. Phys. Chem. 99 (1995) 16033–16042.
[16] Y. Shao, M.V. Mirkin, Probing ion transfer at the liquid/liquid interface by scanning electrochemical microscopy (SECM), J. Phys. Chem. B. 102 (1998) 9915–9921.
[17] J.-M. Noël, Y. Yu, M.V. Mirkin, Dissolution of Pt at moderately negative potentials during oxygen reduction in water and organic media, Langmuir 29 (2013) 1346–1350.
[18] Y. Yu, Y. Gao, K. Hu, P.Y. Blanchard, J.M. Noël, T. Nareshkumar, K.L. Phani, G. Friedman, Y. Gogotsi, M.V. Mirkin, Electrochemistry and electrocatalysis at single gold nanoparticles attached to carbon nanoelectrodes, ChemElectroChem. 2 (2015) 58–63.
[19] M.A. Mezour, R. Cornut, E.M. Hussien, M. Morin, J. Mauzeroll, Detection of hydrogen peroxide produced during the oxygen reduction reaction at self-assembled thiol-porphyrin monolayers on gold using SECM and nanoelectrodes, Langmuir 26 (2010) 13000–13006.
[20] T. Sun, Y. Yu, B.J. Zacher, M.V. Mirkin, Scanning electrochemical microscopy of individual catalytic nanoparticles, Angew. Chem. Int. Ed. 53 (2014) 14120–14123.
[21] J.A. Koch, M.B. Baur, E.L. Woodall, J.E. Baur, Alternating current scanning electrochemical microscopy with simultaneous fast-scan cyclic voltammetry, Anal. Chem. 84 (2012) 9537–9543.
[22] A. Kiss, G. Nagy, New SECM scanning algorithms for improved potentiometric imaging

of circularly symmetric targets, Electrochim. Acta 119 (2014) 169–174.
[23] K. Eckhard, W. Schuhmann, Alternating current techniques in scanning electrochemical microscopy (AC-SECM), Analyst 133 (2008) 1486–97.
[24] D. Trinh, M. Keddam, X.R. Novoa, V. Vivier, Alternating-current measurements in scanning electrochemical microscopy, part 1: Principle and theory, ChemPhysChem. 12 (2011) 2169–2176.
[25] D. Filotás, B.M. Fernández-pérez, J. Izquierdo, A. Kiss, L. Nagy, G. Nagy, Improved potentiometric SECM imaging of galvanic corrosion reactions, Corros. Sci. 129 (2017) 136-145.
[26] D. Filotás, B.M. Fernández-Pérez, A. Kiss, L. Nagy, G. Nagy, R.M. Souto, Double barrel microelectrode assembly to prevent electrical field effects in potentiometric SECM imaging of galvanic corrosion processes, J. Electrochem. Soc. 165 (2018) C270–C277.
[27] K. Eckhard, X. Chen, F. Turcu, W. Schuhmann, Redox competition mode of scanning electrochemical microscopy (RC-SECM) for visualisation of local catalytic activity, Phys. Chem. Chem. Phys. 8 (2006) 5359–5365.
[28] C.M. Sánchez-Sánchez, J. Rodríguez-López, A.J. Bard, Quantitative calibration of the SECM substrate generation/tip collection mode and its use for the study of the oxygen reduction mechanism, Anal. Chem. 80 (2008) 3254–3260.
[29] J. Rodríguez-López, M.A. Alpuche-Avilés, A.J. Bard, Interrogation of surfaces for the quantification of adsorbed species on electrodes: Oxygen on gold and platinum in neutral media, J. Am. Chem. Soc. 130 (2008) 16985–16995.
[30] L. Stratmann, J. Clausmeyer, W. Schuhmann, Non-destructive patterning of carbon electrodes by using the direct mode of scanning electrochemical microscopy, ChemPhysChem. 16 (2015) 3477–3482.
[31] T. Sun, D. Wang, M.V. Mirkin, Tunneling mode of scanning electrochemical microscopy (SECM): Probing electrochemical processes at single nanoparticles, Angew. Chem. Int. Ed. 57 (2018) 7463–7467.
[32] J. Kwak, A.J. Bard, Scanning electrochemical microscopy. Theory of the feedback mode, Anal. Chem. 61 (1989) 1221–1227.
[33] R.D. Martin, P.R. Unwin, Theory and experiment for the substrate generation tip collection mode of the scanning electrochemical microscope: Application as an approach for measuring the diffusion coefficient ratio of a redox couple, Anal. Chem. 70 (1998) 276–284.
[34] J. Clausmeyer, D. Schäfer, M. Nebel, W. Schuhmann, Temperature-induced modulation of the sample position in scanning electrochemical microscopy, ChemElectroChem. 2 (2015) 946–948.
[35] P. Hanekamp, W. Robl, F.-M. Matysik, Development and application of a multipurpose electrodeposition cell configuration for studying plating processes on wafer specimen and for characterizing surface films by scanning electrochemical microscopy, J. Appl. Electrochem. 47 (2017) 1305–1312.
[36] W. Nogala, K. Szot, M. Burchardt, F. Roelfs, J. Rogalski, M. Opallo, G. Wittstock, Feedback mode SECM study of laccase and bilirubin oxidase immobilised in a sol–gel processed silicate film, Analyst 135 (2010) 2051–2058.
[37] D. Momotenko, F. Cortes-Salazar, A. Lesch, G. Wittstock, H.H. Girault, Microfluidic push-pull probe for scanning electrochemical microscopy, Anal. Chem. 83 (2011) 5275–5282.
[38] Y. Takahashi, H. Shiku, T. Murata, T. Yasukawa, T. Matsue, Transfected single-cell imaging by scanning electrochemical optical microscopy with shear force feedback

regulation, Anal. Chem. 81 (2009) 9674–9681.
[39] S. Szunerits, S.E. Pust, G. Wittstock, Multidimensional electrochemical imaging in materials science, Anal. Bioanal. Chem. 389 (2007) 1103–1120.
[40] C. Kranz, Recent advancements in nanoelectrodes and nanopipettes used in combined scanning electrochemical microscopy techniques, Analyst 139 (2014) 336–352.
[41] J. Velmurugan, A. Agrawal, S. An, E. Choudhary, V.A. Szalai, Fabrication of scanning electrochemical microscopy - atomic force microscopy probes to image surface topography and reactivity at the nanoscale, Anal. Chem. 89 (2017) 2687–2691.
[42] R. Hao, B. Zhang, Nanopipette-based electroplated nanoelectrodes, Anal. Chem. 88 (2016) 614–620.
[43] M. Şen, Y. Takahashi, Y. Matsumae, Y. Horiguchi, A. Kumatani, K. Ino, H. Shiku, T. Matsue, Improving the electrochemical imaging sensitivity of scanning electrochemical microscopy-scanning ion conductance microscopy by using electrochemical Pt deposition, Anal. Chem. 87 (2015) 3484–3489.
[44] P. Knittel, M.J. Higgins, C. Kranz, Nanoscopic polypyrrole AFM–SECM probes enabling force measurements under potential control, Nanoscale 6 (2014) 2255.
[45] H.V. Patten, S.C.S. Lai, J.V. MacPherson, P.R. Unwin, Active sites for outer-sphere, inner-sphere, and complex multistage electrochemical reactions at polycrystalline boron-doped diamond electrodes (pBDD) revealed with scanning electrochemical cell microscopy (SECCM), Anal. Chem. 84 (2012) 5427–5432.

2. Fundamentals

2.1 Electrochemical fundamentals

2.1.1 Electrochemical reaction

An electrochemical reaction can be described as a transfer of n numbers of electrons (e^-) between two chemical species. The reaction is located at the electrode/electrolyte interface and can be written as eq. 1. [1]

$$O + n \cdot e^- \rightleftharpoons R \tag{1}$$

The electron accepting species (*O*) gets reduced and the electron donating species (*R*) gets oxidized during the electrochemical reaction. The Nernst equation (eq. 2), delivers the relation of the potential *E* [V] of the *O/R*-system and the standard electrode potential E^0 as a function of the activities of oxidized species a_{Ox} and the reduced species a_{Red}. The standard electrode potential of an electrochemical reaction refers to the standard hydrogen electrode (SHE).

$$E = E^0 + \frac{RT}{zF} ln \frac{a_O}{a_R} \tag{2}$$

R is the ideal gas constant (*R*= 8.3145 J mol^{-1} K^{-1}), *T* is temperature [K], *z* is the stochiometric number of transferred electrons and *F* is the Faraday Constant. The Faraday constant gives the charge of one mole (N_a) elementary charges (*e*).

$$F = e \cdot N_a = 96485.3 \frac{C}{mol} \tag{3}$$

Since the activities of the considered species are often unknown, a formal standard potential $E^{0'}$ was introduced to use the bulk concentrations of the oxidized *[O]* and reduced species *[R]* instead of the activities. [1–3]

$$E = E^{0'} + \frac{RT}{zF} ln \frac{[O]}{[R]} \tag{4}$$

2.1.2 Current

The current *I* [A] is defined as change in charge *Q* [C] per time *t* [s].

$$I = \frac{dQ}{dt} \tag{5}$$

At an electrode, two types of processes contribute to *I* measured in an electrochemical cell. They are faradaic (I_F) and non-faradaic processes (I_C). The total measured current is the sum of both.

$$I = I_F + I_c \tag{6}$$

Faradaic processes are charge transfer processes governed by Faraday's law which correlates the charge passed through the electrochemical cell, to the amount of product n [mol] and the number of electrons transferred per reaction (z) during a chemical reaction.

$$Q = nFz \tag{7}$$

Non-faradaic processes summarize all processes that occur at the electrode excluding chemical reactions. Such processes follow Ohm's law however adsorption and desorption can occur, and the structure of the electrode/electrolyte interface, the so-called double layer, can change with changing potential or solution composition. The charging of the double layer can be described as charging of a capacitator with a capacity C_{dl} [F] and the conversion of a substance as Faraday-impedance $Z_{f.}$ Fig. 2.1 shows the equivalent circuit diagram of a schematic electrochemical cell.

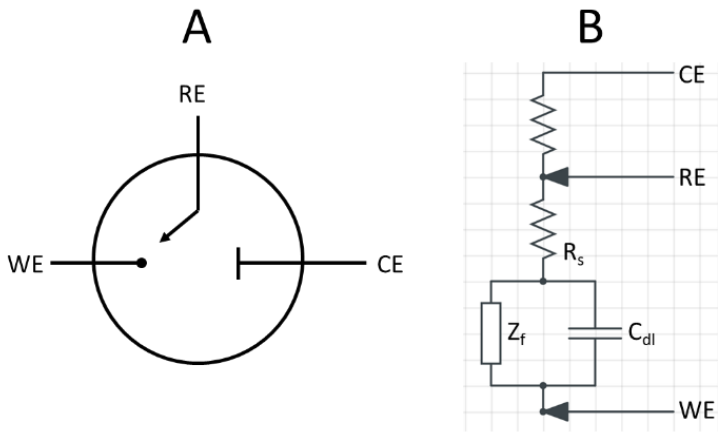

Figure 2.1: Schematic representation of the electrochemical cell (A) and the equivalent circuit diagram (B). R_s represents the ohmic resistance of the solution, Z_f the substance conversion as faraday-impedance and C_{dl} the capacitance of the electrode/electrolyte interface. Adapted from [1].

The resulting charging current I_c for a potential step at an electrode is transient with time and is described by eq. 8 where E is the applied potential, R_s [Ω] the ohmic resistance of the solution, t the time and C_{dl} the capacity of the electrode/electrolyte interface. [1,3]

$$I_c = \frac{E}{R_s} e^{-\frac{t}{R_s C_{dl}}} \tag{8}$$

2.1.3 Reaction rate

A homogenous reaction occurs everywhere within the medium at a uniform rate k [mol m^{-2} s^{-1}] given by the change of the amount of substance per time.

$$k = \frac{dn}{dt} \tag{9}$$

In contrast to a homogenous reaction, the electrochemical reaction is a heterogenous reaction located at the electrode surface with a finite surface area (A [m^2]). According to Faraday's law, the reaction rate of an electrochemical reaction k_r [mol s^{-1}] can be written as

$$k_r = \frac{dn}{dtA} = \frac{I}{zFA} \tag{10}$$

The potential-current curve for a Nernstian reaction (Fig. 2.2) shows the relationship between an applied potential and the reaction rate. Initially only the oxidant is present in solution. With increasing potential, the reaction starts until a complete conversion of the oxidant occurs and a limiting current I_L can be measured.

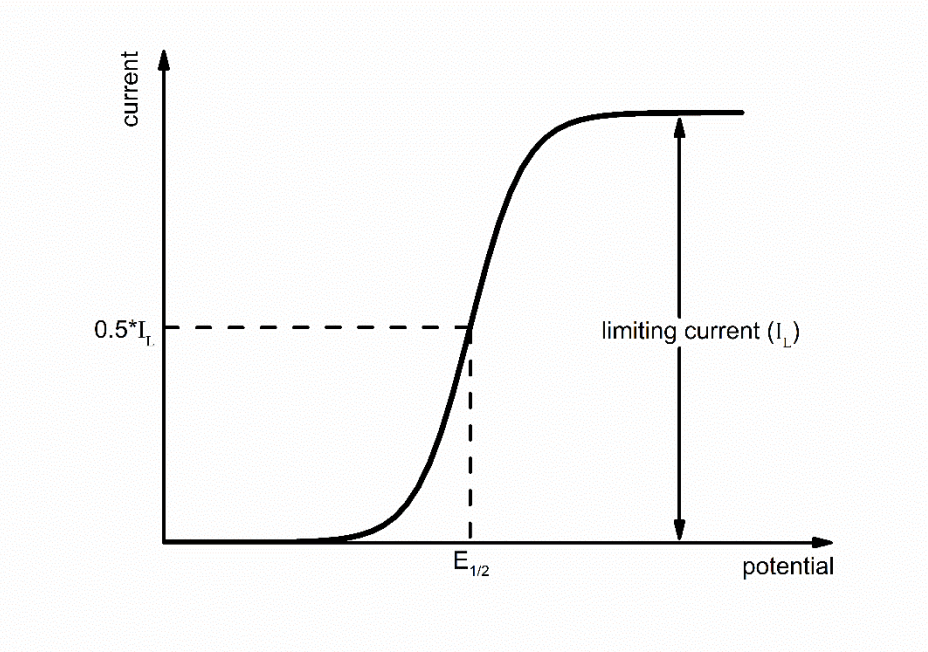

Figure 2.2: Current-potential curve for a Nernstian reaction with only one reactant present initially in solution. Adapted from [1].

The half-wave potential $E_{1/2}$ is independent of the concentration of the reactants and is characteristic for the specific O/R-system.[1,3]

2.1.4 Diffusion layer

As a consequence of an electrochemical reaction the concentration of the reactant changes at the electrode/electrolyte interface and forms a concentration gradient.

$$\frac{dc_i}{dx} = \frac{\left(c_i^* - c_i(x=0)\right)}{dx} \tag{11}$$

The difference of the concentration (dc_i) between the concentration in bulk solution (c_i^* [mol l^{-1} = M]) and the concentration at the electrode surface $c_i(x=0)$ reaches a certain distance (dx) into the bulk solution and forms a diffusion layer. The diffusion layer thickness depends on the time scale of the experiment as shown in Fig. 2.3 and the rate of the diffusion described by a proportionality factor called diffusion coefficient D [m^2 s^{-1}]. Even though the diffusion layer has no definite thickness it is useful to think about the diffusion layer thickness δ_i [m] it in terms of

$$dx = \delta_i = 2\sqrt{D_i t}. \tag{12}$$

With this equation the calculated distance contains the complete diffusion layer with an error of 0.005 [1]. For an experimental time of 1 ms, δ_i is about 2 µm and for 1s the layer has grown to 63 µm (with $D_i = 5 \cdot 10^{-9}$ m^2 s^{-1}). [1]

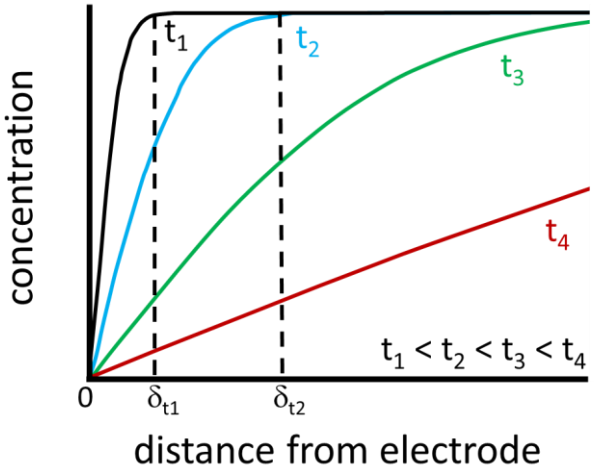

Figure 2.3: Schematic representation of concentration profiles for several times after the start of an electrochemical experiment. Adapted from [4].

2.1.5 Mass transport

If the other processes affecting the reaction rate (e.g.: rate of electron transfer, chemical reactions preceding or following or surface reactions like adsorption, desorption) are ignored then the reaction rate is proportional to the concentration gradient and only limited by the mass transport of the reactant towards the surface.

$$k_r \propto \frac{dc_i}{dx} \propto J_i(x) \tag{13}$$

The mass transport is the flux J_i of a mass or species i [mol s^{-1} m^{-2}] at a distance x from one compartment of the solution to another along the x axis. The mass transport is described by the Nernst-Planck equation (eq. 14) and is categorized into three modes. The flux arises from differences in electrical potential (migration), chemical potential (diffusion) and from the movement of a volume element of solution (convection).

$$J_i(x) = -D_i \frac{\partial c_i(x)}{\partial x} - \frac{z_j F}{RT} D_i c_i \frac{\partial \phi(x)}{\partial x} + c_i v(x) \quad (14)$$

D_i, c_i, ϕ, v are the diffusion coefficient, the concentration, the electric potential and the velocity, respectively. The first term of the Nernst-Planck equation represents the mass transport by diffusion along a concentration gradient. The second term describes the mass transport by migration. The third term describes the mass transport by convection. To simplify the mathematical solution of the Nernst-Planck equation electrochemical systems are designed to neglect one or two contributions to the mass transport. Migration can be neglected by the addition of an inert supporting electrolyte at much higher concentrations than the electroactive species and convection is avoided by preventing stirring and vibrations. Under such conditions the mass transport becomes diffusion limited. [1,5]

2.1.6 Diffusion limited electrochemical reaction

For a diffusion limited electrochemical reaction the reaction rate is given by the first term of the Nernst-Planck equation.

$$k_r = J_i(x) = D_i \frac{\partial c_i(x)}{\partial x} = D_i \frac{\left(c_i^* - c_i(x=0)\right)}{\delta_i} = m_i(c_i^* - c_i(x=0)) \quad (15)$$

Since the diffusion layer thickness is often unknown the combination of δ_i with the diffusion coefficient D_i to a single constant, called the mass transport coefficient m_i [m s^{-1}] is convenient.

$$m_i = \frac{D_i}{\delta_i} \quad (16)$$

In the case of a complete conversion of the reactant at the electrode its concentration at the electrode becomes $c_i(x = 0) = 0$ and the reaction rate is given by the product of the mass transport coefficient m_i and the concentration of the electrochemical active species in bulk solution c_i^*. The diffusion limited current I_l can be calculated with eq. 17.

$$I_l = nFAc_i^* m_i \quad (17)$$

In the defined system the mass transport is limited only by diffusion according to Fick's laws of diffusion. The first law describes the flux J of a species i [mol s^{-1} m^{-2}] as a function of the change in its concentration, with distance x from an electrode.

$$-J_i(x) = D_i \frac{\partial c_i(x)}{\partial x} \tag{18}$$

The second law relates the change in concentration with time, to the change in flux with position.

$$\frac{\partial c_j(x,t)}{\partial t} = D_j \frac{\partial^2 c_j(x,t)}{\partial x^2} \tag{19}$$

The solution of this equations for a potential step experiment results in the Cottrell equation (eq. 20).

$$I_l(t) = \frac{nFAD_i^{1/2} c_i^*}{\pi^{1/2} t^{1/2}} = nFAc_i^* \sqrt{\frac{D_i}{\pi t}} \tag{20}$$

To be valid the current must be diffusion limited and the potential step has to be large enough to ensure the rapid depletion of the electroactive species at the electrode surface. The Cottrell equation predicts the time dependent Faraday current of such potential step experiment and is often applied in chronoamperometry where the current is measured with time (Fig. 2.4A). The resulting graph (Fig. 2.4B) is called chronoamperogram.

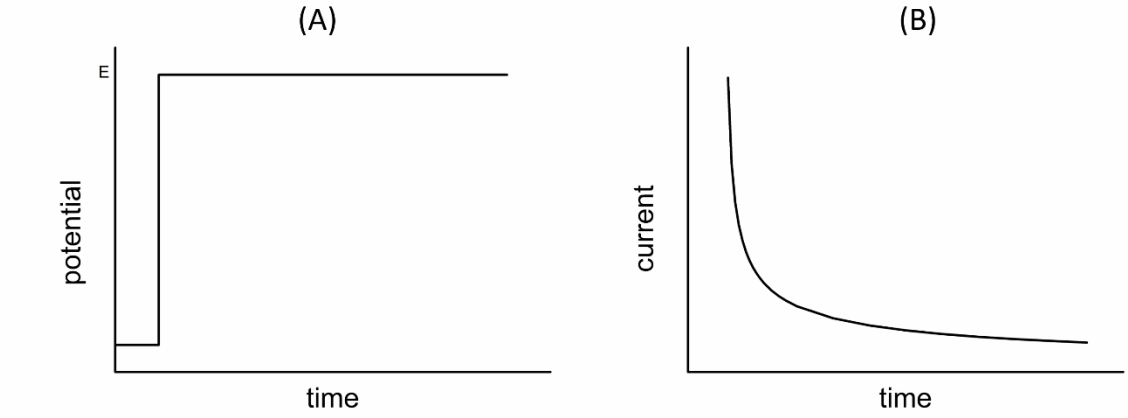

Figure 2.4: Schematic potential-time diagram of a chronoamperometric experiment (A) and the corresponding chronoamperogram (B). Adapted from [1]

The calculation of the diffusion-limited current according to eq. 20 gives the current resulting from planar diffusion neglecting radial diffusion at the electrode borders. For a disk shaped macroelectrode (electrode with dimensions in the mm or cm range) this simplification is valid because the electrode radius a [m] is much larger than the diffusion layer thickness. Disk shaped

ultramicroelectrodes (UME) may have an electrode radius smaller than the diffusion layer thickness with a predominantly radial diffusion as illustrated in Fig. 2.5.

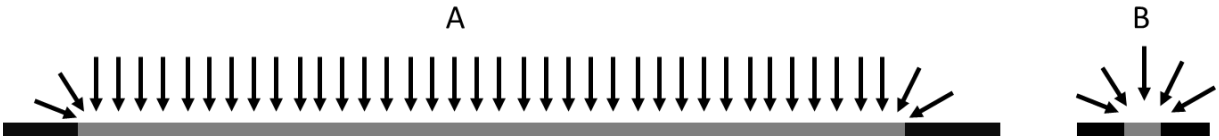

Figure 2.5: Comparison of the diffusion at a disk electrode with $a >> \delta_t$ (A) and at UME (B). Adapted from [5].

In voltammetry the current is measured depending on a changing potential. The potential-current plot is called voltammogram. In cyclic voltammetry the potential is swept as shown in Fig. 2.6A in a linear manner between the starting potential E_{start} and a second potential E_{vertex}. At E_{start} no reaction occurs so that the current flow is negligible. The potential E_{vertex} is set to a value at which the Faraday current is limited by diffusion. At E_{vertex} the direction of the scan is reversed and usually the potential is swept back to its original value. Typical CVs at a macroelectrode and a ultramicroelectrodes are shown in Fig. 2.6B and 2.6C, respectively.

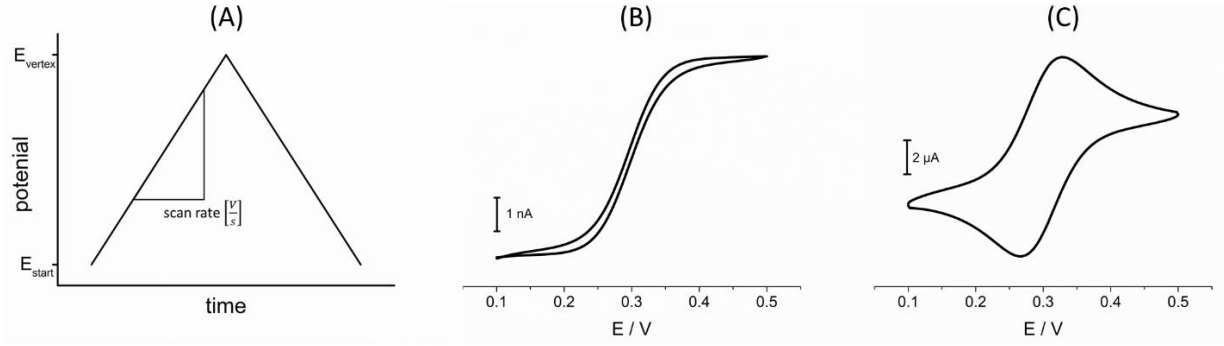

Figure 2.6: Schematic representation of the potential curve of a cyclic voltammetric experiment (A) and voltammograms of 1.5 mM FcMeOH in 0.2 M KNO_3 at a 25 µm diameter Pt disk UME (B) and a 2 mm diameter Pt disk electrode (C) (scan rate: 50 mV s^{-1}). Adapted from [5].

2.1.7 Electrochemical reaction with convection

For a mass transport limited electrochemical reaction with forced convection and added supporting electrolyte, the reaction rate is given by

$$J_i(x) = -D_i \frac{\partial c_i(x)}{\partial x} + c_i v(x) \tag{21}$$

There are several ways known to introduce forced convection into an electrochemical system. The most conventional ones are stirring the solution, rotating the electrode, sonication or electrochemical flow cells. Methods involving convective mass transport are called hydrodynamic methods. The advantages of hydrodynamic methods are a quickly attained steady-state current and a high precision in measurements. Furthermore, the rates of mass transport at the electrode surface are larger than the rates of diffusion alone. One disadvantage of hydrodynamic methods is that the construction of hydrodynamic electrodes and devices that provide known and reproducible mass transport conditions is difficult. Two different types of fluid flows are considered. An unsteady and chaotic motion, termed turbulent and a smooth and steady flow occurring as if separate layers (laminae) of the fluid have constant and characteristic velocities, termed laminar. The velocity profile under these conditions is typically parabolic. The slowest velocity is found at the solution/solid interface. Theoretical treatments of hydrodynamic situations are difficult and require modeling of the system and solving the problem numerically. The simplest treatment of a convective systems assumes that migration can be neglected, and that convection is ineffective at the electrode surface so that during an electrochemical reaction a diffusion layer with a constant thickness is formed. Within the diffusion layer no movement of the solution occurs, and a steady-state mass transport takes place. Figure 2.7 shows the current-time curve for a potential step experiment at a macroelectrode for different convective situations. The recorded steady-state current is the result of a constant mass transport. [1,5]

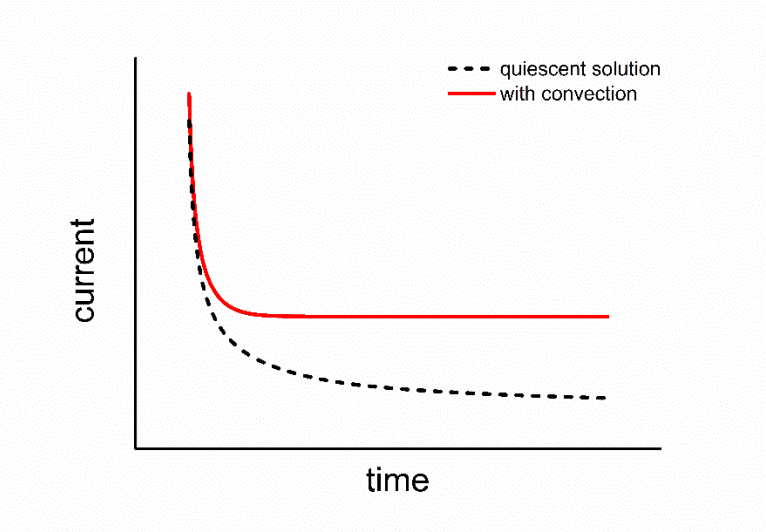

Figure 2.7: Chronoamperometry at a macroelectrode (2 mm diameter) without and with forced convection. Adapted from [1].

In most cases only the steady-state solutions of both hydrodynamic and electrochemical problems are desired. According to the empirical treatment of the steady-state mass transport the diffusion layer thickness can be calculated from the mass transport limited current (I_D) of chrono-amperometric recordings at macroelectrodes according eq. 22. [1]

$$\delta_i = \frac{nFADC}{I_D} \tag{22}$$

2.2 Scanning electrochemical microscope

The scanning electrochemical microscope (SECM) consists of several important components. The measurements are performed in an electrochemical cell, typically with a three or four electrode setup, as illustrated in Fig. 2.8. The applied potential refers always to a reference electrode (RE) and the electrical circuit is completed by a counter electrode (CE). In a three-electrode setup only the probe acts as working electrode. In a four-electrode setup, the substrate acts as second working electrode. The bipotentiostat is necessary to define and control the applied potentials as well as for data acquisition. To image a substrate the probe is positioned near its surface. In imaging experiments the probe is scanned across the substrate and the signal is recorded with respect to its position. The accurate three-dimensional positioning of the probe and the scanning is done with a stepper and/or a piezo positioner. The step width can range from few nm to several µm. Both, the movement of the probe and the data acquisition is controlled via PC. The acquired data is presented in 2- or 3-dimensional false color images. [6]

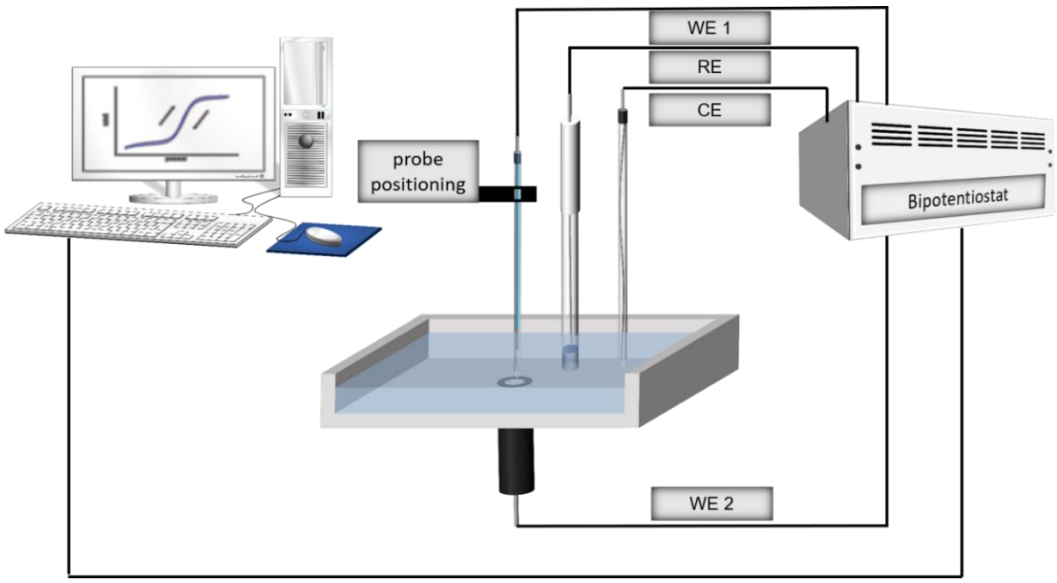

Figure 2.8: Schematic illustration of the instrumental SECM setup. Adapted from [7].

The measured signal depends on the used technique. In this work the SECM was operated using amperometry with a Faraday current of an electrochemical reaction occurring at the UME as measuring signal. This technique requires the presence of an electroactive species, a so-called mediator, in the solution. An ideal mediator is soluble, stable under experiment conditions and undergoes a fast, well-known and reversible one electron transfer reaction within the potential window of the used electrode material. [6]

2.3 Ultramicroelectrode

The probe used in SECM is an UME with at least one dimension in micrometer range. In literature the use of a variety of different electrode materials and designs for SECM experiments are reported [2,3,6]. UMEs used as SECM probes are commonly disk shaped with an electrode diameter of 25 µm diameter or smaller [8]. As electrode material noble metals (Pt, Au) or carbon-based materials are typically used. For the insulation of the electrodes often soda lime glass or SiO_2 is used. Even though SECM probes are commercially available and the fabrication remains difficult, it is still common to use self-fabricated UMEs. Many different methods and techniques for the fabrication of UMEs are described in literature [2,3,6]. A typical probe fabricated for the experimental work presented in this thesis is shown in Fig. 2.9. The UMEs generally consist of a thin Pt wire (25 µm) soldered onto a Cu wire. Both were inserted in a soda lime glass capillary tapered at one end. The Pt wire was insulated by melting the glass of the tapered end with a heating coil or a Bunsen burner. Since the coefficient of thermal expansion of soda lime glass and Pt are similar, this combination of materials delivers well insulated UMEs [9]. The insulation process is followed by a careful grinding and polishing of the tip to expose the metal disk and to shape the tip. The electrode diameter of such a probe is equal to the wire diameter. A prior reduction of the diameter of the wire for example by electrochemical etching of the end of the wire to form a sharp tip enables the fabrication of UMEs with electrode diameters of a few 100 nm [10–14]. A detailed description of the UME fabrication can be found in section 3.2.

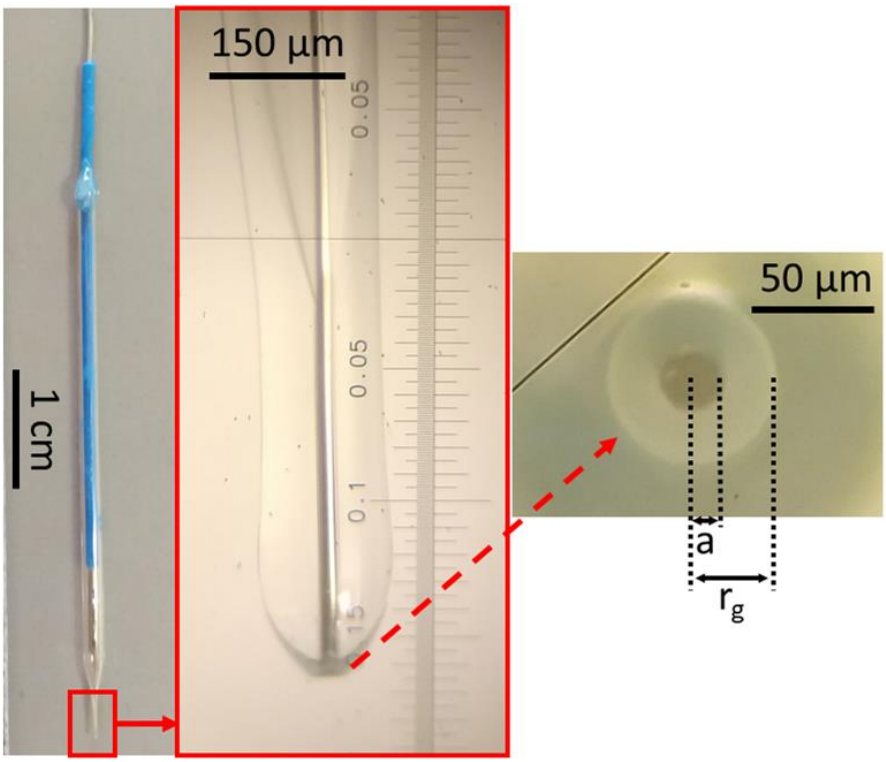

Figure 2.9: Schematic illustration of lab constructed UMEs to be used as SECM probes.

Two properties of the UMEs are of major importance for their application as SECM probes. The active electrode area and the thickness of the insulating sheet surrounding the electrode. The active electrode area is the critical value which affects the resolution of the SECM. For a disk-shaped UME, the active electrode area is given by *a* of the metal disk (Fig. 2.9). The second important property is represented by the *RG* value which characterizes the insulation sheath thickness relative to the electrode radius.

$$RG = \frac{r_g}{a} \tag{23}$$

The *RG* value is defined as the radius of the whole tip (electrode plus insulation, r_g) divided by the electrode radius [6]. For a disk UME with an electrode insulation of $RG > 10$ the steady-state current in the bulk phase (I_∞) can be calculated according

$$I_\infty = 4nFc_i^* D_i a. \tag{24}$$

Diffusion at UMEs with a thin insulation thicknesses ($RG < 10$) can also occur from behind the electrode surface resulting in a higher current as estimated by eq. 24. If the *RG* value is below 10 and the probe dimensions are exactly known, this can be compensated by multiplying the current with the function $\beta(RG)$. [6]

$$I_\infty = 4nFc_i^* D_i r \beta(RG) \tag{25}$$

Different expressions for $\beta(RG)$ can be found in literature [15–18]. Lefrou and Cornut suggested the following equation with a accuracy better than 0.3 % for $RG > 1.1$ [19]. The calculated values presented in table 2.1 show that only for very small *RG* values a significant effect is remarkable.

$$\beta(RG) = 1 + \frac{0.23}{(RG^3 - 0.81)^{0.36}} \tag{26}$$

Table 2.1: Values of $\beta(RG)$ calculated with eq. 26.

RG	50	20	10	7	6	5	4	3	2	1.5	1
β(RG)	1.00	1.01	1.03	1.04	1.05	1.06	1.07	1.10	1.16	1.23	1.58

As shown by Amphlett and Denuault the *RG* value influences the electrochemical contrast [20]. At small *RG* values, the diffusion of mediator species from behind the electrode increases the electrochemical contrast. Another aspect of the *RG* value for SECM imaging is the ability to approach and scan the UME as close as possible across the substrate without crashing the UME into it. The working distance is usually one to two electrode radii depending on the roughness and the tilt of the substrate. Since the fabrication of UMEs with small RG values is challenging as compromise a *RG* value between 2 to 10 was recommended [20].

To describe effects independent from individual probe dimensions, dimensionless variables were used. The tip-to-substrate distance (d) is normalized with respect to the electrode radius resulting in the normalized tip-to-substrate distance (L).

$$L = \frac{d}{a} \tag{27}$$

The normalized feedback current (N_I) is the current measured in bulk phase (I_∞) normalized with the measured current during the experiment (I_M).

$$N_I = \frac{I_M}{I_\infty} \tag{28}$$

2.4 Measuring modes

2.4.1 Feedback mode

A classical measurement principle in SECM is the feedback mode [21]. It is used for imaging the topography and electrochemical activity of the substrate. The signal in feedback mode is a Faraday current at the UME. The magnitude of the current is diffusion controlled and depends on the tip-to-substrate distance or the topography of the substrate and on the kinetic reaction

constant. This reaction constant is, inter alia, determined by the behavior of the substrate as conductor or insulator [22]. An amperometric measurement during the approach of the probe towards the substrate is called probe approach curve (PAC). In Fig. 2.10 the measured current depending on the substrate's property as conductor and insulator as well as on the distance are shown. A feedback occurs at tip-to-substrate distance of less than four times the electrode radius. [6]

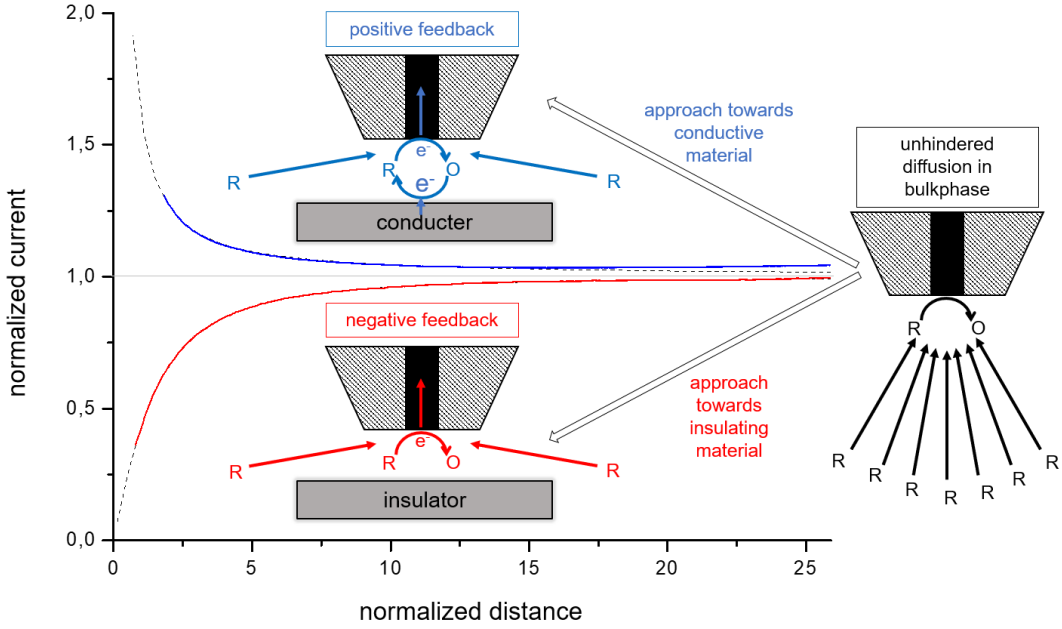

Figure 2.10: Schematic illustration of the feedback current by approaching different substrates. Adapted from [7].

In SECM imaging experiments using the feedback mode the tip-to-substrate distance is usually around one electrode radius. Approaching the probe towards an insulator (e.g. SiO_2, Polytetrafluoroethylene (PTFE)) results in a negative feedback. With smaller distance the insulating substrate blocks the mass transport of the mediator species towards the UME and lesser amount of mediator arrives at the UME. As consequence a decreased current, compared to the current in bulk solution, is measured. Approaching the probe towards a conductive substrate (e.g. Pt, Au) results in positive feedback in which the substrate electrode acts as bipolar electrode. The electrode gets polarized according to the Nernst equation by the local change in the concentration of mediator species induced by the electrochemical reaction at the UME [23]. The redox cycling of the mediator between probe and the conductive substrate results in an increased current compared to the current measured in bulk solution. Even though

blocking of the diffusion of the mediator towards the UME occurs in positive feedback the measured current is dramatically increased at tip-to-substrate distances smaller than two times the electrode radius. [6]

Mathematical expressions for the analytical treatment of PACs in both modes are described in literature [17,24,25]. The negative feedback strongly depends on the *RG* value of the probe. Lefrou et al. [25] reported a mathematical expression for the normalized measured current during a PAC under steady-state condition in negative feedback depending on *RG* and L.

$$N_I(L,RG) = \frac{\frac{2.08}{RG^{0.358}}\left(L-\frac{0.145}{RG}\right)+1.585}{\frac{2.08}{RG^{0.358}}(L+0.0023RG)+1.57+\frac{\ln(RG)}{L}+\frac{2}{\pi RG}ln\left(1+\frac{\pi RG}{2L}\right)} \quad (29)$$

The influence of the *RG* value on positive feedback is relatively weak and therefore an easier approximation published by Shao et al.[24] is commonly applied.

$$I(L) = B + \frac{C}{L} + De^{\frac{E}{L}} \quad (30)$$

In this equation A, B, C and D are parameters. Their values for different *RG* can be found in table 2.2. The use of the more complicated *RG* dependent approximation for positive feedback reported in [17] offers only significant advantages if the *RG* value of the UME is very small, exactly known and differs significantly from the values reported in table 2.2.

Table 2.2: In [24] reported parameter values for eq. 30.

RG	B	C	D	E
1.1	0.5882629	0.6007009	0.3872741	-0.869822
1.5	0.6368360	0.6677381	0.3581836	-1.496865
2.0	0.6686604	0.6973984	0.3218171	-1.744691
5.1	0.72035	0.75128	0.26651	-1.62091
10	0.7449932	0.7582943	0.2353042	-1.683087

The simultaneous dependence on both, conductivity and the tip-to-substrate distance makes data interpretation difficult. Imaging in feedback mode can be used to gain information about the morphology if the substrate is solely insulating or with a uniform reaction rate constant. To gain quantitative information about the activity of the substrate the morphology must be well known. One approach to overcome this problem is the exploitation of the negative feedback itself by exchanging the mediator solution. In one measurement the topographical information is recorded with an irreversible mediator and in a second measurement, with a reversible mediator, the electrochemical information. In literature several different approaches for

topographical and electrochemical imaging have been reported [26,27]. For example, the use of twin micro disk or micro ring disk configuration [28,29]. A specific combination of mediator systems is required to enable the measurement of the negative feedback at one electrode and at the other electrode the positive feedback. Another method is the hopping or standing probe approach [30]. Here, approach curves for each point of the final image are recorded which drastically increases the measurement time for the image. The so-called voltage switching mode is somehow a combination of both [31]. The hopping mode is used to approach the UME in negative feedback (for example O_2 reduction) and after the positioning the voltage is switched to a suitable potential to measure the current of a reversible mediator recording the activity. Schumann and coworkers developed a method to measured the tip-to-substrate distance by measuring the shear force between an oscillating UME and the substrate [32–34]. Alternating current techniques and the usage of fast scan cyclic voltammetry was applied to separate the topographical and electrochemical information [35–37]. The hyphenation of the SECM with other scanning probe techniques like AFM and scanning ion conductance microscopy [38] are promising.

2.4.2 Substrate generation/tip collection mode

The generation/collection mode includes a variety of experiments in which the signal mediating chemical species is generated in-situ at the substrate or the tip and respectively collected at the tip or the substrate [6]. This mode is typically used for the measurement of concentration profiles, chemical fluxes, kinetics or to modify surfaces [39–41]. The substrate generation/tip collection (SG/TC), illustrated in Fig. 2.11, is a subtype of the generation/collection mode. In the simplest form it is assumed that no side or consecutive reactions occur and that no feedback effects contribute to the detected signal. In the SG/TC mode an electroactive species is generated at the substrate and collected at the biased tip. If the size of the diffusion layer which arises from the substrate is much larger than the size of the tip, the SG/TC mode suffers from disadvantages like a transient signal and the lack of a steady state. Nevertheless, this mode is quite useful and extensively used.

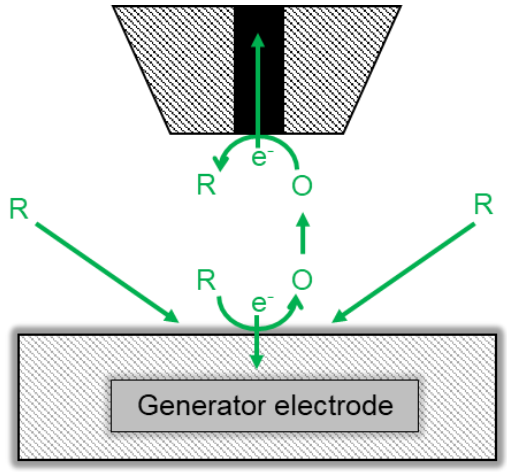

Figure 2.11: Schematic representation of the substrate generation/tip collection mode where reduced compound (R) present in the solution gets oxidized (O) and diffuses to the UME where it is collected. Adapted from [7].

2.5 Probe characterization

For an accurate evaluation of the collected data a detailed knowledge about dimensions and characteristics of the probe is mandatory. To characterize the shape, size and the quality of the probes including its sealing or fouling during fabrication and operation, different microscopic techniques and electrochemical methods are used [42]. Microscopic characterization with optical or scanning electron microscopy (SEM) delivers information about the insulation, the shape and the dimensions of the UME. Electrochemical methods provide additional information about the behavior in electrochemical experiments. Cyclic voltammetry provides information about the active electrode area. The radius can be calculated with eq. 31.

$$a = \frac{I_\infty}{4ncFD} \tag{31}$$

A deviation of the recording from theory indicates possible defects in the insulation (microfractures, cracks etc.) or fouling of the electrode area. The *RG* value is estimated by mathematical fitting of PACs in the negative feedback. Here, the approach speed of the probe is set at a value that allows steady-state condition during the movement of the probe. For fitting eq. 29 is used [43].

References

[1] A.J. Bard, L.R. Faulkner, Electrochemical Methods: Fundamentals and applications, 2nd edition, John Wiley & Sons Inc., New York, 2001.
[2] J. Wang, Analytical Electrochemistry, 3rd edition, WILEY-VCH, 2006.

[3] Cynthia Zoski, Handbook of electrochemistry, Elsevier, 2006.
[4] G. Henze, Polarographie und Voltammetrie: Grundlagen analytischer Praxis, Springer, Heidelberg, 2001.
[5] R.G. Compton, C.E. Banks, Understanding voltammetry, 2nd edition, Imperial College Press, London, 2011.
[6] A.J. Bard, M.V. Mirkin, Scanning electrochemical microscopy, 2nd edition, CRC Press, Boca Raton, 2012.
[7] C. Iffelsberger, T.J. Raith, P.J.H. Hanekamp, P. Vatsyayan, F.-M. Matysik, Trends in der elektrochemischen Rastermikroskopie, Chrom+food FORUM. 4 (2017) 20–22.
[8] A.J. Bard, G. Inzelt, F. Scholz, Electrochemical dictonary, Springer, Berlin Heidelberg, (2008).
[9] S. Bergner, Untersuchungen von Zellmonoschichten mittels Elektrochemischer Rastermikorskopie, University of Regensburg, 2013.
[10] S. Bergner, J. Wegener, F.-M. Matysik, Monitoring passive transport of redox mediators across a confluent cell monolayer with single-cell resolution by means of scanning electrochemical microscopy, Anal. Methods 4 (2012) 623–629.
[11] S. Bergner, J. Wegener, F.-M. Matysik, Simultaneous imaging and chemical attack of a single living cell within a confluent cell monolayer by means of scanning electrochemical microscopy, Anal. Chem. 83 (2011) 169–174.
[12] S. Bergner, P. Palatzky, J. Wegener, F.-M. Matysik, High-resolution imaging of nanostructured Si/SiO_2 substrates and cell monolayers using scanning electrochemical microscopy, Electroanalysis 23 (2011) 196–200.
[13] P. Vatsyayan, C. Iffelsberger, C.C. Mayorga, F.-M. Matysik, Imaging of localized enzymatic peroxidise activity over individual unbiased gold nanowires by scanning electrochemical microscopy, Anal. Methods 8 (2016) 6847–6855.
[14] C. Lee, C.J. Miller, A.J. Bard, Scanning electrochemical microscopy: Preparateion of submicrometer electrodes, Anal. Chem. 63 (1991) 78–83.
[15] J. Galceran, J. Cecília, E. Companys, J. Salvador, J. Puy, Analytical expressions for feedback currents at the scanning electrochemical microscope, J. Phys. Chem. B 104 (2000) 7993–8000.
[16] C.G. Zoski, M.V. Mirkin, Steady-state limiting currents at finite conical microelectrodes, Anal. Chem. 74 (2002) 1986–1992.
[17] C. Lefrou, A unified new analytical approximation for positive feedback currents with a microdisk SECM tip, J. Electroanal. Chem. 592 (2006) 103–112.
[18] S. Daniele, I. Ciani, D. Battistel, Effect of the insulating shield thickness on the steady-state diffusion-limiting current of sphere cap microelectrodes, Anal. Chem. 80 (2008) 253–259.
[19] C. Lefrou, R. Cornut, Analytical expressions for quantitative scanning electrochemical microscopy (SECM), Chemphyschem. 11 (2010) 547–556.
[20] J.L. Amphlett, G. Denuault, Scanning electrochemical microscopy (SECM): An investigation of the effects of tip geometry on amperometric tip response, J. Phys. Chem. B 102 (1998) 9946–9951.
[21] J. Kwak, A.J. Bard, Scanning electrochemical microscopy. Theory of the feedback mode, Anal. Chem. 61 (1989) 1221–1227.
[22] A.L. Whitworth, D. Mandler, P.R. Unwin, Theory of scanning electrochemical microscopy (SECM) as a probe of surface conductivity, Phys. Chem. Chem. Phys. 7 (2005) 356–365.
[23] A.I. Oleinick, D. Battistel, S. Daniele, I. Svir, C. Amatore, Simple and clear evidence for

positive feedback limitation by bipolar conductors, Anal. Chem 83 (2011) 4887–4893.
[24] Y. Shao, M.V. Mirkin, Probing ion transfer at the liquid/liquid interface by scanning electrochemical microscopy (SECM), J. Phys. Chem. B 102 (1998) 9915–9921.
[25] R. Cornut, C. Lefrou, A unified new analytical approximation for negative feedback currents with a microdisk SECM tip, J. Electroanal. Chem. 608 (2007) 59–66.
[26] M.A. O'Connell, A.J. Wain, Combined electrochemical-topographical imaging: A critical review, Anal. Methods 7 (2015) 6983–6999.
[27] S. Bergner, P. Vatsyayan, F.-M. Matysik, Recent advances in high resolution scanning electrochemical microscopy of living cells-a review, Anal. Chim. Acta 775 (2013) 1–13.
[28] M. Nebel, S. Neugebauer, K. Eckhard, W. Schuhmann, Ring-disk microelectrodes for simultaneous constant-distance and constant-current mode scanning electrochemical microscopy, Electrochem. Commun. 27 (2013) 160–163.
[29] T. Yasukawa, T. Kaya, T. Matsue, Dual imaging of topography and photosynthetic activity of a single protoplast by scanning electrochemical microscopy, Anal. Chem. 71 (1999) 4637–4641.
[30] O. Images, C. Using, H. Yamada, T. Matsue, Topographic, electrochemical, and optical images captured using standing approach mode scanning electrochemical / optical microscopy, Langmuir (2006) 10299–10306.
[31] Y. Takahashi, A.I. Shevchuk, P. Novak, B. Babakinejad, J. Macpherson, P.R. Unwin, H. Shiku, J. Gorelik, D. Klenerman, Y.E. Korchev, T. Matsue, Topographical and electrochemical nanoscale imaging of living cells using voltage-switching mode scanning electrochemical microscopy, Proc. Natl. Acad. Sci. 109 (2012) 11540–11545.
[32] M. Ludwig, C. Kranz, W. Schuhmann, H.E. Gaub, Topography feedback mechanism for the scanning electrochemical microscope based on hydrodynamic forces between tip and sample, Rev. Sci. Instrum. 66 (1995) 2857–2860.
[33] E.M. Hussien, W. Schuhmann, A. Schulte, Shearforce-based constant-distance scanning electrochemical microscopy as fabrication tool for needle-type carbon-fiber nanoelectrodes, Anal. Chem. 82 (2010) 5900–5905.
[34] H. Yamada, H. Fukumoto, T. Yokoyama, T. Koike, Immobilized diaphorase surfaces observed by scanning electrochemical microscope with shear force based tip - substrate positioning, Anal. Chem. 77 (2005) 1785–1790.
[35] F.D. Munteanu, M. Mosbach, A. Schulte, W. Schuhmann, L. Gorton, Fast-scan cyclic voltammetry and scanning electrochemical microscopy studies of the pH-dependent dissolution of 2-electron mediators immobilized on zirconium phosphate containing carbon pastes, Electroanalysis 14 (2002) 1479–1487.
[36] K. Eckhard, W. Schuhmann, Alternating current techniques in scanning electrochemical microscopy (AC-SECM), Analyst 133 (2008) 1486–1497.
[37] K. Eckhard, T. Erichsen, M. Stratmann, W. Schuhmann, Frequency-dependent alternating-current scanning electrochemical microscopy (4D AC-SECM) for local visualisation of corrosion sites, Chem. - A Eur. J. 14 (2008) 3968–3976.
[38] C.-C. Chen, Y. Zhou, L.A. Baker, Scanning ion conductance microscopy, Annu. Rev. Anal. Chem. 5 (2012) 207–228.
[39] J.V. Macpherson, P.R. Unwin, Determination of the diffusion coefficient of hydrogen in aqueous solution using single and double potential step chronoamperometry at a disk ultramicroelectrode, Anal. Chem. 69 (1997) 2063–2069.
[40] N. Baltes, L. Thouin, C. Amatore, J. Heinze, Imaging concentration profiles of redox-active species with nanometric amperometric probes: Effect of natural convection on transport at microdisk electrodes, Angew. Chem. Int. Ed. 43 (2004) 1431–1435.

[41] E.M. Oliveira, S. Beyer, J. Heinze, SECM characterization of immobilised enzymes by self-assembled monolayers on titanium dioxide surfaces, Bioelectrochemistry 71 (2007) 186–191.
[42] C.G. Zoski, Ultramicroelectrodes: Design, fabrication, and characterization, Electroanalysis 14 (2002) 1041–1051.
[43] R. Cornut, S. Poirier, J. Mauzeroll, Forced convection during feedback approach curve measurements in scanning electrochemical microscopy: Maximal displacement velocity with a microdisk, Anal. Chem. 84 (2012) 3531–3537.

3. Experimental

This section describes the chemicals, materials and instrumentation generally used to carry out research work outlined in this thesis. However, there are specific chemicals, materials and instrumentation which are only used in specific projects. They are described later in the corresponding section of the results and discussion chapter.

3.1 SECM Instrumentation

A commercial SECM system CHI 920c (CH Instruments, Austin, USA) was used (Fig. 3.1). It consisted of a bipotentiostat and a motor control unit that controls both the stepper motor and the piezo positioner. The electrochemical cell made of PTFE with an integrated Pt disk electrode (2 mm diameter) as substrate was bolted on a platform made of aluminum. The platform was held by three micrometer adjustment screws fixed on an object table of a transmitted-light microscope (magnification: x50, x100, x200, x500, x1000, Leica, Germany). The inverted optical microscope with the electrochemical cell and the stepper motors were placed within a faradaic cage on a damped workbench. The bipotentiostat, the motor control unit and the PC were placed on the side of the faradaic cage.

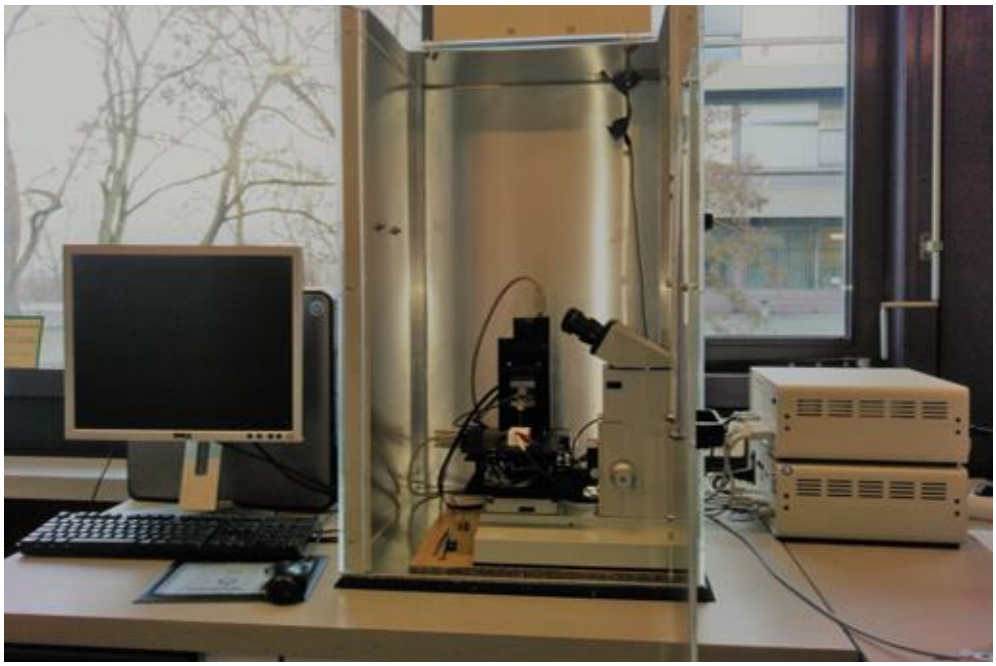

Figure 3.1: SECM placed in a faraday cage on a damped workbench with bipotentiostat, motor control unit and PC on its sides.

3.2 Ultramicroelectrode fabrication

3.2.1 Chemicals, materials & instrumentation

An aqueous solution containing 1.5 mM ferrocene methanol (FcMeOH, 99 %, ABCR, Karlsruhe, Germany) and KNO_3 (analytical grade, Merck KGaA, Darmstadt, Germany) as supporting electrolyte was used. All other chemicals were of analytical grade. All the solutions were prepared in ultrapure water with a resistivity higher than 18 MΩ cm (membraPure, Bodenheim, Germany).

For preparation of a stable mediator solution, the water was purged with N_2 for 15 min before dissolving FcMeOH and KNO_3 by sonication at 45 °C for 30 min. To prevent a dissolution of oxygen from air, the flask was tightly closed. After cooling and precipitation of residues over night the mediator solution was ready to use without further filtration.

For UME fabrication, Pt wires (12.5 µm and 25 µm diameter) and Wollaston-based Pt wires (600 nm Pt diameter) were obtained from Goodfellow (Cambridge, UK). Soda lime glass capillaries (type I860, inner diameter (ID): 1.1 mm; outer diameter (OD): 1.8 mm) were obtained from Technische Glaswerke Ilmenau (Ilmenau, Germany). The heating-coil was made from Kanthal wire (21 Ω m^{-1}, length 20 cm, 0.4 mm diameter, coiled in 10 loops with 6-7 mm loop diameter). As dual current (DC) power supply the PPS-11360 (180 W, Voltcraft) was used. For polishing, alumina (30, 10, 3, 0.3 µm, 3M, St. Paul, USA) and diamond lapping films (0.3, 0.1 µm, Precision surface international, Houston, USA) were used.

The electrochemical characterization of UMEs was performed in a two-electrode setup using the SECM. A Pt-wire with a diameter of 1 mm was used as a quasi-reference and counter electrode. Prior to experiments the Pt substrate electrode was polished with 0.3 µm alumina suspension on a polishing cloth (TexMed, Buehler, Lake Bluff, USA). Microscopic images were taken with wide stand microscope (magnification: x100, PEAK) and a smartphone camera and the digital microscope VHX-1000D (magnification: x500, x1000, Keyence, Osaka, Japan). For leveling of the substrate prior to the experiments a bullseye level (Model 1034, 14 mm diameter, sensitivity: 5', Glas- und Meßtechnik GmbH, Wächtersbach, Germany) was used.

3.2.2 Fabrication of Pt ultramicroelectrodes

UMEs with diameters > 10 µm were fabricated following the procedure described by Lee et al. [1]. Briefly, the Pt microwire was soldered to a copper wire and inserted into a pulled soda lime glass capillary and insulated by melting the glass with a microtorch or heating coil. The

exposure of the Pt disk electrode and the shaping of the surrounding glass-sealing was done by polishing with alumina (30, 10, 3, 0.3 µm) and diamond lapping films of decreasing grain sizes. All polishing steps were carried out manually. The tip of the UME was then heated using a lighter flame to retrieve the glass and to define the RG of the tip. A final fine polishing step was done with diamond lapping films of 0.1 µm grain size. Following this procedure, probes with an electrode diameter equal to the wire diameter and an RG ≈ 2-8 were routinely fabricated within one hour [2].

UMEs based on electrochemically etched 25 µm diameter Pt wires for sub-µm probes were fabricated in a similar way following the procedure described by Bergner et al. [3]. For the electrochemical etching, the Pt wire, already soldered on a copper wire, was inserted into a pulled soda-lime glass capillary unit it protrudes outside of the tapered capillary tip. The tip of the protrude Pt wire was carefully immersed in a solution of $CaCl_2$ (60 % v/v), H_2O (36 % v/v) and concentrated HCl (4 % v/v). The Pt tip was than etched in a two-electrode setup using differential pulse amperometry with potential pulses of ± 2 V (vs a Pt pseudo-reference electrode) at a frequency of 50 Hz. The etched Pt wire was inspected under a light microscope (100-fold magnification). The application of lower negative potential (-1 V) led to a milder etching with a brighter and smoother Pt surface. The etched Pt tip was then retracted into the capillary, sealed and polished as described above. Sub-µm UMEs of varying diameter with RG > 10 were fabricated following this procedure.

To simplify the fabrication and to decrease the RG of these sub-µm Pt UMEs, an alternative method for the glass-sealing of the electrochemically etched Pt tips was developed. After etching the Pt wire as described above, the Pt tip was inserted into a soda lime glass capillary. The middle part of the glass capillary was narrowed by careful capillary pulling. The Pt wire was inserted until around 2 cm of the Pt wire were inside the narrowed capillary part. As illustrated in Fig. 3.2A, the end of the glass capillary without Pt/Cu wire was then fixed (f) perpendicular through a heating coil. The heating coil (b) was made of Kanthal wire twisted and coiled in 4-5 loops with a loop diameter of 6-7 mm. In order to achieve a uniform heating, the coil was inserted in a borosilicate glass tube (c) (length ≈ 3 cm, ID: 7 mm, OD: 10 mm). The etched tip of the Pt wire was placed short above (< 5 mm) the top end of the heating coil. It was very important to strictly avoid any contact between the heating coil and the glass capillary. After the correct positioning, the soda lime glass was melted by heating the coil fast with DC power supply (~5-6 A) until the capillary fell into a funnel. The funnel made of glass

(B) was used to carefully catch the electrode and prevent a contact between the fragile tip and the wall of the tube. The pull of the melted glass during the plunge formed a thin glass sheath, which surrounded and sealed the Pt microwire and the etched tip. The exposure of the Pt was done by focused ion beam (FIB) milling with argon ions. Figure 3.2B shows a schematic drawing of the fabrication process.

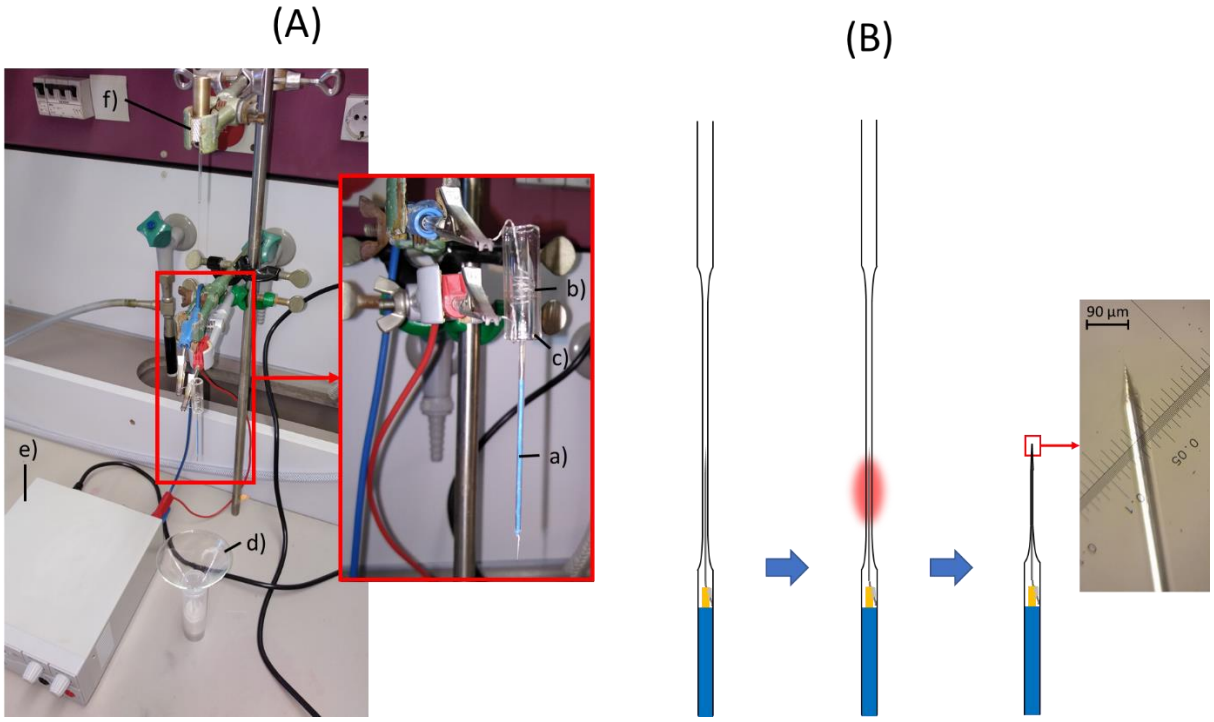

Figure 3.2: Setup (A) and schematic drawing (B) of the gravity enhanced fabrication method for high-resolution SECM probes. A) Photo of the workplace with the glass capillary (a), heating coil (b), borosilicate glass tubing (c), glass funnel (d), DC power supply (e) and the fixation of the capillary (f).

3.2.3 Fabrication of Wollaston-based Pt ultramicroelectrodes

This section is adapted from the work of Vatsyayan et al. [4], published by The Royal Society of Chemistry. The Wollaston-based Pt disk UMEs (radii 500 nm and 300 nm) were fabricated by the procedure described by Bond et al. [5] with partial modification. Briefly, the silver coated Pt wire was soldered to a copper lead. The wire was then inserted into a glass capillary (1.1–1.2 mm diameter) in such a way that the Wollaston wire protruded outside the capillary. The silver coating was then dissolved in concentrated nitric acid by dipping the tip of the wire in a drop of nitric acid with the help of a micromanipulator for ~30 min. The exposed Pt wire was then washed thoroughly in acetone and water to remove any debris on the wire. The wire was

then retrieved inside the glass capillary and dried at 100 °C for 1 h to remove moisture. The Pt wire was then sealed inside the glass capillary (through the joint from where it was exposed from the silver coating) following the procedure described by Bergner et al. [6]. A Kanthal wire was heated by a DC power supply (~10 V) for 5-10 s. The capillary containing the exposed Pt wire was placed inside the loop till the sealing was complete. The probe was then inspected under a light microscope (100-fold magnification) to ensure that the exposed Pt wire did not break inside the glass capillary during heating and cooling of glass around it. The disk-shaped Pt electrode was then exposed by polishing with alumina polishing foils of decreasing grain size (30, 10, 3, 0.3, 0.1 µm). Consecutively, a conically sharpened glass tip was prepared under microscope with 500 and 1000-fold magnification by manually polishing the glass-sealing from the sides with 0.3-0.1 µm alumina polishing foils. The diameter of the glass sheath produced in this way was typically about 10-20 µm.

3.2.4 Ultramicroelectrode characterization

SECM probes were characterized with the techniques described in section 2.5. Microscopic characterization was carried out using optical microscopy. For SECM probes with an electrode diameter > 10 µm the RG was determined using an optical microscope (100-fold magnification). For high resolution probes a higher magnification of 500 and 1000- fold was used. To evaluate the electrode diameter and the quality of the glass-sealing, CVs were recorded between -0.2 and 0.3 V with a scan rate of 50 mV s^{-1}. For the electrochemical RG determination PACs towards a polished Pt substrate for positive feedback and on insulators like glass or PTFE for negative feedback response were recorded with an approach speed of 0.5 µm s^{-1}. The evaluation was done by fitting and comparing theoretical expressions for negative [7] and positive [8] feedback current with experimental data. To check the performance of the fabricated probes interdigitated electrodes (Micrux Technologies, Oviedo, Spain) with 3 µm Pt strips separated by 2 µm distance (Type: IDA 4) or 10 µm Pt stripes with a separation of 10 µm (Type: IDA1) were used as standard substrates for imaging in feedback mode.

3.3 Substrate leveling and imaging

For SECM imaging a proper positioning of the substrate is prerequisite. The leveling of the substrate was done in two steps. First, a coarse leveling was done using a bullseye level. This bullseye level was placed on the side of or, if possible, inside the electrochemical cell. The

micrometer adjustment screws beneath the aluminum platform were used for leveling. For the fine adjustment of the remaining tilt, PACs were recorded at three edges of a virtual triangle around the area of interest. A 25 µm diameter probe and an increment distance of 2 µm and an increment time of 0.04 s was used for this PACs. The retrieval distance after the first approach was ≈ 400 µm and was adjusted after each approach so that the starting height was equal for each PAC. For leveling with smaller probes, the values for increment distance and the retrieval distance were adjusted depending on the size of the probe. The area covered by the virtual triangle was at least 1 mm^2. A satisfactory leveling was achieved within a tilt of less or equal to one probe radius per mm^2 substrate area. In cases where the tilt remained bigger the adjustment screws were used for fine adjustment and the tilt was determined again. This procedure was repeated until the desired leveling was achieved.

Imaging is a critical process in SECM studies and was always performed in constant height mode. The settings were adjusted for each project individually and are reported within the corresponding sections in the results and discussion chapter of this thesis.

References

[1] C. Lee, C.J. Miller, A.J. Bard, Scanning electrochemical microscopy: Prepareteion of submicrometer electrodes, Anal. Chem. 63 (1991) 78–83.

[2] C. Iffelsberger, P. Vatsyayan, F.-M. Matysik, Scanning electrochemical microscopy with forced convection introduced by high-precision stirring, Anal. Chem. 89 (2017) 1658–1664.

[3] S. Bergner, P. Palatzky, J. Wegener, F.-M. Matysik, High-resolution imaging of nanostructured Si/SiO_2 substrates and cell monolayers using scanning electrochemical microscopy, Electroanalysis 23 (2011) 196–200.

[4] P. Vatsyayan, C. Iffelsberger, C.C. Mayorga, F.-M. Matysik, Imaging of localized enzymatic peroxidise activity over individual unbiased gold nanowires by scanning electrochemical microscopy, Anal. Methods 8 (2016) 6847–6855.

[5] A.M. Bond, M. Fleischmann, J. Robinson, Electrochemistry in organic solvents without supporting electrolyte using platinum microelectrodes, J. Electroanal. Chem. 168 (1984) 299–312.

[6] S. Bergner, J. Wegener, F.-M. Matysik, Simultaneous imaging and chemical attack of a single living cell within a confluent cell monolayer by means of scanning electrochemical microscopy, Anal. Chem. 83 (2011) 169–174.

[7] R. Cornut, C. Lefrou, A unified new analytical approximation for negative feedback currents with a microdisk SECM tip, J. Electroanal. Chem. 608 (2007) 59–66.

[8] Y. Shao, M.V. Mirkin, Probing ion transfer at the liquid/liquid interface by scanning electrochemical microscopy (SECM), J. Phys. Chem. B 102 (1998) 9915–9921.

4. Results and discussion

4.1 Ultramicroelectrode characterization

4.1.1 Pt ultramicroelectrodes

UMEs made from unetched Pt wires (12.5 and 25 µm diameters), were used routinely for the experimental work. Such UMEs were comparably easy to fabricate and handle. The relatively thick tip was robust and easy to clean. Once the electrode surface was fouled or the sealing is damaged from crashing the probe into the substrate, it was possible to regenerate the tip either by polishing or by a repeated careful melting of the glass followed by polishing as described in section 3.2.2. Figure 4.1.1 exemplary shows the optical and electrochemical characterization of these Pt disk UMEs. The presented CVs show a steady-state current for the oxidation of FcMeOH. The PACs shown in Fig. 4.1.1C were in good agreement with the theoretical approach curves for both negative and positive feedback. The RG values of 2.4 for the 25 µm diameter UME and 2.3 for the 12.5 µm diameter UME are estimated from negative feedback curve and were in agreement with the optical images of the tips.

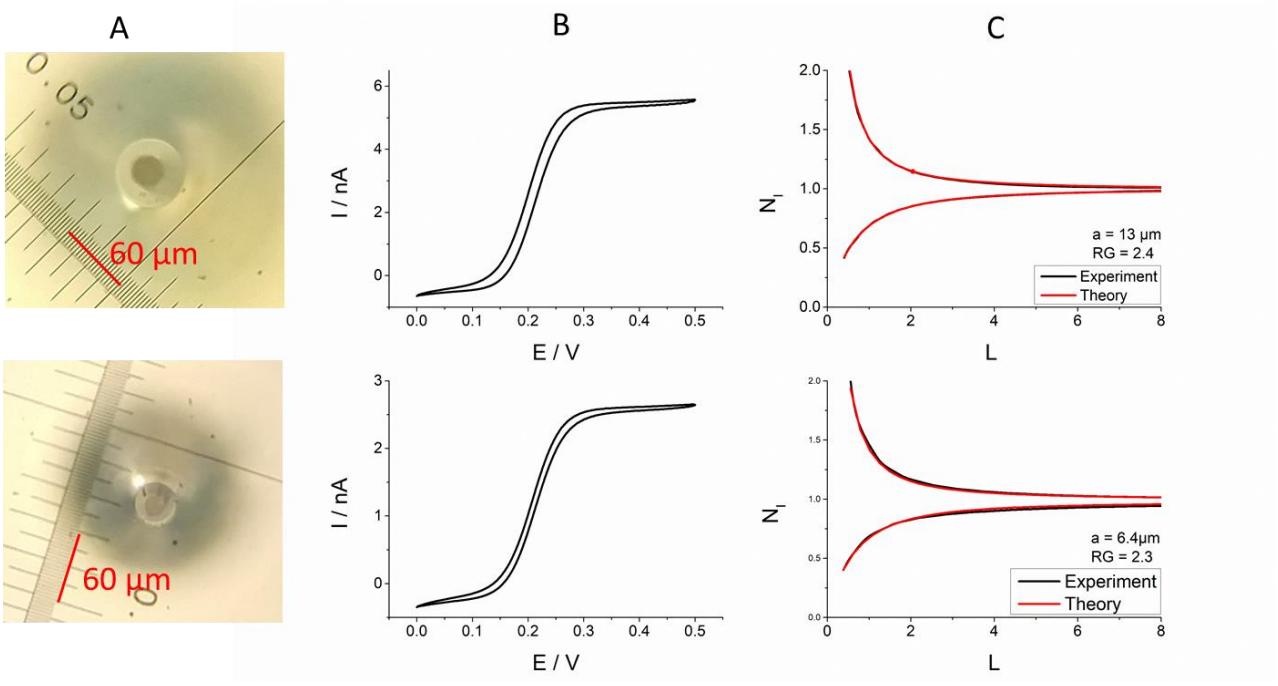

Figure 4.1.1: Characterization of UMEs. (A) Optical microscopic images of a 25 µm (above) and a 12.5 µm (below) diameter Pt disk UME tip (100-fold magnification). (B) Corresponding CVs of the UMEs at a scan rate of 50 mV s^{-1}. (C) Experimental and theoretical PACs of the

UMEs approaching a glass and a Pt substrate (approach speed: 0.5 µm s^{-1}). For electrochemical experiments 1.5 mM FcMeOH in 0.2 M KNO_3 was used as mediator and E_{UME} = 0.5 V.

4.1.2 Weight-force sealed etched Pt ultramicroelectrodes

Compared to the other fabrication methods described previously in this work, the probe fabrication with the weight force-sealing and FIB milling pronounced technical aspects instead of the experimenter's skill in manual polishing. The overall shape of the probe was equal compared to the probes fabricated by the other methods. However, the use of FIB milling limited the length of the probe to a maximum of 6 cm. The probes sealed by this method had a thin sheath of glass insulation around the electrode, though sealing the Pt microwire completely (Fig. 4.1.2A) forming a long and thin electrode ideal for hydrodynamic SECM experiments. For optical characterization and the determination of the electrode and tip diameter SEM imaging was used (Fig. 4.1.2B). Electrode diameters between 0.2 – 3 µm with RG values of ≤ 10 were achieved with this glass-sealing method.

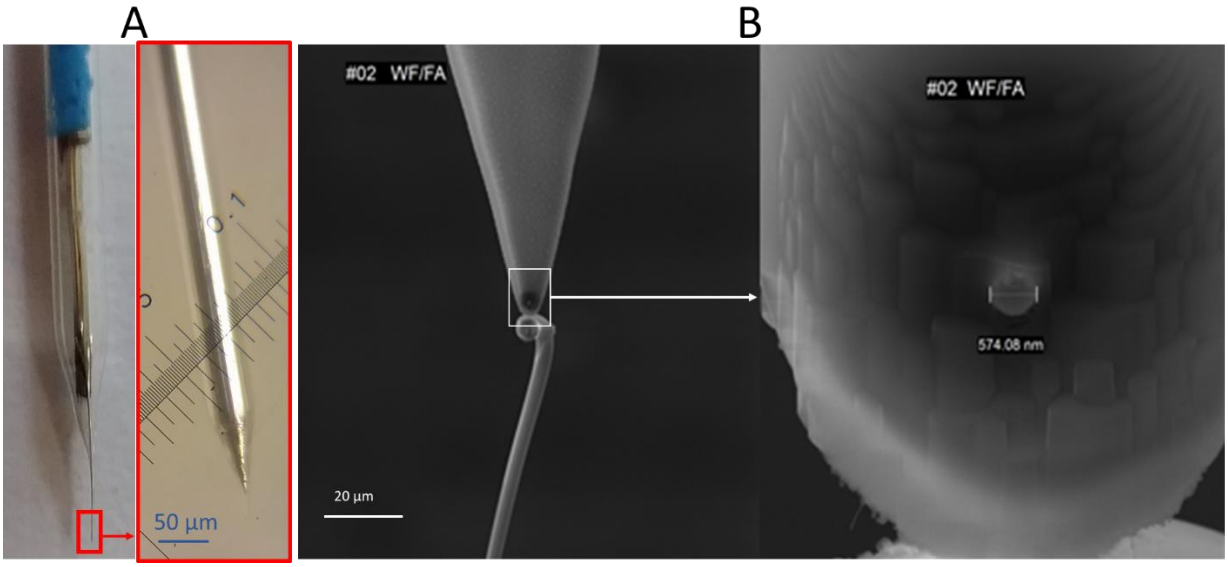

Figure 4.1.2: Images of an etched Pt UME produced with weight force-sealing. (A) Photograph and optical microscopic image of the electrode. (B) SEM images of UME after FIB exposure (a ≈ 300 nm, RG ≈ 8).

The electrochemical characterization of the probes was carried out to ascertain the quality of the probe and its sealing (Fig. 4.1.3). CV measurements showed small charging currents and hysteresis proving an intact glass-sealing of the Pt (Fig. 4.1.3A). Probe approach curves with

positive feedback on Pt and negative feedback on glass substrate followed theory closely (Fig. 4.1.3B). A high quality SECM image of an IDA1 interdigitated electrode (10 µm Pt strips with 10 µm gap) was obtained using these probes (Fig. 4.1.3C). These results established that the UMEs fabricated by weight-force sealing and subsequently FIB milling, were of high quality and superior in terms of RG compared to probes fabricated according other herein reported methods where the probes were manually polished.

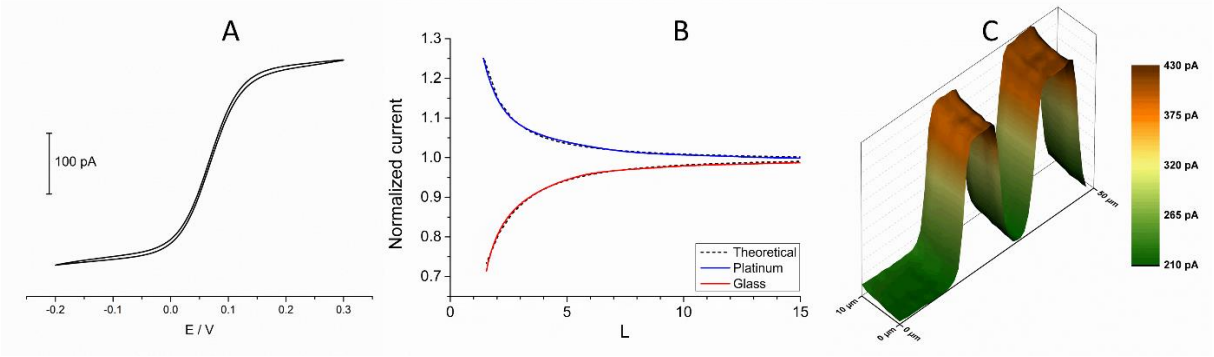

Figure 4.1.3: (A) CV of a weight force sealed UME (radius: 0.8 µm) at a scan rate of 100 mV s^{-1}. (B) Experimental and theoretical PACs of the UME (RG = 3 ± 1) approaching a glass and a Pt substrate (approach speed: 0.5 µm s^{-1}). (C) SECM image of an interdigitated Micrux electrode (IDA1, scan speed: 25 µm s^{-1}). All experiments were carried out in 1.5 mM ferrocene methanol with E_{UME} = 0.3 V vs Pt.

A limitation of this UME preparation method is the major technical effort necessary to expose the Pt disk electrode by FIB milling. Roughly, one quarter of the FIB prepared probes were usable. Further technical improvements of the glass-sealing are necessary to ensure the complete insulation of the Pt tip inside the capillary and to gain an improved yield.

4.1.3 Wollaston-based Pt ultramicroelectrodes

This section is adapted from the work of Vatsyayan et al. [1], published by The Royal Society of Chemistry. The Wollaston-based Pt UMEs are used since long for electrochemical studies [2] and SECM imaging [3]. However, fabrication of sub-micrometer UME probes was always a challenge because of the fragility of the exposed Pt nanowires and difficulty in their sealing inside the glass capillaries which required a lot of practice and patience. Despite of these limitations, the robustness of Wollaston-based Pt UMEs makes them an interesting target for exploitation in SECM imaging studies. With some minor modifications (as discussed in section 3.2.3) in the already established fabrication protocol of Wollaston-based Pt UMEs, the

fabrication of probes down to radii of 300 nm on a regular basis was possible. The probes once sealed and polished were robust enough to be used for multiple scans over long periods of time with intermittent cleaning and polishing. Thus, Wollaston-based probes provided an advantage over other relatively fragile sub-micrometer Pt disk probes fabricated by alternative methods such as Pt wire etching or capillary pulling. Fig. 4.1.4A shows the cyclic voltammograms of the sub micrometer Wollaston-based Pt UMEs. Well-defined voltammograms with minor hysteresis and stable steady-state currents were obtained. With cone formation, a RG value of ~10 was achieved for 500 nm probe, whereas, the RG for 300 nm probe was more than 10 (Fig. 4.1.4B).

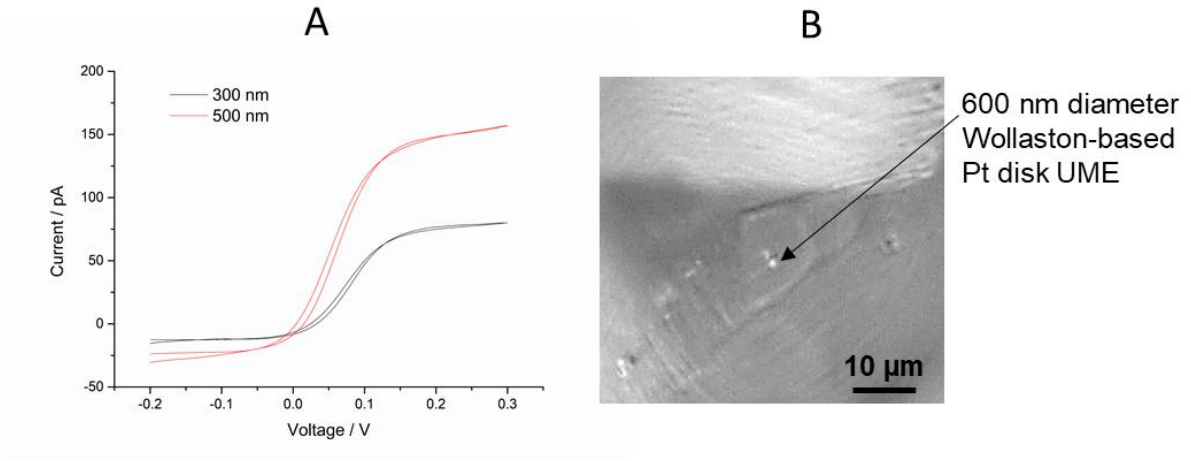

Figure 4.1.4: (A) Cyclic voltammograms of Wollaston-based Pt UMEs of different radii (500 nm and 300 nm) at a scan rate of 50 mV s^{-1}. (B) Optical microscopic image of a 300 nm radius Wollaston-based UME tip (1000-fold magnification). Adapted from [1]. Published by The Royal Society of Chemistry.

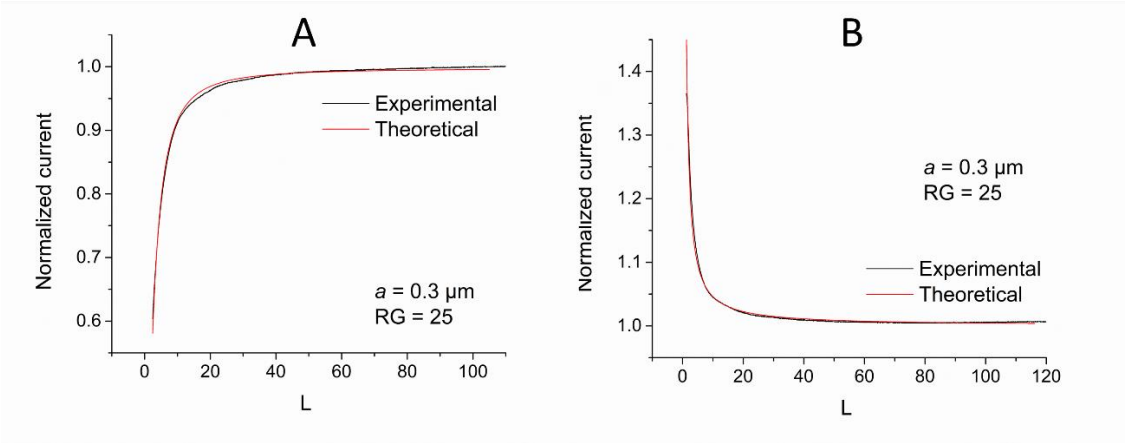

Figure 4.1.5: Experimental current–distance curves and corresponding theoretical curves obtained with a 300 nm Wollaston-based Pt UME by approaching an insulating glass substrate

(A) and a conducting gold-coated glass substrate (B). The probe potential was 0.3 V and the approach rate was 0.25 µm s^{-1}. The experiment was carried out in 1.5 mM ferrocene methanol solution (pH 5, adjusted with acetic acid). Adapted from [1]. Published by The Royal Society of Chemistry.

The probe approach curves over a flat glass substrate and a gold-coated glass substrate were recorded for calculation of RG of the fabricated 300 nm radius Wollaston-based Pt UME (Fig. 4.1.5). A high-resolution image of an interdigitated Micrux electrode with 3 µm Pt strips separated by 2 µm distance (nonconductive Pyrex material) was recorded with a 300 nm radius UME (Fig. 4.1.6A). A strong positive feedback current (~200 pA) because of recycling of ferrocene methanol at the Pt surface was recorded which was well resolved from the negative feedback current (~70 pA) from the Pyrex material in between the Pt strips. The I_∞ was ~100 pA. The SECM image of the interdigitated electrode structure correlated very well with its AFM image (Fig. 4.1.6B). The flat surfaces of Pt strips as recorded in AFM image were also visible in the corresponding SECM image. Figure 4.1.6C shows the representative areas imaged by SECM and AFM. The apparent width of the unbiased conductive Pt strip in the SECM image correlated closely with the actual width of the strip. Thus, the 300 nm radius probe was considered to be potentially suitable to image Gold nanowires later in section 4.5 which were 2-3 µm long and ~140 nm in diameter.

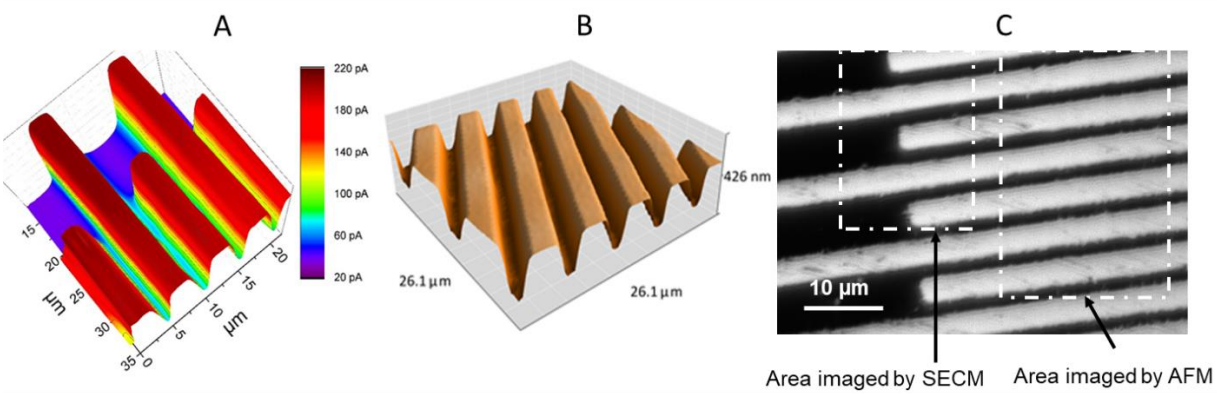

Figure 4.1.6: (A) High-resolution SECM image of an interdigitated Micrux electrode with 3 µm Pt strips separated by 2 µm distance (non-conductive Pyrex material). The image was recorded with a 300 nm radius Pt probe at a potential of 0.3 V and a scan rate of 12.5 µm s^{-1} in 1.5 mM ferrocene methanol solution. (B) Representative AFM image of the same substrate (C) Optical microscopic image of an interdigitated Micrux electrode with 3 µm Pt strips separated

by 2 µm distance (non-conductive glass material). Adapted from [1]. Published by The Royal Society of Chemistry.

4.1.4 Conclusion

Different alternative approaches were used to fabricate UMEs and supplement already existing fabrication methods to improve the overall efficiency of the fabrication procedure and to maintain a constant supply of high-quality probes for the variety of SECM experiments mentioned in this work. The described procedure for the fabrication of UMEs with diameters > 10 µm enabled the fabrication of well insulated electrodes with RG values between 2 and 10. The fabrication of high resolution probes (electrode radii of < 1 µm) remained difficult and time consuming. Nevertheless, the improved quality and the robustness of the probes compensate the drawbacks. The use of novel fabrication techniques like the focused ion beam enabled the fabrication of UMEs with sub-micrometer electrode diameters, insulated by a soda lime glass layer of few µm thickness. The characterization showed favorable characteristics of the UMEs and established their potential for high resolution SECM experiments in combination with forced convection.

References

[1] P. Vatsyayan, C. Iffelsberger, C.C. Mayorga, F.-M. Matysik, Imaging of localized enzymatic peroxidise activity over individual unbiased gold nanowires by scanning electrochemical microscopy, Anal. Methods 8 (2016) 6847–6855.

[2] A.M. Bond, M. Fleischmann, J. Robinson, Electrochemistry in organic solvents without supporting electrolyte using platinum microelectrodes, J. Electroanal. Chem. 168 (1984) 299–312.

[3] A.J. Bard, Electronanalytical chemistry, Marcel Dekker, New York, 18 (1994).

4.2 Scanning electrochemical microscopy with forced convection introduced by high-precision stirring

Christian Iffelsberger, Preety Vatsyayan and Frank-Michael Matysik,

Analytical Chemistry 89 (2017) 1658–1664.

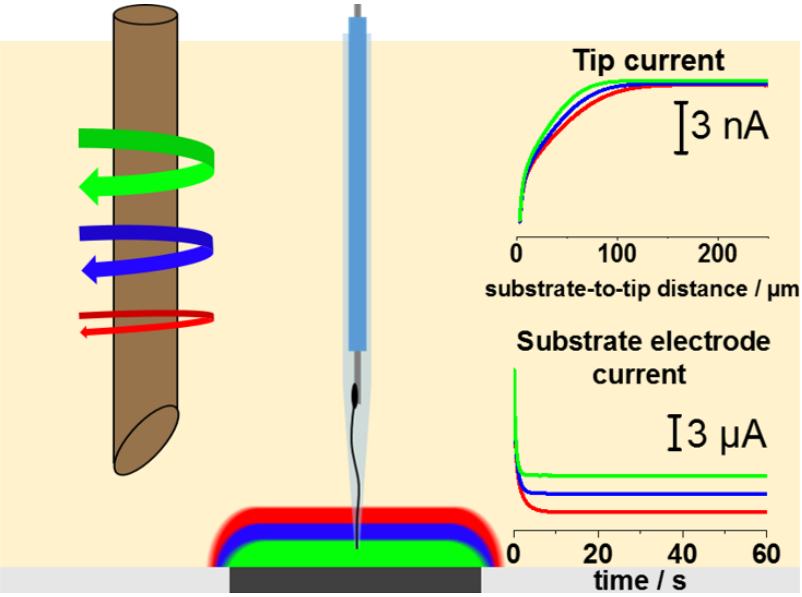

Abstract

In this section the well-known advantages of hydrodynamic mass transport in electrochemical systems are used in combination with scanning electrochemical microscopy (SECM). The hydrodynamic SECM system integrates a high-precision stirring device into the experimental setup. The well-defined stirring of the SECM electrolyte results in steady-state diffusion layer characteristics in the vicinity of large substrate electrodes operated in chronoamperometric measuring mode. For a range of rotation frequencies of a rotating cylinder the thickness and the stability of the diffusion layer was studied by hydrodynamic SECM in the substrate generation/tip collection (SG/TC) as well as in the competition mode using ferrocene methanol as redox mediator. Different UME probe dimensions ranging from Pt diameters of 20 µm down to 0.6 µm were used. The smallest probe with 0.6 µm electrode diameter was found most suitable for these studies due to the almost convection-independent amperometric response associated with sub-µm electrodes. Additionally, preliminary studies of hydrodynamic SECM imaging of a 2 mm Pt disk electrode surface in the SG/TC mode based on in-situ produced

hydrogen as mediator are presented. Comparative images measured in the conventional positive feedback mode in quiescent solution show that hydrodynamic SECM offers attractive complementary information.

4.2.1 Introduction

The technique of scanning electrochemical microscopy (SECM), after its introduction by Bard and co-workers in 1989 [1], has evolved to a powerful electrochemical tool for the high resolution imaging of topography and surface (re)activity as well as for the investigation and determination of important (electro)chemical parameters for mass transfer rates and reaction kinetics [2]. Besides the common feedback mode [3], the generation/collection mode [4] is an alternative approach for SECM experiments with two variants, the tip generation/substrate collection (TG/SC) and the substrate generation/tip collection (SG/TC) modes. In the SG/TC mode, a substrate-generated species is detected at the SECM probe at a diffusion-limited rate. This mode was used to monitor concentration profiles [5], localized enzyme activity [6] or to gain a deeper insight into the oxygen reduction reaction [7] which is important for battery and corrosion research, to name just a few examples. Also a large number of novel techniques like the hopping intermittent contact [8], surface interrogation [9] and redox competition mode [10] are based on the SG/TC mode. One limitation of the SG/TC mode is the time-dependent amperometric signal. In quiescent solution the substrate electrode current is transient due to the growth of the diffusion layer thickness with time. Consequently, the probe current at fixed tip-to-substrate distance changes also with time. To achieve a steady-state or at least a quasi steady-state mass transport, several methods were used. A quasi steady-state around the tip-substrate gap with a separation of a few micrometers was achieved after a macroscopic substrate was held at a fixed potential for a brief period of time [4,11,12], when the potential was swept slowly at 2 mV s^{-1} [13] or by cyclic sweeping of the substrate potential around E^0 for rapid electron transfer reactions [14]. Furthermore, potential pulses at the substrate electrode were used to limit the extension of the diffusion layer above the substrate [15–17]. A real steady-state mass transport was achieved by the use of micro or ultramicroelectrodes instead of macroscopic substrate electrodes [18,19]. A disadvantage of this approach was the restriction concerning the size of the substrate. This results in limitations concerning several practical applications where studies at surfaces of large substrates are of interest.

In electroanalytical chemistry with macroscopic electrodes, the introduction of forced convection into the electrochemical system is a well-established way for enhancing the analytical performance. Hydrodynamic voltammetry is associated with the advantage of considerably increased mass transport under steady-state conditions [20]. Various techniques of hydrodynamic voltammetry exploiting the increased mass transport are known. Typical examples are different kinds of rotating electrodes [21–23], a variety of flow systems like channels [24], wall- and micro-jets [25,26] or tubes as well as convective systems based on sonication [27], microwave radiation [28] and even magnetic fields [29,30] have been applied. The effect of natural convection on the signal at the UME was addressed in a study by Baltes et al. [18] in which they showed that natural convection has no effect on the amperometric signal and just a small effect on the diffusion layer of an UME with a radius of 40 µm at distances smaller than 16 µm. The influence of forced convection due to the moving UME on positive feedback approach curves was studied to provide an expression for the maximal approach velocity [31]. During the imaging process forced convection originating from the probe velocity can induce a perturbed current response [32], so the imaging with different probe velocities was used to distinguish between active and less active spots at substrates with a well-known surface morphology [33]. Based on this work, a method for high speed SECM imaging [34] was developed and used to study living cells [35]. Another approach to SECM experiments in a hydrodynamic environment was the use of capillary-based probes with integrated microwires. Palatzky et al. [36] used this special probe configuration for the characterization of the reproducibility and for the optimization of positioning of a fused silica capillary above a large substrate electrode for the concept of electrochemically assisted injection in capillary electrophoresis [37]. The opposite way, the integration of a nanoflow-system into a SECM probe, was reported by Momotenko et al. [38]. They developed a so-called microfluidic push-pull probe. In this flexible probe a working and a reference electrode as well as two micro-channels were integrated. One microchannel was used for the delivery (push) and the other one for the aspiration (pull) of mediator solution. With this probe they generated SECM images of a dry substrate by applying just a nanodroplet to the substrate. A different approach was reported by Kai et al. [39] using a nanoflow system for the continuous delivery of fresh mediator solution to increase the resolution of the SECM for the imaging of spots of active horseradish peroxidase enzyme.

In this section of work, a new approach to establish steady-state mass transport at macroscopic electrodes in combination with SECM experiments is described. Forced convection is introduced to the SECM measuring cell by high-precision stirring. It is showen that hydrodynamic SECM measurements in the SG/TC and competition modes can be used for detailed studies within the steady-state diffusion layer of a large substrate electrode. Preliminary results for the application of hydrodynamic SG/TC experiments based on hydrogen evolution at the substrate will be presented.

4.2.2 Experimental

Chemicals

An aqueous solution containing ferrocene methanol (FcMeOH, 99%, ABCR, Karlsruhe, Germany) as mediator and KNO_3 (analytical grade, Merck KGaA, Darmstadt, Germany) as supporting electrolyte was used. All other chemicals were of analytical reagent grade. The solutions were prepared in ultrapure water with a resistivity higher than 18 MΩ cm (membraPure, Bodenheim, Germany).

Instrumentation

For all experiments, a commercial SECM system CHI 920C (CH Instruments, Austin, USA) with the included electrochemical cell and a Pt disk electrode (2 mm diameter) as substrate electrode was used. Prior to all experiments the substrate electrode was polished with 0.3 µm alumina suspension on a polishing cloth (TexMed, Buehler, Lake Bluff, USA). An Ag/AgCl/sat. KCl electrode and a Pt-wire electrode were used as reference and counter electrodes, respectively. All the potentials mentioned in this work refer to the reference electrode specified above. To protect the electrochemical cell from any disturbances caused by electrical fields or vibrations, the electrochemical cell and the SECM positioning unit were placed in a homemade faradaic cage on a damped working bench. The stirring system consisted of an electrical motor (2250S012BX4 CSD 3830, BL- DC- Motor with integrated motion controller, Dr. Fritz Faulhaber GmbH & Co. KG, Schönaich, Germany) and a homemade rotating cylinder (polyether ether ketone (PEEK); length: 9.7 cm, diameter: 3 mm, beveled at the end (45°)). A stirrer guide made of a borosilicate glass tube (length: 2 cm, ID: 3 mm, OD: 6 mm) completed the stirring system. To control the electrical motor via PC an adapter board (BX4CxD RS/CAN) and the motion manager 5 software both provided by Dr. Fritz Faulhaber

GmbH & Co were used. To inhibit electrical disturbances the current circuit of the SECM and the stirrer were separated via an isolation transformer (230/230V ~50Hz, 550 VA, Voltcraft, Germany). A homemade 3D-printed sliding cap with several holes was used to cover the electrochemical cell and to ensure a precise (re-) positioning of the stirrer. UMEs with diameters of 10 and 20 µm were fabricated following the procedure described by Lee et al. [40]. The sub-micrometer Pt disk UME (600 nm diameter) was fabricated using Wollaston-based Pt (600 nm Pt diameter, Goodfellow, Cambridge, UK) wire by following the procedure described by Bond et al. [41] with a partial modification as described by Vatsyayan et al. [42]. The detailed descriptions for probe fabrication are covered in section 3.2.

Experimental setup

The setup for hydrodynamic SECM experiments is shown in Figure 4.2.1. To protect the electrochemical cell from vibrations caused by the electrical motor the holder was placed alongside the damper plate of the working bench so that there was, beside the electrolyte solution, no contact between the SECM and the stirrer system. To achieve a uniform and reproducible convection above the substrate electrode the precise positioning of both the electrochemical cell and the stirrer (1) was a prerequisite. The electrochemical cell was levelled within a range of 30 µm height difference per 1.5 cm distance between the measurement points using three micrometer adjustment screws. To fix the X, Y position of the rotating cylinder in the plane of the electrochemical cell, a 3D-printed sliding cap (3) with several holes for the stirrer (3.5 mm diameter) and the SECM probe (5) was used. This mask covered the cell tightly enough to keep the distance between center of the substrate electrode (4) and stirrer fixed at 0.8 cm so that for all experiments the same distance was used. To avoid any vibration due to contact of mask and rotating stirrer shaft, the alignment needed to be done carefully to prevent a contact between the stirrer and the slide cap during measurements. To predefine the penetration depth of the stirrer into the solution the distance between the bottom of the cell and the end of the stirrer (1 mm) was adjusted by matching a mark at the stirrer shaft with the top of the mask. To avoid oscillations of the stirrer shaft (length: 10 cm) at higher rotation speed, a borosilicate glass tube was used as a guide (2). In all experiments, the electrochemical cell was filled with 6 ml solution. In experiments with a moving probe, the electrical motor created interferences to the amperometric signal. To eliminate this interference the sampling time of the current measurement was synchronized with the rotation speed f_{rot} of the motor.

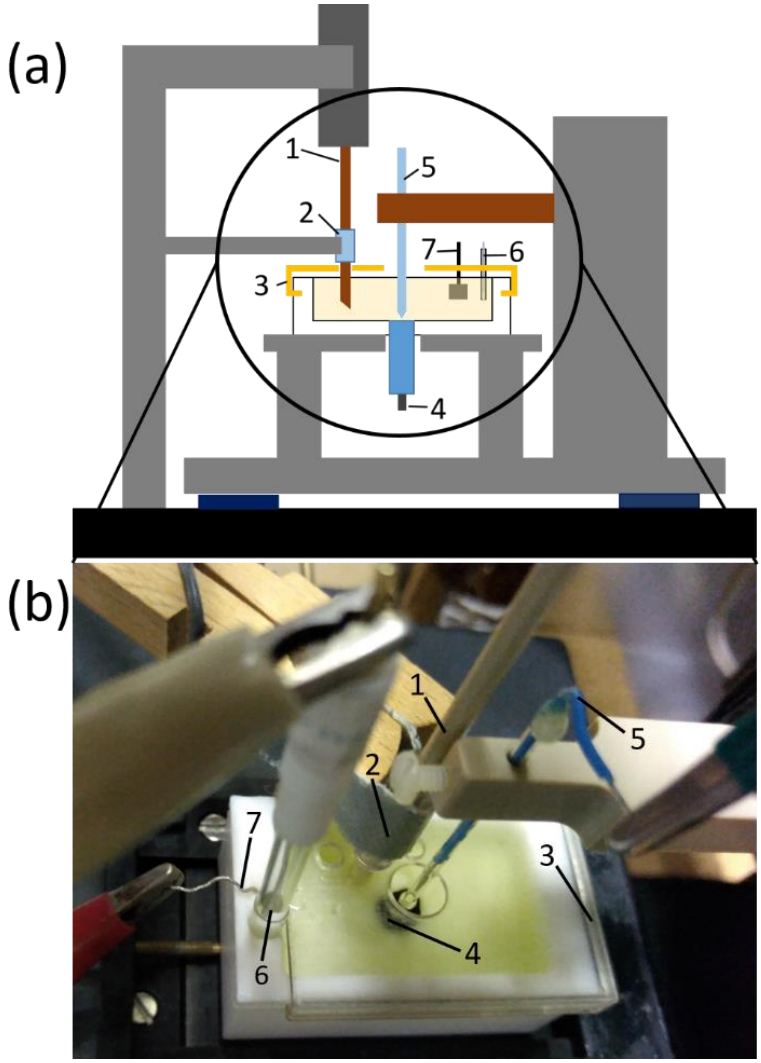

Figure 4.2.1: Schematic representation (a) and photograph (b) of the experimental setup for hydrodynamic SECM experiments. Components: High-precision electrical motor with stirrer (1), guide for the stirrer (2), mask for the positioning of the stirrer (3), substrate electrode (4), SECM probe (5), reference electrode (6), and auxiliary electrode (7). Copyright © 2017 American Chemical Society.

Hydrodynamic SECM experiments for the characterization of the diffusion layer for a large substrate electrode (2 mm diameter)

In all experiments FcMeOH was oxidized at the substrate electrode at a potential of $E_{substrate}$= 0.45 V. A solution of 1.5 mM FcMeOH with 0.2 M KNO_3 was used. To demonstrate the effect of forced convection on the mass transport and consequently on the thickness of the diffusion layer, chronoamperometric measurements at the substrate electrode were performed.

The rotation speed of the stirrer was varied from 8.3 to 33.3 s^{-1}. The solution was stirred for about 1 min prior to each measurement to achieve a uniform convection throughout the solution. The current was measured for 60 s with 0.1 s sampling time. Based on the steady-state limiting current, the thickness of the diffusion layer (δ) was calculated.

To study the influence of the probe size on the quality of recording diffusion layer profiles near the substrate electrode under hydrodynamic conditions, probes with different electrode diameters (0.6, ~10, ~20 µm) were used. The rotation speed of the rotating cylinder was varied ranging from 8.3 to 16.7 s^{-1}.

Prior to hydrodynamic SECM studies conventional probe approach measurements were made in quiescent solution. The probes were positioned at a tip-to-substrate distance corresponding to the normalized value I_M/I_∞ of 300 % for 20 µm and 10 µm probes and 125 % for the 0.6 µm probe. To determine the exact distance, the current ratio (I_M/I_∞) was compared to theoretical probe approach curves (PACs) calculated with the simplified equation reported by Shao et al. [43]. After the positioning of the probe near the substrate and prior to all hydrodynamic recordings the probe was retracted for 400 µm using the stepper motor. In all further experiments, the approach velocity was 20 µm s^{-1} and each approach was repeated at least two times (N = 2).

Hydrodynamic SECM imaging

To study the influence of forced convection on SECM imaging, two different experiments were performed. To investigate the stability of the diffusion layer repetitive images in the SG/TC mode were recorded with and without stirring. The potentials were $E_{substrate}$= 0.45 V and E_{UME} = 0 V. In order to position the probe at a suitable tip-to-substrate distance a PAC was recorded in quiescent solution as described earlier. Then the probe was retrieved to fix a tip-to-substrate distance of ~28 µm. To reduce the noise generated by the electrical motor an i/E conversion filter with 0.32 Hz was applied. The experiment was performed in 1.5 mM FcMeOH mediator solution at a probe velocity of 100 µm s^{-1} and a quiet time of 1 s. The rotation speed was set at f_{rot}= 16.7 s^{-1} and the solution was stirred until the convection was uniform (1 min).

In the second experiment, the SECM with forced convection was used for imaging and surface characterization of a Pt disk electrode in the SG/TC mode by using in situ generated hydrogen as mediator. For this experiment, the positioning of the stirrer was done as described before. However, the mask was removed before performing the experiment to enable access to the

solution. For the height positioning of the stirrer, the end of the PEEK cylinder was first placed in contact to the cell bottom and then lifted for 1 mm. The Pt disk electrode was first imaged with 1.5 mM FcMeOH as mediator in quiescent solution at an approach position corresponding to I_∞ = 135 %. Afterwards, the mediator solution was exchanged with 0.2 M KNO_3 solution. The rotating speed of the stirrer was set to 16.7 s^{-1}. For hydrogen generation at the substrate electrode, a potential of $E_{substrate}$ = -1.2 V was applied. To oxidize the hydrogen, the tip potential was set at E_{UME} = -0.1 V. In both images the probe velocity was 150 µm s^{-1}.

4.2.3 Results and discussion

Hydrodynamic SECM for diffusion layer studies using UME probes of different size

The application of well-defined convection in chronoamperometric experiments led to enhanced steady-state currents at large electrodes. Using a rotating cylinder as source of convection, the strength of convection is defined by the rotation speed of the stirrer. Without stirring, the diffusion layer above a large substrate electrode would grow infinitely into the solution. The chronoamperograms for the oxidation of FcMeOH at a 2 mm Pt disk substrate electrode in presence and absence of convection are shown in Figure 4.2.2. In quiescent solution (Figure 4.2.2a) the typical current decay according to the Cottrell equation is observed. In contrast, the application of convection induced by a rotating stirrer created a stable diffusion layer in the vicinity of the substrate electrode associated with an increased and constant current (Figure 4.2.2b-d). The steady sate currents were 3.322 ± 0.003 µA, 4.633 ± 0.002 µA, and 5.908 ± 0.007 µA for rotation speeds of 8.3 s^{-1}, 16.7 s^{-1}, and 25 s^{-1}, respectively. Simulations using COMSOL Multiphysics, presented in section 4.3, strengthen the suggestion of a laminar convective conditions near the substrate electrode. For rotation speeds higher than 25 s^{-1} there were only minor further mass transport enhancements and the precision of current recordings declined indicating turbulent convective conditions. In most of the following experiments, the rotation speed of the stirrer was set at 16.7 s^{-1} ensuring high stability of mass transport towards and from the substrate electrode.

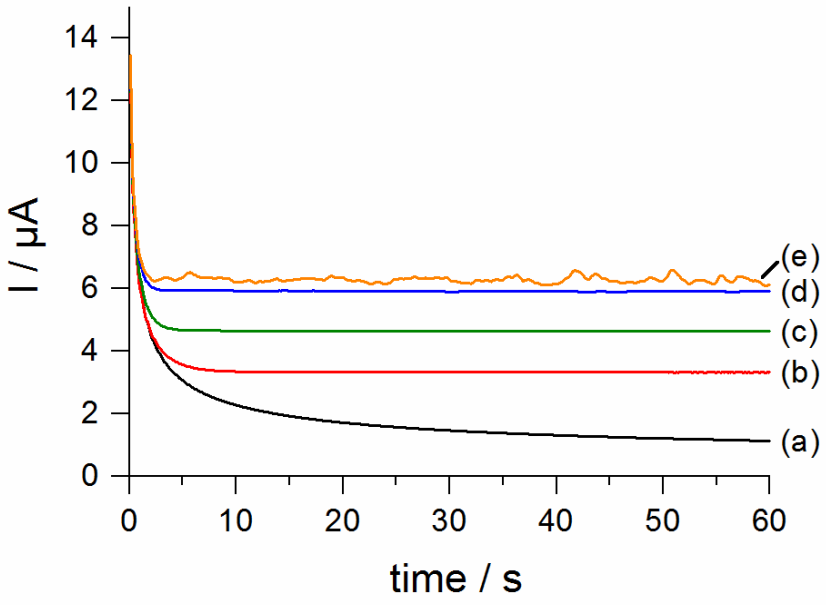

Figure 4.2.2: Chronoamperometric recordings for the oxidation of FcMeOH at a Pt disk electrode (2 mm diameter) at different rotation speeds of the stirrer. (a) without stirring, (b) 8.3 s^{-1}, (c) 16.7 s^{-1}, (d) 25 s^{-1}, (e) 33.3 s^{-1}. The measurements were carried out using a solution containing 1.5 mM FcMeOH and 0.2 M KNO_3. The electrode potential was set at 0.45 V. Copyright © 2017 American Chemical Society.

Figure 4.2.3 shows results of hydrodynamic SECM experiments for the characterization of the diffusion layer in the vicinity of a 2 mm Pt disk electrode. The measurements were done in the substrate generation/tip collection (SG/TC) as well as in the competition mode. In the former one the concentration profile of the oxidized species ($FcMeOH^+$) can be studied while the latter one reflects the concentration change of FcMeOH. Interestingly, for measurements in the competition mode for tip-to-substrate distances larger than the diffusion layer thickness there was still a slight current increase measured at the UME for increasing distances from the substrate electrode in the case of the rather large UME probes (20 µm and 9 µm diameter). The steady-state current of UMEs in this size region shows still some dependence on changing convective conditions. In contrast, an UME probe with sub-µm diameter exhibits a nearly convection-independent current response [44]. Consequently, the probe current in the competition mode measured with the 0.6 µm UME is nearly constant for tip-to-substrate distances larger than 100 µm and independent of the rotation speed of the stirrer. In addition, deviations from a linear concentration gradient of FcMeOH due to competition with the

substrate electrode are just seen at closer tip-to-substrate distances in the case of the 9 µm and 20 µm UME probes. Deviations from a linear concentration gradient in close vicinity to the substrate electrode surface can also be attributed to the physical presence of the probe tip influencing the diffusion field of the substrate electrode. This would explain why the 0.6 µm electrode shows also some deviation from a linear concentration gradient without being affected by competition effects.

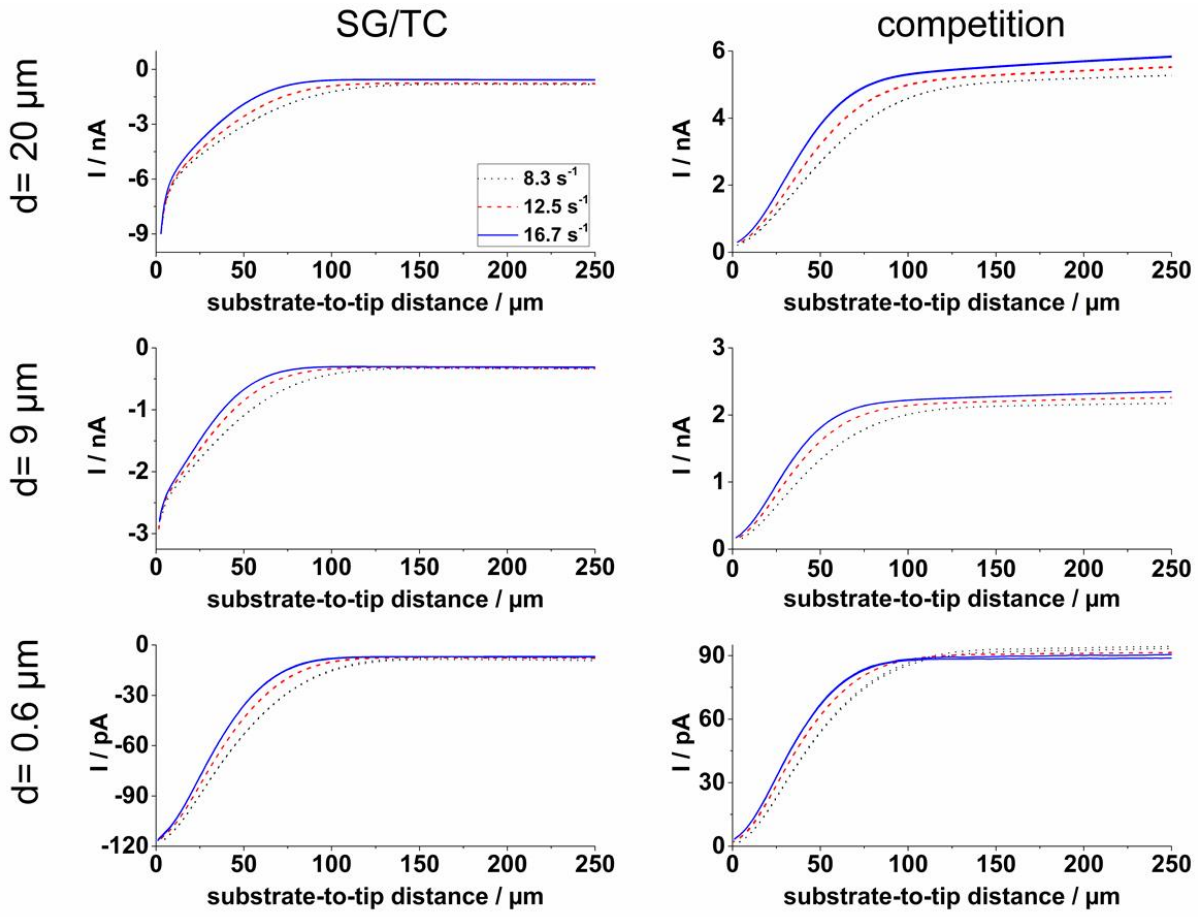

Figure 4.2.3: Study of the diffusion layer in the vicinity of a 2 mm Pt disk electrode by hydrodynamic SECM using UME probes with different diameters (20 µm, 9 µm and 0.6 µm) applying varying stirrer rotation speeds (dotted line, 8.3 s^{-1}; dashed line, 12.5 s^{-1}; solid line, 16.7 s^{-1}). The probe potentials in SG/TC mode and competition mode were 0 V and 0.45 V, respectively. The substrate electrode potential was set at 0.45 V. The measurements were carried out using a solution containing 1.5 mM FcMeOH and 0.2 M KNO_3. Copyright © 2017 American Chemical Society.

It has to be stated that repetitive measurements of the concentration profiles of the mediator and its oxidized form, in absence of convection, show a steady growth of the diffusion layer for increasing reaction times and rather poor reproducibility.

In the SG/TC mode (Figure 4.2.3 left) with all probes, a small cathodic offset was measured. Upon closer approach to the substrate electrode, the current increased with increasing concentration of $FcMeOH^+$ generated at the substrate electrode. In closer proximity to the substrate electrode (< 25 µm) deviations from the linear behavior of the measured probe signals and a strong dependence on the probe size was seen. For a 20 µm probe, a large increase in the UME current at a tip-to-substrate distance of ~ 25 µm was found. This is due to a redox cycling effect leading to an enhanced current. The same effect was measured in the case of the 9 µm probe at relatively closer distances of ~ 10 µm. For the sub-µm probe (0.6 µm diameter) the effect of a redox cycling was not observed as the shortest tip-to-substrate separation was just ~1 µm. The application of different rotation speeds in both modes illustrated the dependence of the thickness of the diffusion layer on the rotation speed. In agreement with the chronoamperometric recordings shown in Figure 4.2.2 an increase in rotation speed resulted in a reduced diffusion layer thickness. Based on the above results the 0.6 µm UME probe was better suited for an undistorted characterization of the diffusion layer in the vicinity of a 2 mm Pt disk electrode and was consequently used for a more detailed study.

Determination of the diffusion layer thickness

A detailed view of the diffusion layer is illustrated in Figure 4.2.4. To calculate the thickness of the diffusion layer the recordings of the concentration profiles in both, competition (corresponding to FcMeOH) and SG/TG (corresponding to $FcMeOH^+$) modes were used. The perpendiculars of the intersection points of the two tangents in the respective plots shown in Figure 4.2.4 were used for the determination of the diffusion layer thickness.

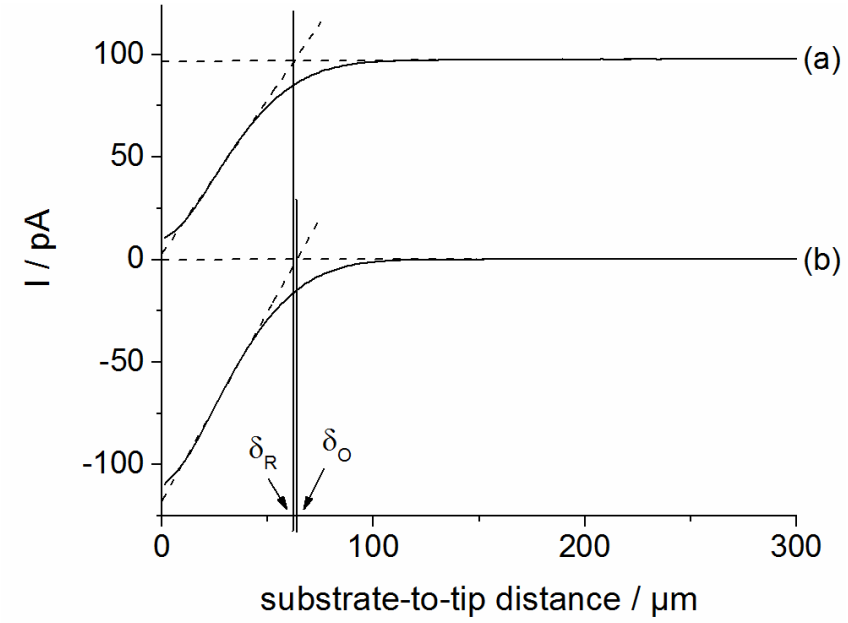

Figure 4.2.4: Detailed view of the diffusion layer characteristics for a 2 mm Pt disk substrate electrode recorded by hydrodynamic SECM using a 0.6 µm UME. The rotation speed of the stirrer was 16.7 s^{-1}. Measuring modes: (a) competition mode (E_{UME} = 0.45 V) and (b) SG/TC mode (E_{UME} = 0 V). The substrate electrode was set at a potential of 0.45 V, δ_R and δ_O represent the diffusion layer thicknesses derived from of the concentration profiles of the oxidized ($FcMeOH^+$, δ_O) and reduced (FcMeOH, δ_R) forms of the mediator, respectively. Cathodic offset current was compensated. Other conditions are as in Figure 4.2.3. Copyright © 2017 American Chemical Society.

In a region close to the substrate electrode (d < 25 µm) the concentration gradients were flattened. This can probably be attributed to the presence of the probe in close vicinity of the substrate surface hindering effective mass transport. It should be noted that for the 0.6 µm UME probe redox cycling effects would just come into play for tip-to-substrate distances smaller than 1 µm. It was found that the diffusion layer thickness derived from concentration profiles of FcMeOH and $FcMeOH^+$ were in good agreement. For a rotation speed of 16.7 s^{-1} a mean value for the diffusion layer thickness of 67.6 ± 0.7 µm was obtained. The diffusion layer thickness can also be calculated using the limiting currents at the substrate electrode according to equation (22):

$$\delta = \frac{D_R n F A c_0^*(R)}{I_D} \qquad (22)$$

where D_R is the diffusion coefficient of FcMeOH (R), n the number of transferred electrons, c_0^* the bulk concentration of R, F the Faraday constant, A the electrode surface area, and I_D the limiting current. Figure 4.2.5 shows the dependence of the diffusion layer thickness (for various ways of determination) on the rotation speed. The calculated errors increased dramatically for small and very high rotation speeds (f_{rot} < 10 s^{-1}; f_{rot} > 25 s^{-1}). This observation can be attributed to non-steady-state mass transprot for small rotation speeds and turbulences for high rotation speeds, respectively.

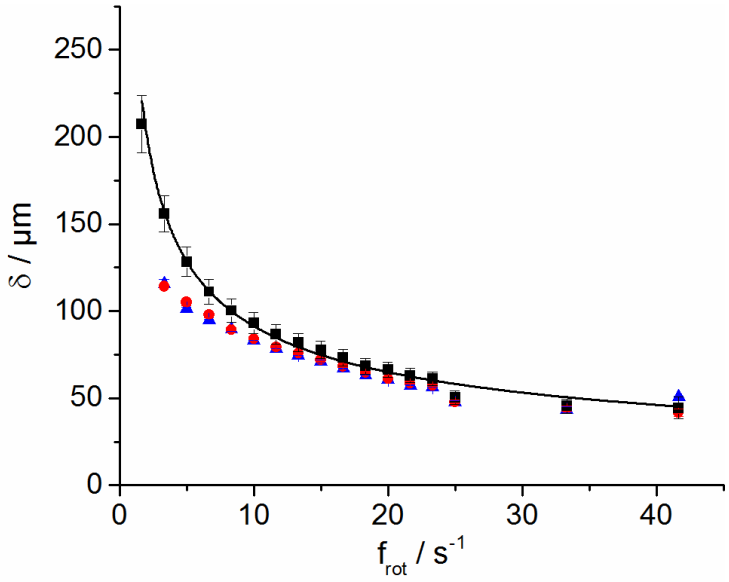

Figure 4.2.5: Thickness of the diffusion layer in the vicinity of a 2 mm Pt disk electrode ($E_{substrate}$= 0.45 V) studied by hydrodynamic SECM with a 0.6 µm diameter probe applying different rotation speeds. (■) Diffusion layer thickness calculated according to equation 1 based on chronoamperometric limiting currents (D_R = 7.2 ± 0.2 *10^{-10} m^2s^{-1}, A = 3.0 ± 0.2 mm^2; error bars calculated according to error propagation of ΔI_D, ΔD_R, ΔA) and (-) its mathematical fit (Allometric1 $(y = ax^b)$ $\delta \propto f_{rot}^{-0.49}$). The diffusion layer thicknesses derived from hydrodynamic SECM measurements are represented by ● for the SG/TC mode (δ_O, E_{UME} = 0 V) and by ▲ for the competition mode (δ_R, E_{UME} = 0.45 V). Error bars for ● and▲ correspond to standard deviations of repeated measurements (N = 3). All measurements were carried out in a solution containing 1.5 mM FcMeOH and 0.2 M KNO_3. Copyright © 2017 American Chemical Society.

The mathematical fit (black line in Figure 4.2.5) of δ as a function of f_{rot} based on limiting current measurements and calculations using eq. 22 is represented by $\delta \propto f_{rot}^{-0.49}$ showing a

nearly inversed square root dependence of the diffusion layer thickness on the rotation speed within our experimental setup.

Hydrodynamic SECM imaging

Hydrodynamic SECM enables a reproducible SG/TC imaging at a fixed plane within the diffusion layer of a large substrate electrode. This is illustrated in Figure 4.2.6 showing the contrast between measurements in quiescent solution and under forced convection. Under the former condition it was impossible to generate reproducible results in successive recordings due to the instability of the diffusion layer characteristics.

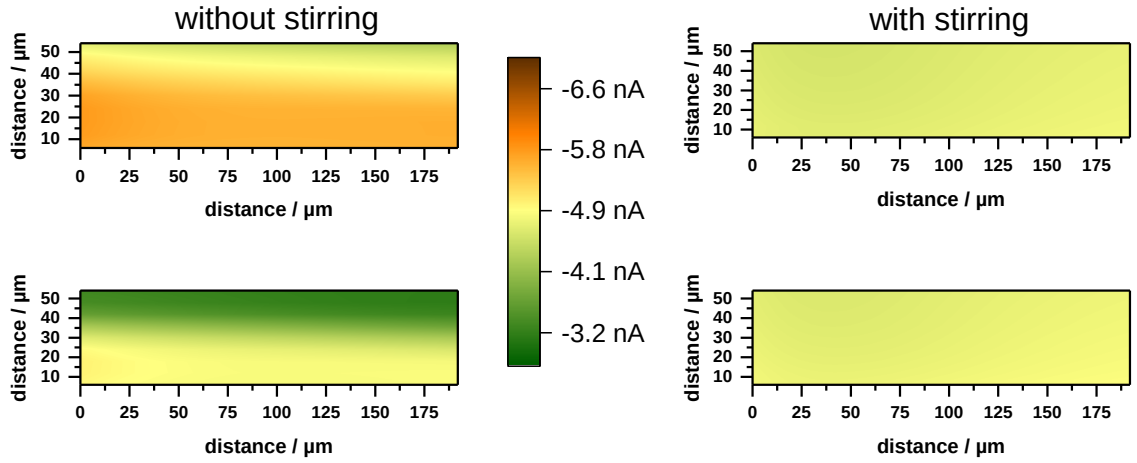

Figure 4.2.6: Successive SECM images in the SG/TC mode ($E_{substrate}$ = 0.45 V, E_{UME} = 0 V) within the diffusion layer of a 2 mm Pt disk substrate electrode. Left: SECM under quiescent conditions. Right: Hydrodynamic SECM applying a constant stirrer rotation speed (f_{rot} = 16.7 s^{-1}). All measurements were done in a fixed plane at a tip-to-substrate distance of ~28 µm using a 20 µm probe in a solution containing 1.5 mM FcMeOH and 0.2 M KNO_3. Copyright © 2017 American Chemical Society.

In contrast, hydrodynamic SECM resulted in very well-defined and reproducible SG/TC recordings. A uniform current signal of 4.9 ± 0.1 nA was detected at a constant tip-to-substrate distance of 28 µm applying a rotation speed of 16.7 s^{-1}. In a second imaging experiment the 2 mm Pt disk electrode was operated in a potential region of hydrogen evolution in 0.2 M KNO_3 solution ($E_{substrate}$ = -1.2 V). The H^+/H_2 couple was previously been used as mediator system in SECM experiments [45–48]. In our experiments the UME probe was set at a potential of -0.1

V where hydrogen is oxidized. Hydrodynamic SECM studies at a tip-to-substrate distance of 14 µm enabled a well-defined imaging of the Pt electrode surface as shown in Figure 4.2.7 (a). The same surface region was imaged in quiescent solution after adding FcMeOH (Figure 4.2.7 (b)).

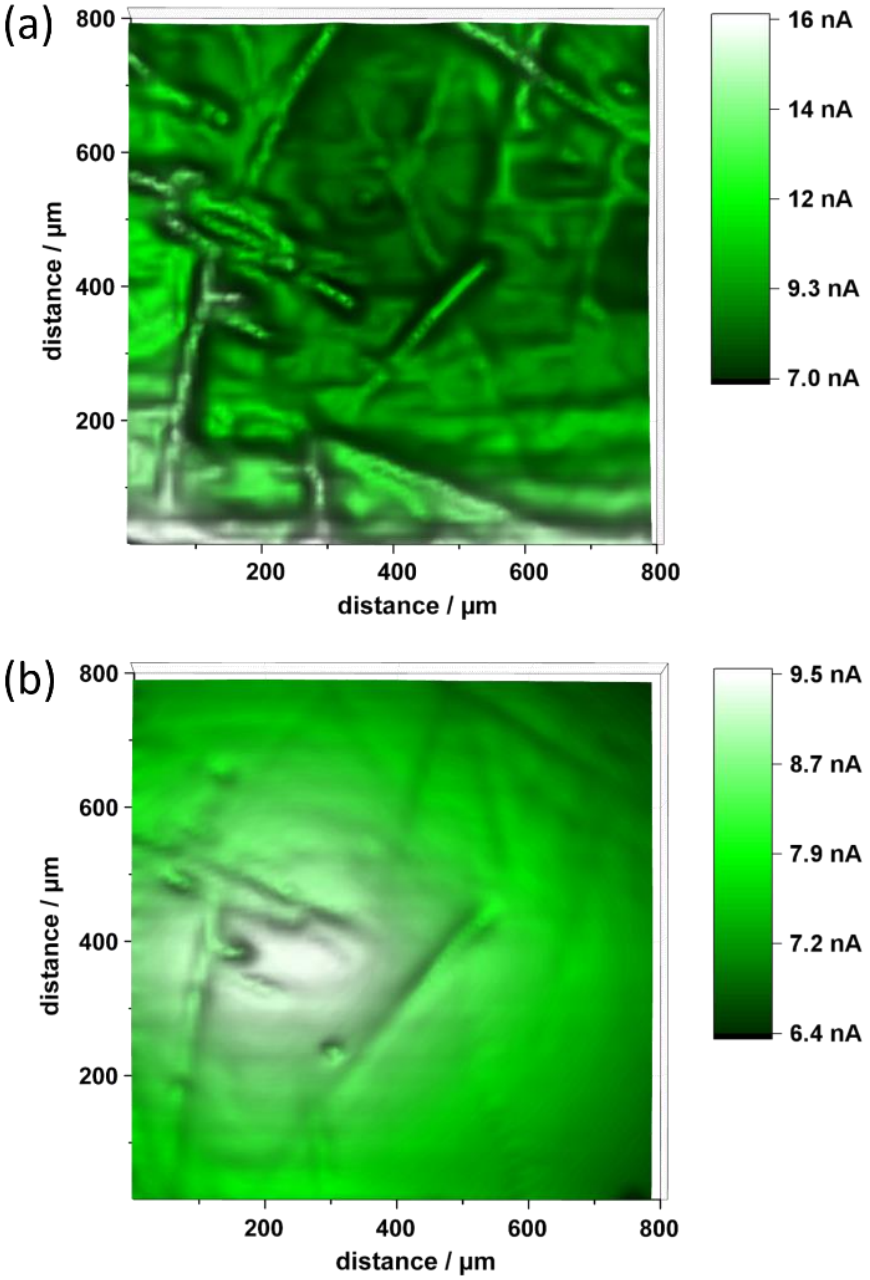

Figure 4.2.7: SECM images (distance ~14 µm) of a 2 mm Pt disk electrode using a 20 µm UME probe. (a) Hydrodynamic SECM image recorded in the SG/TC mode (E_{UME} = -0.1 V, $E_{substrate}$ = -1.2 V) with a constant stirrer rotation speed of 16.7 s^{-1}. The imaging is based on hydrogen evolution at the substrate electrode and hydrogen oxidation at the UME probe, 0.2 M KNO_3

was used as electrolyte. (b) SECM image in quiescent solution recorded in the positive feedback mode (E_{UME} = 0.5 V; substrate at open circuit potential) using 1.5 mM FcMeOH containing 0.2 M KNO_3. Copyright © 2017 American Chemical Society.

Both images reflect some morphological characteristics (scratches) of the Pt electrode surface. The contrast of the hydrogen based SG/TC recording under forced convection was clearly better than the conventional feedback-based imaging in quiescent solution. In addition, in the case of hydrogen-based imaging differences in local electrode activity towards hydrogen evolution could be identified.

4.2.4 Conclusion

In this work we demonstrated that SECM with forced convection introduced by high-precision stirring can be realized. The well-defined convective conditions led to stable diffusion layers in the vicinity of a large substrate electrode. Correspondingly, hydrodynamic SECM measurements enabled well-defined SG/TC measurements within the diffusion layer region as well as measurements in the competition mode. A complete characterization of the diffusion layer of a large substrate electrode was possible. Smaller (sub-µm) UME probes were found to be better suited for hydrodynamic SECM studies than larger probes (equal to or larger than 10 µm diameter) in the case of measurements with varying tip-to-substrate distances. The advantage of the sub-µm UMEs is the nearly convection independent voltammetric response within the hydrodynamic boundary layer near the substrate electrode. However, at constant tip-to-substrate distances larger probes (10 µm or 20 µm diameter) are also suitable for hydrodynamic SECM studies. Well-defined SECM SG/TC imaging at constant distance within the diffusion layer region of a large substrate electrode could be demonstrated. Preliminary studies based on hydrogen evolution at a 2 mm Pt disk electrode and oxidation of hydrogen at the UME probe in neutral solution illustrated that hydrodynamic SECM has a great potential to enhance and complement information obtained with conventional SECM modes and paves the way for new applications.

References

[1] J. Kwak, A.J. Bard, Scanning electrochemical microscopy. Apparatus and two-dimensional scans of conductive and insulating substrates, Anal. Chem. 61 (1989) 1794–1799.

[2] A.J. Bard, M.V. Mirkin, Scanning electrochemical microscopy, 2nd edition,CRC Press, Boca Raton, 2012.
[3] J. Kwak, A.J. Bard, Scanning electrochemical microscopy. Theory of the feedback mode, Anal. Chem. 61 (1989) 1221–1227.
[4] R.D. Martin, P.R. Unwin, Theory and experiment for the substrate generation tip collection mode of the scanning electrochemical microscope: Application as an approach for measuring the diffusion coefficient ratio of a redox couple, Anal. Chem. 70 (1998) 276–284.
[5] C. Amatore, S. Szunerits, L. Thouin, Mapping concentration profiles within the diffusion layer of an electrode: Part II. Potentiometric measurements with an ultramicroelectrode, Electrochem. Commun. 2 (2000) 248–253.
[6] D.T. Pierce, A.J. Bard, Scanning electrochemical microscopy. 23. Reaction localization of artificially patterned and tissue-bound enzymes, Anal. Chem. 65 (1993) 3598–3604.
[7] C.M. Sánchez-Sánchez, J. Rodríguez-López, A.J. Bard, Quantitative calibration of the SECM substrate generation/tip collection mode and its use for the study of the oxygen reduction mechanism, Anal. Chem. 80 (2008) 3254–3260.
[8] R.A. Lazenby, K. McKelvey, P.R. Unwin, Hopping intermittent contact-scanning electrochemical microscopy (HIC-SECM): Visualizing interfacial reactions and fluxes from surfaces to bulk solution, Anal. Chem. 85 (2013) 2937–2944.
[9] J. Rodríguez-López, M.A. Alpuche-Avilés, A.J. Bard, Interrogation of surfaces for the quantification of adsorbed species on electrodes: Oxygen on gold and platinum in neutral media, J. Am. Chem. Soc. 130 (2008) 16985–16995.
[10] K. Eckhard, X. Chen, F. Turcu, W. Schuhmann, Redox competition mode of scanning electrochemical microscopy (RC-SECM) for visualisation of local catalytic activity, Phys. Chem. Chem. Phys. 8 (2006) 5359–5365.
[11] C.G. Zoski, C.R. Luman, J.L. Fernández, A.J. Bard, Scanning electrochemical microscopy. 57. SECM tip voltammetry at different substrate potentials under quasi-steady-state and steady-state conditions, Anal. Chem. 79 (2007) 4957–4966.
[12] M.A. Mezour, R. Cornut, E.M. Hussien, M. Morin, J. Mauzeroll, Detection of hydrogen peroxide produced during the oxygen reduction reaction at self-assembled thiol-porphyrin monolayers on gold using SECM and nanoelectrodes, Langmuir 26 (2010) 13000–13006.
[13] R.C. Engstrom, M. Weber, D.J. Wunder, B. Robert, W. Sharon, Measurements within the diffusion layer using a microelectrode probe, Anal. Chem. 58 (1986) 844–848.
[14] N. Nioradze, J. Kim, S. Amemiya, Quasi-steady-state voltammetry of rapid electron transfer reactions microscope, Anal. Chem. 83 (2011) 828–835.
[15] A. Minguzzi, D. Battistel, J. Rodríguez-López, A. Vertova, S. Rondinini, A.J. Bard, S. Daniele, Rapid characterization of oxygen-evolving electrocatalyst spot arrays by the substrate generation/tip collection mode of scanning electrochemical microscopy with decreased O_2 diffusion layer overlap, J. Phys. Chem. C 119 (2015) 2941–2947.
[16] Y. Shen, M. Träuble, G. Wittstock, Detection of hydrogen peroxide produced during electrochemical oxygen reduction using scanning electrochemical microscopy, Anal. Chem. 80 (2008) 750–759.
[17] K. Eckhard, W. Schuhmann, Localised visualisation of O_2 consumption and H_2O_2 formation by means of SECM for the characterisation of fuel cell catalyst activity, Electrochim. Acta 53 (2007) 1164–1169.
[18] N. Baltes, L. Thouin, C. Amatore, J. Heinze, Imaging concentration profiles of redox-active species with nanometric amperometric probes: Effect of natural convection on

transport at microdisk electrodes, Angew. Chem. Int. Ed. 43 (2004) 1431–1435.
[19] S. Bi, B. Liu, F.R.F. Fan, A.J. Bard, Electrochemical studies of guanosine in DMF and detection of its radical cation in a scanning electrochemical microscopy nanogap experiment, J. Am. Chem. Soc. 127 (2005) 3690–3691.
[20] A.J. Bard, L.R. Faulkner, Electrochemical Methods: Fundamentals and applications, 2nd edition, John Wiley & Sons Inc., New York, 2001.
[21] F. Opekar, P. Beran, Rotating disk electrods, J. Electroanal. Chem. 69 (1976) 1–105.
[22] C.I. Banks, A.O. Simm, R. Bowler, K. Dawes, R.G. Compton, Hydrodynamic electrochemistry: design for a high-speed rotating disk electrode, Anal. Chem. 77 (2005) 1928–1930.
[23] S.D. Ahn, K. Somasundaram, H.V. Nguyen, E. Birgersson, J.Y. Lee, X. Gao, A.C. Fisher, P.E. Frith, F. Marken, Hydrodynamic voltammetry at a rocking disc electrode: Theory versus experiment, Electrochim. Acta 188 (2016) 837–844.
[24] J.A. Cooper, R.G. Compton, Channel electrodes — a review, Electroanalysis 10 (1998) 141–155.
[25] J.L. Melville, B.A. Coles, R.G. Compton, N. Simjee, J.V. Macpherson, P.R. Unwin, Hydrodynamics and mass transport in wall tube and microjet electrodes. Simulation and experiment for micrometer-scale electrodes, J. Phys. Chem. B 107 (2003) 379–386.
[26] H. Gunasingham, B. Fleet, Wall-jet electrode in continuous monitoring voltammetry, Anal. Chem. 55 (1983) 1409–1414.
[27] C.E. Banks, R.G. Compton, A.C. Fisher, I.E. Henley, The transport limited currents at insonated electrodes, Phys. Chem. Chem. Phys. 6 (2004) 3147–3152. d
[28] F. Marken, Y.-C. Tsai, B.A. Coles, S.L. Matthews, R.G. Compton, Microwave activation of electrochemical processes: convection, thermal gradients and hot spot formation at the electrode|solution interface, New J. Chem. 24 (2000) 653–658.
[29] O. Lioubashevski, E. Katz, I. Willner, Magnetic field effects on electrochemical processes: A theoretical hydrodynamic model, J. Phys. Chem. B 108 (2004) 5778–5784.
[30] P.U. Arumugam, A.J. Belle, I. Fritsch, Inducing convection in solutions on a small scale: Electrochemistry at microelectrodes embedded in permanent magnets, IEEE Trans. Magn. 40 (2004) 3063–3065.
[31] R. Cornut, S. Poirier, J. Mauzeroll, Forced convection during feedback approach curve measurements in scanning electrochemical microscopy: Maximal displacement velocity with a microdisk, Anal. Chem. 84 (2012) 3531–3537.
[32] C. Combellas, M. Fermigier, A. Fuchs, F. Kanoufi, Scanning electrochemical microscopy. Hydrodynamics generated by the motion of a scanning tip and its consequences on the tip current, Anal. Chem. 77 (2005) 7966–7975.
[33] S. Kuss, C. Kuss, D. Trinh, S. Brian, J. Mauzeroll, Forced convection during scanning electrochemical microscopy imaging over living cells: Effect of topographies and kinetics on the microelectrode current, Electrochim. Acta 110 (2013) 42–48.
[34] S. Kuss, D. Trinh, J. Mauzeroll, L. Danis, J. Mauzeroll, High-speed scanning electrochemical microscopy method for substrate kinetic determination: Method and theory, Anal. Chem. 87 (2015) 8096–8101.
[35] S. Kuss, D. Trinh, J. Mauzeroll, High-speed scanning electrochemical microscopy method for substrate kinetic determination: Application to live cell imaging in human cancer, Anal. Chem. 87 (2015) 8102–8106.
[36] P. Palatzky, F.-M. Matysik, Development of capillary-based SECM probes for the characterization of cell arrangements for electrochemically assisted injection, Electroanalysis 23 (2011) 50–54.

[37] F.-M. Matysik, Electrochemically assisted injection - A new approach for hyphenation of electrochemistry with capillary-based separation systems, Electrochem. Commun. 5 (2003) 1021–1024.
[38] D. Momotenko, F. Cortes-salazar, A. Lesch, G. Wittstock, H.H. Girault, Microfluidic push-pull probe for scanning electrochemical microscopy, Anal. Chem. 83 (2011) 5275–5282.
[39] T. Kai, S. Chen, E. Monterroso, F. Zhou, Continuous nanoflow-scanning electrochemical microscopy: Voltammetric characterization and application for accurate and reproducible imaging of enzyme-labeled protein microarrays, Anal. Chem. 87 (2015) 4523–4529.
[40] C. Lee, C.J. Miller, A.J. Bard, Scanning electrochemical microscopy: Preparateion of submicrometer electrodes, Anal. Chem. 63 (1991) 78–83.
[41] A.M. Bond, M. Fleischmann, J. Robinson, Electrochemistry in organic solvents without supporting electrolyte using platinum microelectrodes, J. Electroanal. Chem. 168 (1984) 299–312.
[42] P. Vatsyayan, C. Iffelsberger, C.C. Mayorga, F.-M. Matysik, Imaging of localized enzymatic peroxidise activity over individual unbiased gold nanowires by scanning electrochemical microscopy, Anal. Methods 8 (2016) 6847–6855.
[43] Y. Shao, M.V. Mirkin, Probing ion transfer at the liquid/liquid interface by scanning electrochemical microscopy (SECM), J. Phys. Chem. B. 102 (1998) 9915–9921.
[44] F.-M. Matysik, H. Emons, Convection independent detection with voltammetric single microdisk electrodes, Electroanalysis 4 (1992) 501–506.
[45] J. Zhou, Y. Zu, A.J. Bard, Scanning electrochemical microscopy - Part 39. The proton/hydrogen mediator system and its application to the study of the electrocatalysis of hydrogen oxidation, J. Electroanal. Chem. 491 (2000) 22–29.
[46] C. Zoski, Scanning electrochemical microscopy: Investigation of hydrogen oxidation at polycrystalline noble metal electrodes, J. Phys. Chem. B 107 (2003) 6401–6405.
[47] U. Mengesha, M. Edward, P. Dauphin, M. Danaie, G.A. Botton, J. Mauzeroll, Local flux of hydrogen from magnesium alloy corrosion investigated by scanning electrochemical microscopy, J. Electroanal. Chem. 721 (2014) 121–127.
[48] R.F. Schaller, S. Thomas, N. Birbilis, J.R. Scully, Spatially resolved mapping of the relative concentration of dissolved hydrogen using the scanning electrochemical microscope, Electrochem. Commun. 51 (2015) 54–58.

4.3. Numerical simulation and characterization of the convection for hydrodynamic scanning electrochemical microscopy

4.3.1 Introduction

In many electrochemical techniques forced convection is used to move the liquid with respect to the electrode to generate a convective mass transport of reactants and products. Such methods are called hydrodynamic methods and provide an efficiently attained steady state and an increased rate of mass transport at the electrode surface. These advantages come at the cost of a more difficult construction and theoretical treatment of hydrodynamic systems. The theoretical treatment involves solving hydrodynamic problems like the flow velocity profile within the electrochemical cell prior to the electrochemical problems [1]. Numerical simulations are frequently used to solve electroanalytical problems or to describe and characterize velocity profiles especially if only steady-state solutions are desired [2]. Furthermore simulations are used in SECM to gain detailed information about experimental feedback currents [3–5].

For the computation with COMSOL Multiphysics of the velocity profile within the electrochemical cell of the SECM the Navier-Stokes equations were used [6]. The momentum equation reads

$$\rho \frac{\partial u}{\partial t} + \rho(u \cdot \nabla)u = \nabla \cdot [-pI + \mu(\nabla u + (\nabla u)^T] + F_v. \qquad (32)$$

In this equation ρ [kg m^{-3}] is the fluid density, u [m s^{-1}] is the velocity vector, I is the identity matrix, μ [Pa s^{-1}] is the dynamic viscosity, t is the time, T the temperature and F_v [N] is the volume force vector. The vector operator ∇ can be written as,

$$\nabla = i\frac{\partial}{\partial x} + j\frac{\partial}{\partial y} + k\frac{\partial}{\partial z} \qquad (33)$$

where i, j, k are the unit vectors along the axis and x, y, z [m] is the distance in a three-dimensional Cartesian space. The continuity equation is a statement of incompressibility, which means that the ρ is constant within time and space with the velocity vector.

$$\rho \nabla \cdot u = 0 \qquad (34)$$

4.3.2 Computational Setup

Flow solver

Simulations were carried out with COMSOL Multiphysics 5.2™ with the rotating machinery, laminar flow module study for the “Frozen Rotator” with the stationary solver 1 and nonlinear

solver. In table 4.3.1 all dimensions of the electrochemical cell and numerical settings for the simulation of the velocity profile are given. Simulations were carried out for different rotation speeds (f_{rot} = 5, 10, 15, 20 s^{-1}). In Fig. 4.3.1 the geometry of the electrochemical cell is presented. The model for the simulation of the hydrodynamic environment within the electrochemical cell consisted of 10^5 grid cells and was verified with numerical and experimental methods.

Table 4.3.1: Model dimensions and settings.

Dimension	value / mm
Hight	6
Width	24
Length	38
Radius of the stirrer	1.5
Distance (bottom of the cell - stirrer)	1
Position of the stirrer in (X/Y)	0/0
Position model basis edge in (X/Y)	-7/-10
Top diameter UME	0.1
Bottom diameter UME	0.85
Distance UME - substrate	0.01
Boundary conditions	
Top wall	slip
All other walls	no slip
Material	water (liquid)
Meshing	
Stirrer, UME and cell bottom	normal
Substrate electrode	finer (min. element size: 0.005 mm)
All other walls	coarse

Simulations were carried out using an Acer Aspire V5-573G Laptop with Windows 10 (64-bit), Intel® Core™ i5-4200U 1.6 GHz with Turbo Boos up to 2.6 GHz, NVIDIA® GeForce™ GT 750M with 4 GB dedicated VRAM, 8 GB DDR3 L Memory and 500 GB HDD. The computation time was up to 16 min depending on the applied rotational speed.

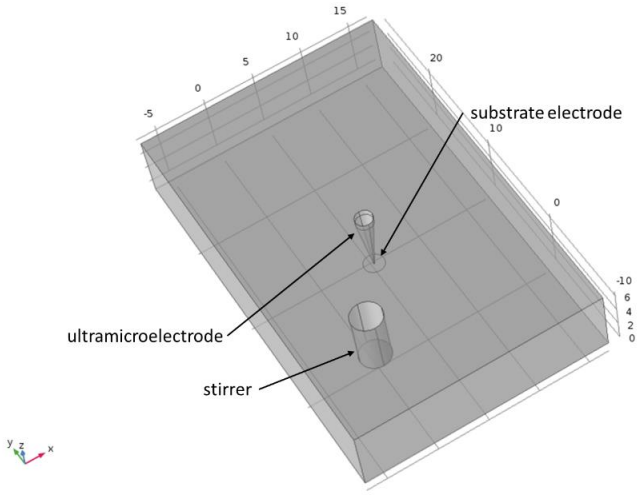

Figure 4.3.1: Schematic representation of the model for the simulation of the hydrodynamic environment during stirring of water within the electrochemical cell. The dimensions are given in mm.

Setup for numerical verification model

A simplified symmetric model of stirred water in a cube as presented in Fig. 4.3.2 was used to verify the reliability of the numerical simulation. Near the stirrer, the mean flow velocity of the water equals the velocity of the stirrer surface. This enables the comparison of the computed results for the mean flow velocity of the liquid with the stirrer velocity. The velocity of the surface of the stirrer v_a can be calculated according eq. 35.

$$v_a = 2\pi a f_{rot} \tag{35}$$

The applied settings for the simulation are listed in table 4.3.2. A rotational speed of f_{rot} = 1 s^{-1} was used.

Table 4.3.2: Model dimensions and setting for simplified model.

Dimension	value / mm
Height/width/length	10
Radius of the stirrer	1.5
Distance (bottom of the cell - stirrer)	1
Position of the stirrer in (X/Y)	0/0
Position model basis edge in (X/Y)	-5/-5
Boundary conditions	
top wall	slip
all other walls	no slip
Material	water (liquid)
Meshing	coarser (19288 grid cells)

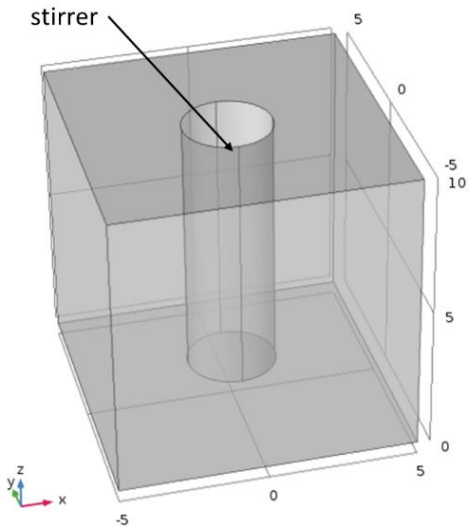

Figure 4.3.2: Schematic representation of the simplified model for the numerical verification. The dimensions are given in mm.

Setup for experimental verification model

Principle

As reported in [7], the current at a 25 µm UME is inflected by the local mean velocity of the stirred mediator solution. The higher the mean velocity the higher was the current. To verify the numerical result for the mean velocity profile in water an electrochemical experiment was performed. The current of a 25 µm UME approaching the substrate electrode in the presence of applied forced convection was recorded and compared to the mean velocity profile extracted from the simulation applying the same rotational speed. Since during the approach, the UME traverse the entire liquid phase vertically, the obtained current profile reflects the mean velocity profile.

Instrumentation and Chemicals

For all electrochemical experiments a commercial SECM system CHI 920C (CH Instruments, Austin, USA) with an electrochemical cell made of PTFE was used. The high-precision stirring device and its integration was carried out as reported [7]. For SECM experiments an aqueous solution of 1.5 mM ferrocene methanol (FcMeOH, 99 %, ABCR, Karlsruhe, Germany) and 0.2 M KNO_3 (Merck KGaA, Darmstadt, Germany) was used as mediator solution. Solutions were

prepared with ultrapure water with a resistivity higher than 18 MΩ cm (membraPure, Bodenheim, Germany). For measurements a three-electrode setup with an Ag/AgCl reference electrode with 3 M KCl and a Pt counter electrode was used. The potential applied at the UME was 0.3 V.

Measurement

Prior to the approach, the UME was placed above the center of the substrate electrode and retracted outside of the mediator solution. The PAC was recorded with constant approach speed of 100 µm s^{-1} and forced convection with a stirrer rotation speed of f_{rot} = 15 s^{-1} was applied. The stirrer rotation speed was kept the same for both the experimental and the numerical approaches.

4.3.3 Results and discussion

Numerical verification of the model

Figure 4.3.3 shows the results of the simulation of stirred water in a cube. The mean velocity around the stirrer shaft showed a uniform acceleration of the water. The highest flow velocity from the water, extracted from the simulation (v = 9.425 mm s^{-1}), equaled the surface velocity of the stirrer at the rotation speed of f_{rot} = 1 s^{-1}. The inset shows that the flow velocity profile of the water at the end of stirrer (dashed line along y-axis) equals the calculated velocity of the stirrer surface. The arrows in the image on the left side represents streamlines. The direction of the arrow indicates the direction of the stream and the thickness and length the mean velocity. It is shown that the velocity distribution in the water is radial near the stirrer and becomes more cubic like at the boundaries of the cube. These results enhanced the reliability of the numerical simulation.

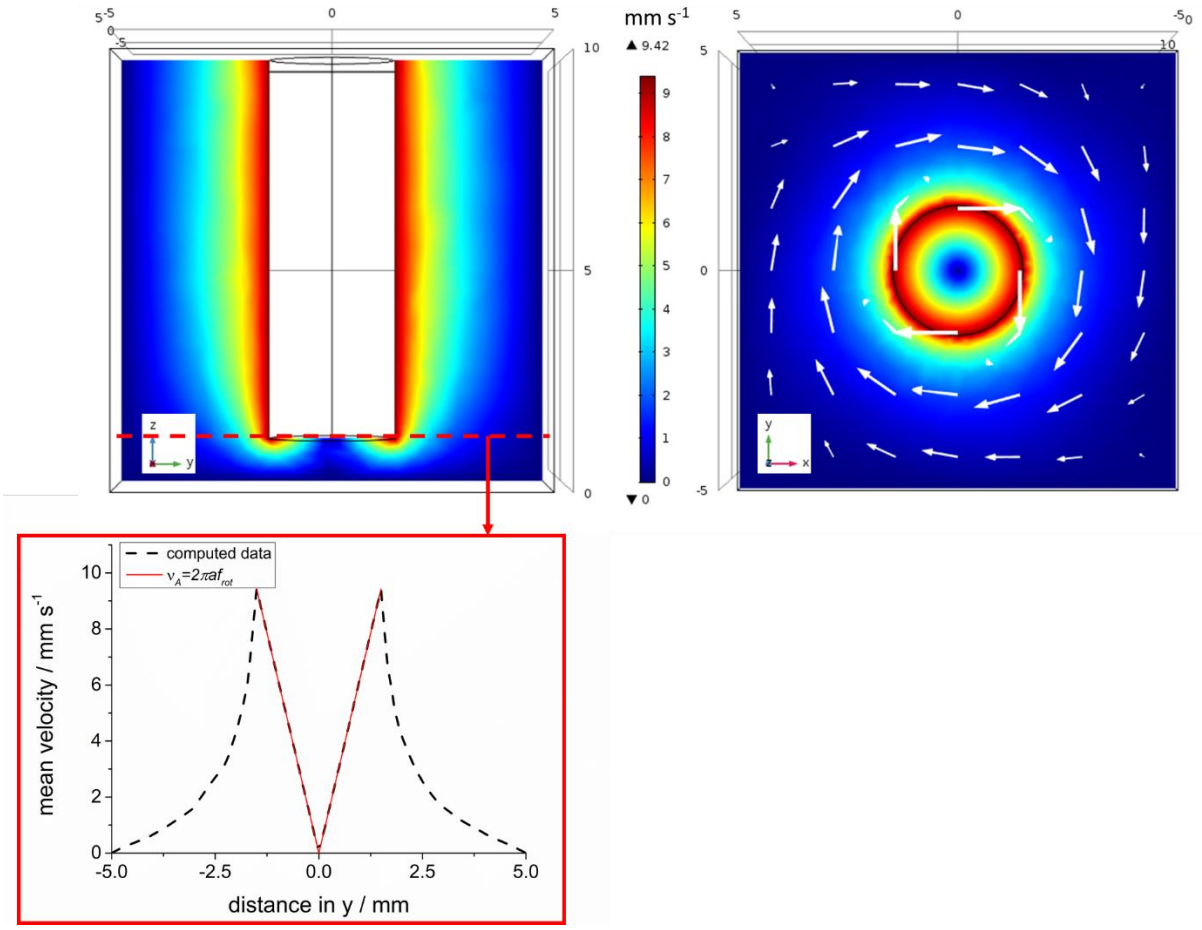

Figure 4.3.3: Numerical simulation of the convection within a cube. Contour plot of the mean flow velocity profile of water stirred at f_{rot} = 1 s^{-1} with a cylindrical stirrer (3 mm diameter), left: side view, right: top view. The arrows indicate the streamlines. Inset: comparison of the computed mean velocity along y-axis (dashed line) extracted from simulation with the angular velocity of the stirrer. The dimensions are in mm.

Experimental verification of the model

The experimental verification of the hydrodynamic simulation model was achieved by comparison of the recorded current of a 25 µm UME during approach towards the substrate electrode with the mean flow velocity profile extracted from the simulation. The plot presented in Fig. 4.3.4 shows a good correlation of the measured current with the mean velocity of the liquid extracted from simulations. The non-linear relation of the current and the mean flow velocity prevented quantitative measurements of the local velocity. However, the qualitative agreement showed the reliability of the computed simulations.

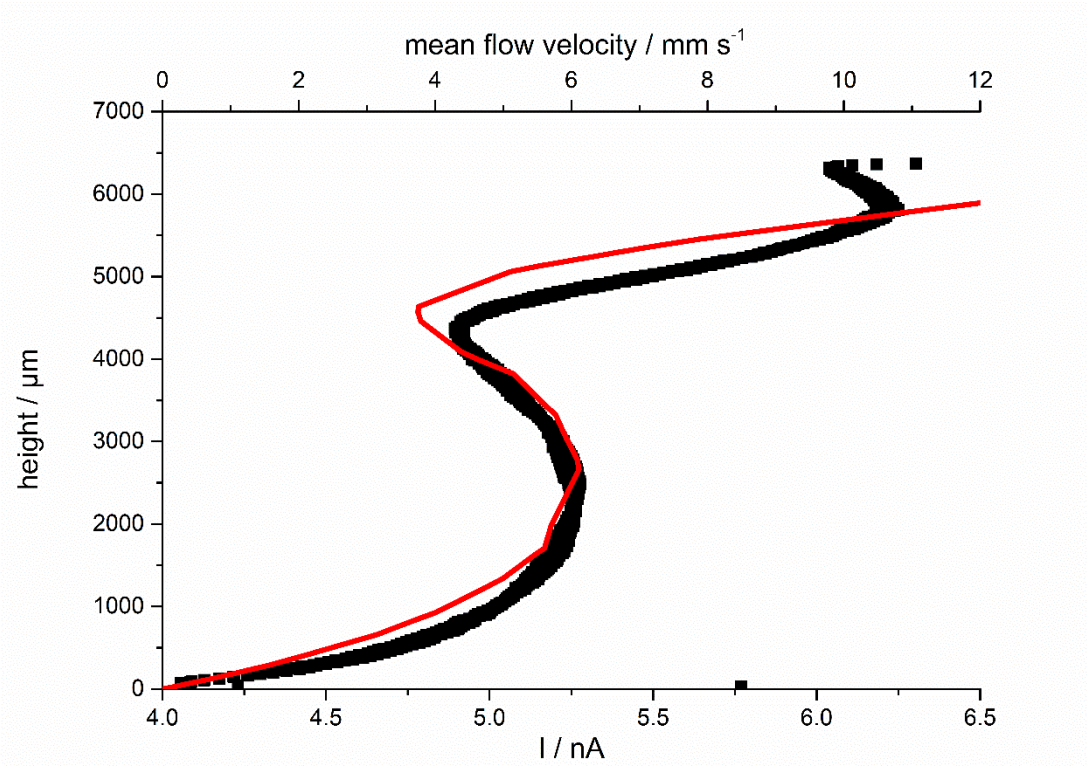

Figure 4.3.4: Comparison of the mean flow velocity profile above the substrate electrode of water stirred at f_{rot} = 15 s^{-1} (red line) extracted from simulation with the current recorded at a 25 µm UME approaching the substrate electrode (black squares). Adapted from [8].

Hydrodynamic environment near the substrate electrode

The numerical simulation of the convective situation within the electrochemical cell was performed neglecting the UME. The results presented in Fig. 4.3.5(a) show a uniform mean velocity of the water at different heights above the substrate electrode. The flow of the water is directed towards the stirrer. The application of different rotation speeds affected the mean velocity near the substrate electrode dramatically as shown in Fig. 4.3.5(b). A higher rotational speed resulted in an increased convection above the substrate. Furthermore, the presented data shows that within the working distance of SECM measurements, relatively low mean flow velocities were present. Since SECM experiments were usually performed near the substrate electrode the assumption of an even flow of the water causing the formation of steady-state diffusion layers in SG/TC mode and the control of their thickness in hydrodynamic SECM experiments is supported by these simulations.

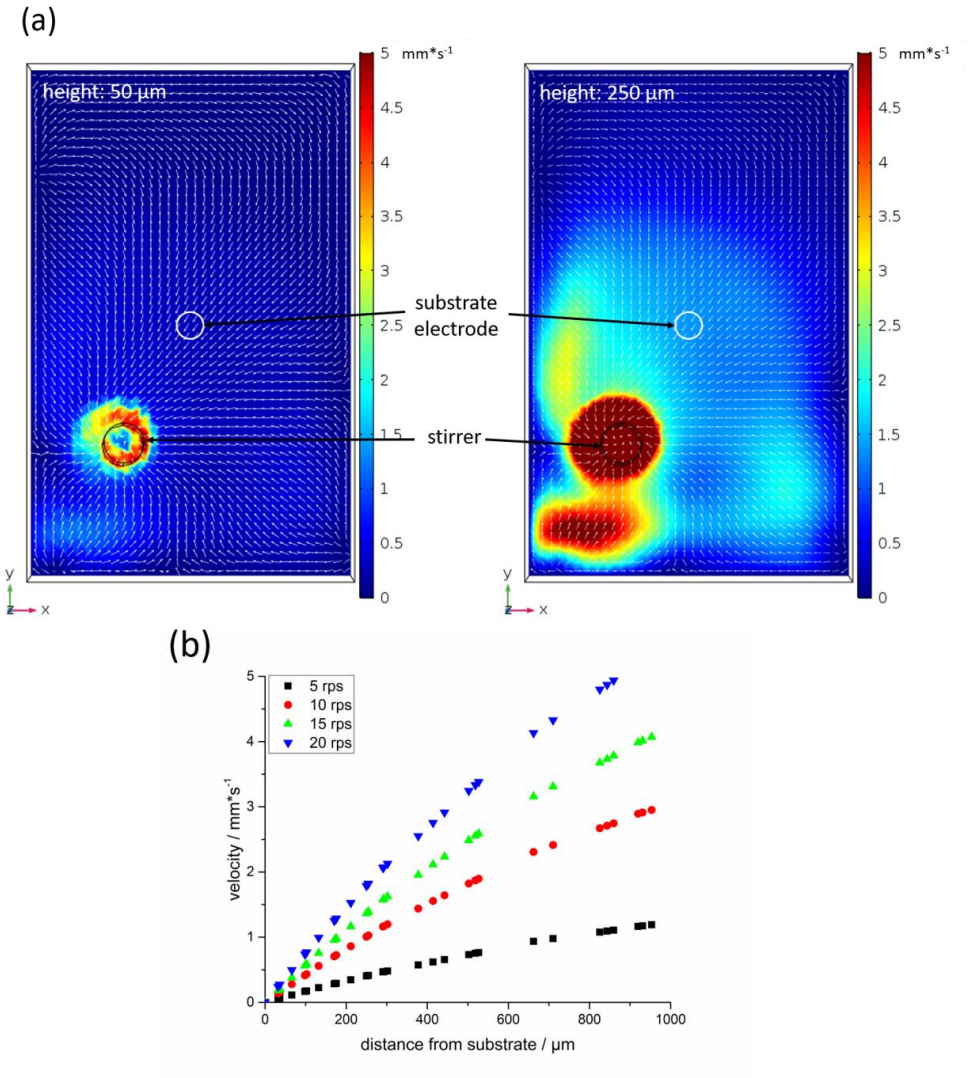

Figure 4.3.5: Numerical simulation of the convection within the electrochemical cell. (a) Contour plots of the mean flow velocity of water stirred at f_{rot} = 15 s^{-1} at a distance of 50 µm (left) and 250 µm (right) above the bottom of the cell. The arrows indicate the streamlines. (b) Magnitude of the flow velocity above the center of the substrate electrode for different stirrer rotation speeds ranging from 5 rpm to 20 rpm. Adapted from [7]. Copyright © 2017 American Chemical Society.

The next step was to integrate the UME into the model to study the effects caused by its presence. The movement of the UME during a scan across the substrate is not implemented. The simulation assumed a fixed UME. As shown in Fig. 4.3.6 at a height of 1 mm above the substrate, the UME affected the flow within the electrochemical cell. The zoomed contour plot represents the situation at a typical tip-to-substrate distance of 20 µm. The simulation showed

that the UME caused a local disturbance of the velocity profile. Directly below the UME (0.1 mm diameter) only a slow movement of the water occurred. Before and after the tip of the UME, in respect to the stirrer, the mean velocity of the liquid was decreased. The black arrows represent streamlines of the flow. The UME caused distortions in X and Y direction, but the arrows indicated that only negligible distortion of the laminar flow in Z direction. The indicated scan direction illustrates that during the SECM imaging process the UME moves inside a region with a higher velocity this shows that SECM imaging within a steady-state diffusion layer delivers reliable results.

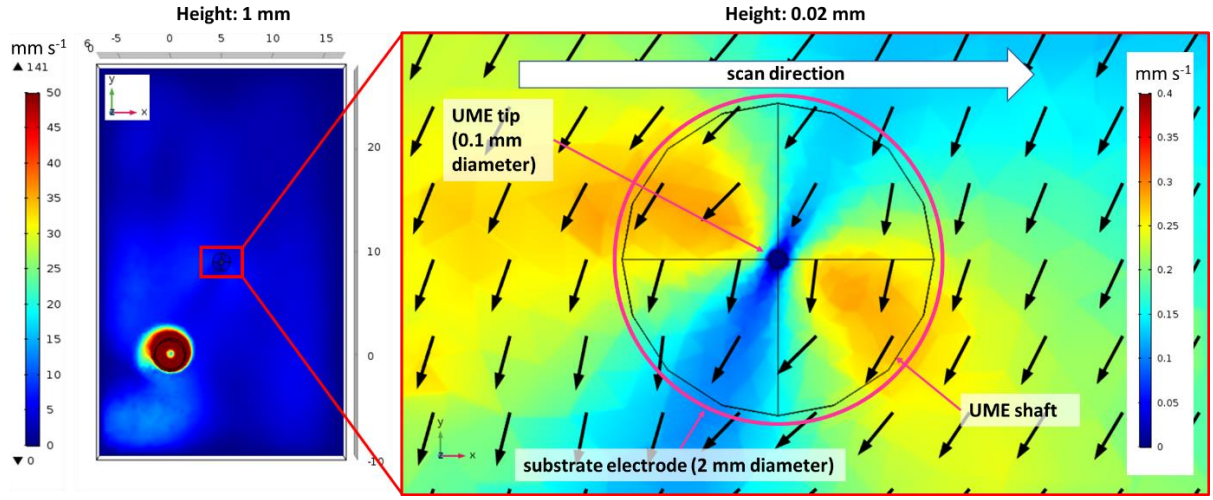

Figure 4.3.6: Numerical simulation of the convection within the electrochemical cell. Contour plots of the magnitude of the mean flow velocity of water stirred at f_{rot} = 15 s^{-1} at different distances. The zoomed contour plot (right) shows the mean flow velocity above the center of the substrate electrode at a tip-to-substrate distance of 20 µm with an UME present in the water. The arrows indicate the streamlines.

4.3.4 Conclusion

The numerical and experimental verification proved the reliability of the simulation. The simulations showed a uniform convection near the substrate electrode. This supports the assumption of steady-state diffusion layers controlled by the rotational speed of the stirrer during SECM experiments. Further simulations showed negligible effects on the laminar flow caused by the presence of the UME. The application of UMEs with thinner insulation could help reducing the effects of its presence. Furthermore, an extension of the simulation to other

cell and substrate geometries as well as the incorporation of electrochemistry into the simulation can provide interesting and valuable information for future experiments applying the hydrodynamic mode for SECM.

References

[1] A.J. Bard, L.R. Faulkner, Electrochemical methods: Fundamentals and applications, 2nd edition, John Wiley & Sons Inc., New York, 2001.

[2] E.J.F. Dickinson, H. Ekström, E. Fontes, COMSOL Multiphysics®: Finite element software for electrochemical analysis. A mini-review, Electrochem. Commun. 40 (2014) 71–74.

[3] O. Sklyar, G. Wittstock, Numerical simulations of complex nonsymmetrical 3D systems for scanning electrochemical microscopy using the boundary element method, J. Phys. Chem. B 106 (2002) 7499–7508.

[4] O. Sklyar, A. Kueng, C. Kranz, B. Mizaikoff, A. Lugstein, E. Bertagnolli, G. Wittstock, Numerical simulation of scanning electrochemical microscopy experiments with frame-shaped integrated atomic force microscopy-SECM probes using the boundary element method, Anal. Chem. 77 (2005) 764–771.

[5] Q. Fulian, A.C. Fisher, G. Denuault, Applications of the boundary element method in electrochemistry: Scanning electrochemical microscopy, J. Phys. Chem. B 103 (1999) 4387–4392.

[6] P.M. Gresho, R.L. Sani, Incompressible flow and the finite element method. Volume 1: Advection-diffusion and isothermal laminar flow, John Wiley and Sons Inc., New York, (1998).

[7] C. Iffelsberger, P. Vatsyayan, F.-M. Matysik, Scanning electrochemical microscopy with forced convection introduced by high-precision stirring, Anal. Chem. 89 (2017) 1658–1664.

[8] M.A. Wetzel, Elektrochemische Charakterisierung eines hydrodynamischen Systems, Bachelorthesis, University of Regensburg, 2017.

4.4 Detection and imaging of reactive oxygen species associated with the electrochemical oxygen evolution by hydrodynamic scanning electrochemical microscopy

Christian Iffelsberger, Timo Raith, Preety Vatsyayan, Vlastimil Vyskočil, and Frank-Michael Matysik

Electrochimica Acta 281 (2018) 494-501

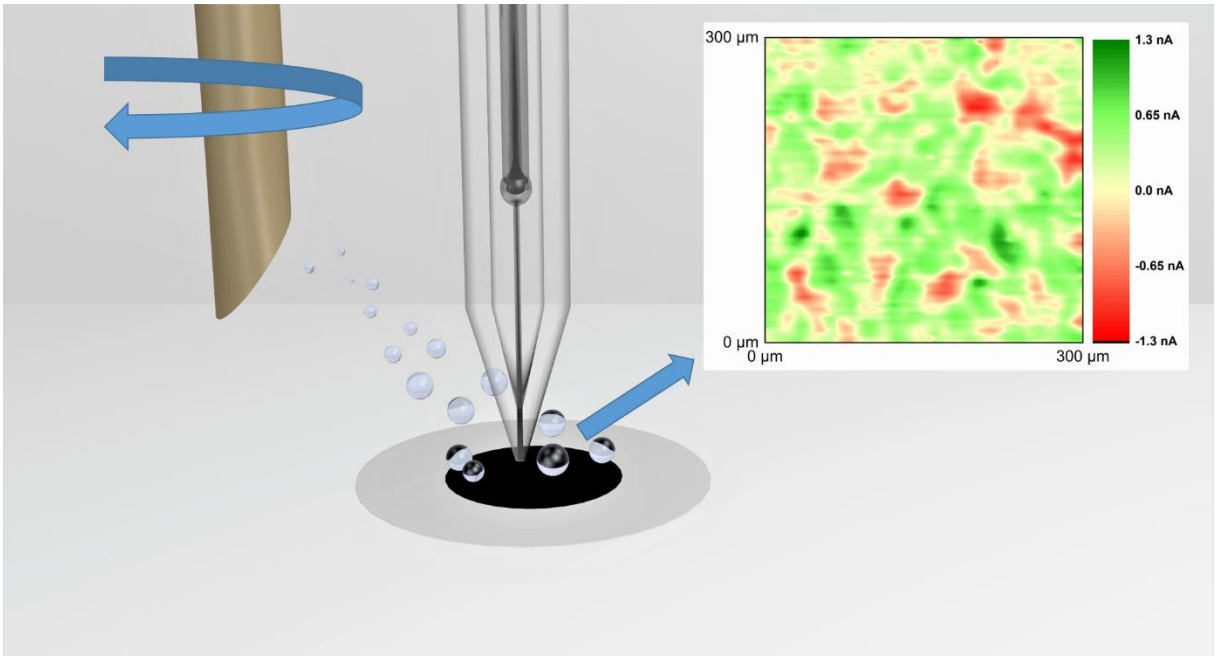

Abstract

Hydrodynamic scanning electrochemical microscopy (SECM) was applied for the characterization of Pt and boron-doped diamond (BDD) macroelectrodes operated in a potential region producing reactive oxygen species (ROS) during oxygen evolution reaction (OER). Forced convection introduced by high-precision stirring enabled the formation of a stable diffusion layer of electrochemically produced species and tip-substrate voltammetry was used for the detection of different ROS species produced during OER at BDD. Hydrodynamic SECM imaging in substrate generation/tip collection mode revealed local differences in the production of the ROS species across the BDD electrode surface.

4.4.1 Introduction

Reactive oxygen species (ROS), such as hydroxyl radical (·OH), hydrogen peroxide (H_2O_2) and superoxide (O_2^-), are of immense scientific interest because of their oxidative power and their omnipresence in living cells. In living aerobic organism, ROS are generated as byproducts of the oxygen metabolism [1] and are involved in many reaction pathways throughout the cell life, starting from proliferation and differentiation [2] to self-protection [3] and signaling [4,5] until apoptosis [6]. For the artificial production of ROS, many methods are known [7]. One prominent and frequently used method to produce large amounts of free radicals is the Fenton [8] or the more advanced Fenton-like reaction. Here, free ·OH is generated due to the catalytic decay of H_2O_2 by transition metals ions [9]. The H_2O_2 decay can be accelerated by UV radiation which is then called photo-Fenton reaction [10]. However, for some applications like wastewater treatment or the study of degradation mechanism of organic compounds, the use of chemical reagents or catalysts has some disadvantages [11]. Therefore, electrochemical approaches to produce ROS are intensively discussed in the literature [11–16] for wastewater treatment. It is well known that during water oxidation, short-lived intermediates and strong oxidants like ·OH, $\cdot HO_2$, H_2O_2 and O_3 are produced. Many side, cross, and extermination reactions with high reaction rates (e.g. $k(\cdot OH + \cdot OH) = 5.5 \cdot 10^9$ L mol^{-1} s^{-1} [17], $k(\cdot OH + \cdot HO_2) = 6.6 \cdot 10^9$ L mol^{-1} s^{-1} [17], $k(\cdot HO_2 + \cdot HO_2) = 5.5 \cdot 10^5$ L mol^{-1} s^{-1} [18]) are reported to be involved in further reaction steps so that H_2O_2, O_2 and O_3 are the relatively stable products of water oxidation.

According to previous reports, the electrode materials and their capability for ROS production can be classified into two types [11]. At active electrode materials like Pt, the surface atoms continually cycle the oxidation states during the reaction. Active materials are less efficient in terms of ·OH production [19]. Composed with the natural characteristics of diamond, such as high stability, hardness and an inert surface, boron-doped diamond (BDD) electrodes are an example of an inactive electrode material exhibiting attractive electrochemical properties [20]. The wide potential window in aqueous solution is important for many electrochemical studies and allows for their application in electrochemical advanced oxidation processes (EAOP) [21]. The surface atoms of inactive materials do not change their oxidation state during the electrochemical reaction. This means that the ·OH is physically adsorbed at the surface, resulting in a high overpotential for the oxygen evolution reaction (OER) associated with a large amount of free ·OH [22]. Studies showed that BDD [23–28] is a complex electrode

material with varying properties like defects, impurities and conductivity affecting its electrochemical behavior. Recently, it was proved that especially the boron dopant level is very important and can directly be correlated with the electrochemical activity of the BDD [29,30].

In many studies regarding the effectivity of ROS generation during anodic oxidation at different electrode materials, the detection was performed indirectly by measuring the degradation of organic compounds [15,31,32] often with aromatic structural elements like dyes, pharmaceuticals, herbicides, pesticides and even DNA. The different and complex degradation mechanisms are a difficulty for the determination of the produced ROS. Spin trapping [33], however, is a common technique for direct detection of produced radical species. The direct detection of ROS can also be performed with rotating ring disc electrodes (RRDE) [34], where the reactive species are generated at the disk electrode and detected directly at the ring electrode. In all these approaches, the results provide an overview of the capability for radical production of the whole electrode area. Local differences in electrode reactions at different electrode structures or compositions are neglected.

Since its introduction by Bard and coworkers in 1989 [35], scanning electrochemical microscopy (SECM) evolved to a powerful tool to image surface topography and to localize differences in the reactivity [36]. The occurrence of ·OH during oxygen reduction reaction (ORR) or H_2O_2 reduction at Pt ultramicroelectrodes was shown by Noël et al. [37] and as one consequence a dissolution of Pt was proved [38]. Zhao et al. [39] localized an increased ROS production over the cell core structure in living RAW264.7 cells. Salamifar et al. [37] used a combined scanning electrochemical and fluorescence microscope for detection of reactive oxygen species in prostate cancer cells and Amatore´s workgroup [40] showed the release of reactive oxygen from stimulated macrophage. The interrogation mode [41] was widely used to study and quantify surface adsorbed ·OH by electrochemical titration of the radical after its formation at a micro-sized substrate [42,43]. The indirect detection of ·OH during OER at a BDD microarray was done by Khamis et al. [44] via reduction of the intermediate peroxydisulfate.

In addition to the classical feedback mode [45], the generation/collection mode [46] is a standard mode for the characterization of (electrode) surfaces. In the substrate generation/tip collection (SG/TC) mode, a substrate-generated species is detected at the SECM probe at a diffusion-limited rate. Analogous to the RRDE, the tip-substrate voltammetry (TSV) [47,48] is an approach with a local resolution using SG/TC mode. Here, the probe is positioned few

micrometers above the studied substrate. The potential applied at the substrate is swept while the potential at the probe is kept constant for an amperometric detection of the electrochemically produced species arising from the substrate. In quiescent solution, the substrate electrode current is transient due to the growth of the diffusion layer thickness with time. As previously shown, the introduction of forced convection by high-precision stirring enabled the generation and characterization of steady-state diffusion layers above a 2 mm Pt disk electrode [49]. With this experimental approach, the localization of an increased hydrogen production at surface defects of a Pt electrode was possible. The hydrodynamic SECM imaging revealed a more detailed view concerning the surface defects compared to imaging in conventional feedback mode in quiescent solution.

In this work, hydrodynamic SECM as a method for the study of the electrochemical production of ROS associated with the OER is presented. This approach enables a local and direct detection of ROS. The effect of forced convection for the characterization of production and detection potentials for ROS is presented. The exploitation of hydrodynamic effects enables the imaging of ROS production at macroscopic substrate electrodes using the SG/TC mode. The applied techniques were used to study and compare Pt and BDD electrodes concerning their capability to produce ROS.

4.4.2 Experimental

Chemicals

For feedback mode imaging and probe positioning, an aqueous solution of 1.5 mM ferrocene methanol (FcMeOH, 99 %, ABCR, Karlsruhe, Germany) and 0.2 M KNO_3 (Merck KGaA, Darmstadt, Germany) was used as mediator solution. In studies involving oxygen and ROS production, a solution of 0.2 M perchloric acid ($HClO_4$, 70 %, Merck KGaA, Darmstadt, Germany) served as an electrolyte. All chemicals were of analytical reagent grade. The solutions were prepared with ultrapure water with a resistivity higher than 18 MΩ cm (membraPure, Bodenheim, Germany).

Instrumentation

All electrochemical experiments were conducted with the setup shown in Fig. 4.4.1 using a commercial SECM system CHI 920C (CH Instruments, Austin, USA) with an electrochemical cell made of PTFE. The high-precision stirring device and its integration was carried out as

mentioned earlier [49]. Briefly, the stirring system consisted of an electrical motor (2250S012BX4 CSD 3830, BL- DC- Motor with integrated motion controller, Dr. Fritz Faulhaber GmbH & Co. KG, Schönaich, Germany) and a homemade rotating cylinder (PEEK; length: 9.7 cm, 3 mm diameter, beveled at the end with 45°). A stirrer guide made of borosilicate glass tube (length: 2 cm, ID: 3 mm, OD: 6 mm) completed the stirring system. For the alignment of the stirrer, a 3D-printed sliding cap was used and removed afterwards. A 2 mm diameter Pt disk electrode (CH Instruments, Austin, USA) and a 3 mm diameter BDD disk (Windsor Scientific, Windsor, Great Britain) insulated by heat shrinking (cavity diameter for BDD: 2.9 mm, outer diameter: 7 mm, length: 27 mm) into a PTFE cylinder were used as substrates. An Ag/AgCl/ 3M KCl electrode served as reference and a Pt-wire as counter electrode. To prevent interferences from chloride oxidation in TSV experiments, the reference electrode was immersed in a separate glass vial with a fused silica capillary (length: approx. 15 cm, ID: 150 µm, OD: 360 µm) acting as a salt bridge. The vial was filled with 0.2 M $HClO_4$. All experimental potentials refer to the used reference electrode. Prior to all experiments, the Pt substrate electrode was polished with 0.3 µm alumina suspension on a polishing cloth (TexMed, Buehler, Lake Bluff, USA) and the BDD electrode was cleaned by cycling the electrode potential 10 times between -1.5 and 2.5 V in 1 M H_2SO_4. Ultramicroelectrodes (UME) with electrode diameters of 12.5 and 25 µm and outer diameters of about 50 µm were fabricated following the procedure described elsewhere [50]. For SECM imaging, the tip-to-substrate distance was calculated from positive feedback approaches with the equation published by Shao et al. [51]. The atomic force microscopic (AFM) image was obtained with Nanosurf easyScan 2 (Nanoscience Instruments, Phoenix, USA) and PPP-NCLR cantilevers (Nanoscience Instruments, Phoenix, USA) in the tapping mode. Scanning electron microscopy (SEM) was performed with Evo Ma 10 SEM (Carl Zeiss AG, Oberkochen, Germany) with a secondary electron detector at a working distance of 7.5 mm. The acceleration voltage was 25 kV.

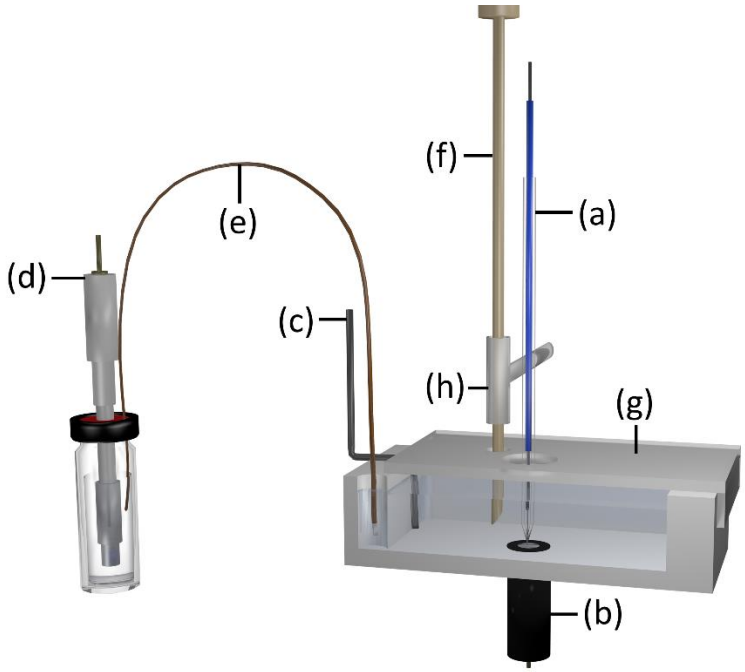

Figure 4.4.1: Schematic representation of the experimental setup. The probe (a), substrate (b) and counter electrode (c) were directly immersed in the solution of the SECM cell. The reference electrode (d) was connected via a fused silica capillary serving as a salt bridge (e). The stirrer (f) was aligned with a mask (g) and guided by a glass tube (h). Copyright © 2018 Elsevier Ltd.

SECM characterization of the BDD electrode

The BDD electrode was characterized by SECM in feedback mode. The image was recorded in quiescent solution with 1.5 mM FcMeOH mediator solution and a 25 µm diameter probe (E_{UME} = 0.5 V) at a tip-to-substrate distance of $d \approx 15$ µm and a scan speed of 125 µm s^{-1} (pixel size: 5 × 5 µm, image resolution: 100 × 100 pixels).

Tip-substrate voltammetry

Prior to experiments involving oxygen and ROS production, the probe was approached to a tip-to-substrate distance of $d \approx 11$ µm using FcMeOH mediator solution. Following the approach, the mediator solution was exchanged with 6 mL of 0.2 M $HClO_4$ after a thorough rinsing of the electrochemical cell with water. For TSV experiments, UMEs with an electrode diameter of 25 µm were used and a quiet time of 5 s was applied. Forced convection was introduced by stirring with a rotation speed of f_{rot} = 25 s^{-1}. To suppress electrical interferences by the stirrer, internal

electrical filters of the instrument were adjusted (signal filter: 1.5 Hz, 2nd I/E filter: 3.2 Hz, 2nd signal filter: 1.5 Hz). For the evaluation of the detection potentials for oxygen and ROS, the substrate electrode was used in the amperometric mode with different fixed potentials ($E_{substrate}$ = 1.6 V, 1.8 V and 2 V). Simultaneously, the potential at the UME was swept between 0 V and 1.6 V with a scan rate of 100 mV s^{-1}. To find suitable potentials for the amperometric ROS generation for the subsequent imaging experiments, the potential at the substrate electrode was swept from 0 V to 2 V for the Pt and from 0 V to 3.2 V for the BDD electrode with a scan rate of 100 mV s^{-1}. The amperometric response at the UME was recorded with E_{UME} = 0.3 V for oxygen and E_{UME} = 1 V for ROS detection.

Imaging of ROS production

For the localization of differences in the ROS production at the BDD surface, several SECM images in feedback and hydrodynamic SG/TC mode were recorded within an area of 300 x 300 µm at the center of a 3 mm BDD disk electrode. Prior to the SECM experiments, the BDD substrate electrode was levelled within a tilt of ≤ 1 µm per 1 mm^2 substrate area. All images were recorded with a 12.5 µm diameter UME at a tip-to-substrate distance of ≈ 3 µm. Imaging in feedback mode was done in quiescent solution with 1.5 mM FcMeOH solution (E_{UME} = 0.5 V, pixel size: 2 × 2 µm, image resolution: 150 × 150 pixels, scan speed: 50 µm s^{-1}). Afterwards, the mediator solution was exchanged as described in the above section. Imaging in the hydrodynamic SG/TC mode (f_{rot} = 25 s^{-1}) during OER was performed with fixed substrate potentials of $E_{substrate}$ = 2.8 V and 3.4 V. The detection at the UME was performed with a fixed potential of E_{UME} = 1 V and the scan speed was 100 µm s^{-1} (pixel size: 4 × 4 µm, image resolution: 75 × 75 pixels).

4.4.3 Results and discussion

ROS formation at Pt

Investigation of O_2 and ROS detection potentials

To investigate the potentials suitable to differentiate between simultaneously produced oxygen and ROS, cyclic voltammetry (CV) at an UME fixed within the diffusion layer of electrochemically produced oxygen was performed. A 2 mm Pt disk electrode was used as substrate electrode. To prevent side reactions of highly reactive ROS with electrolyte species, $HClO_4$ was used as an electrolyte. Forced convection was used to generate a steady-state

diffusion layer in SG/TC experiments as shown previously by our group [46]. The lower part of Fig. 4.4.2 shows the currents measured at the Pt substrate electrode and the upper part shows the corresponding current measured at the UME. As shown by the amperometric current at the substrate electrode, the amount of produced oxygen increased from $E_{substrate}$ = 1.6 V to 2 V. For an increased oxygen evolution at the substrate electrode, a shift of the oxygen reduction potential at the UME towards higher potentials was observed. This showed the effect of a local pH decrease near the substrate electrode with increasing oxygen evolution. A steady-state mass transport for oxygen was recorded at potentials below E_{UME} = 0.3 V in all three cases. This potential was used for the detection of oxygen in further experiments. The observed potential shift for increased oxygen evolution made a potential higher than E_{UME} = 0.9 V necessary to ensure the differentiation between oxygen and ROS. Therefore, a potential of E_{UME} = 1 V was selected for ROS detection.

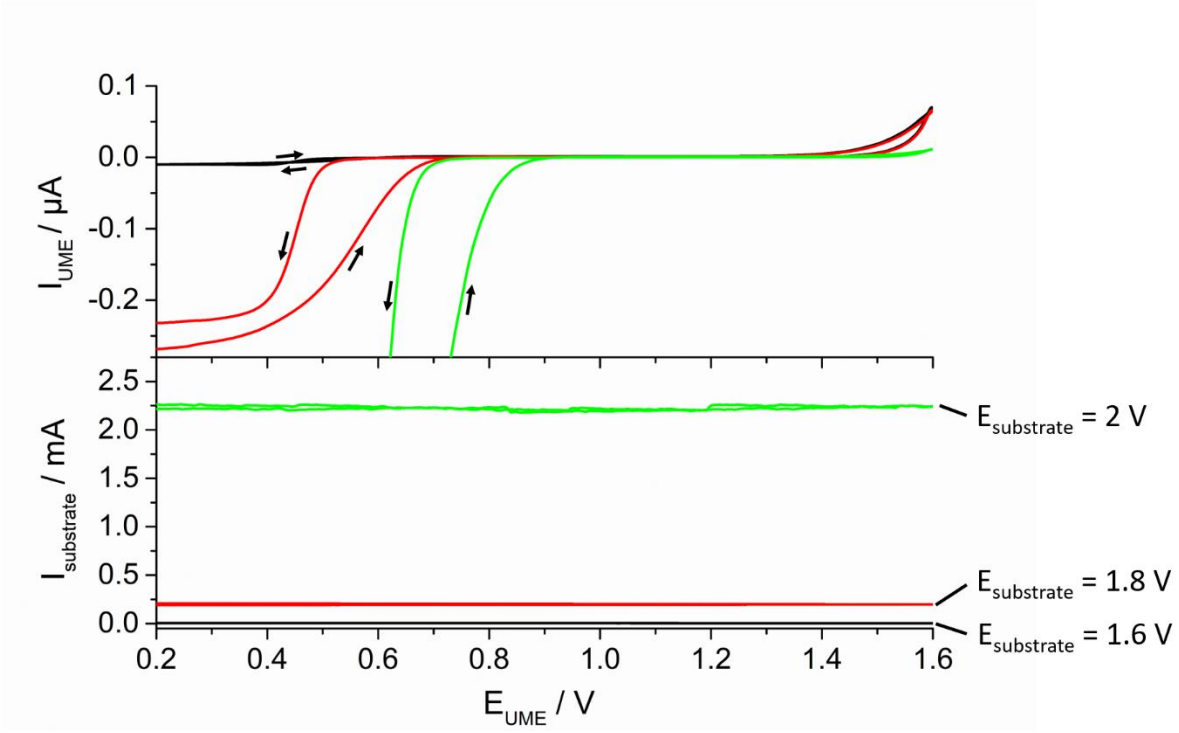

Figure 4.4.2: Amperometric currents at a 2 mm Pt substrate electrode (below) with corresponding CVs (E_{start} = 0.2 V, E_{vertex} = 1.6 V, scan rate: 100 mV s^{-1}) at a 25 µm UME in 0.2 M $HClO_4$ with forced convection (f_{rot} = 25 s^{-1}). The tip-to-substrate distance was ≈ 11 µm.

Investigation of hydrodynamic effects on tip-substrate voltammetry

For the investigation of hydrodynamic effects on the amperometric signal at the UME, the electrode connections for the measurements were switched. CV was performed at the substrate electrode and amperometric detection at the UME fixed near the substrate. This setup in combination with forced convection resulted in an experiment analogous to rotating ring disc electrodes (RRDE). The characterization of hydrodynamic effects was done by UME detection of oxygen produced during CV at the substrate electrode. The lower part of Fig. 4.4.3 shows CVs at the substrate electrode in quiescent solution and with forced convection and the corresponding signals at the UME are shown in the upper part.

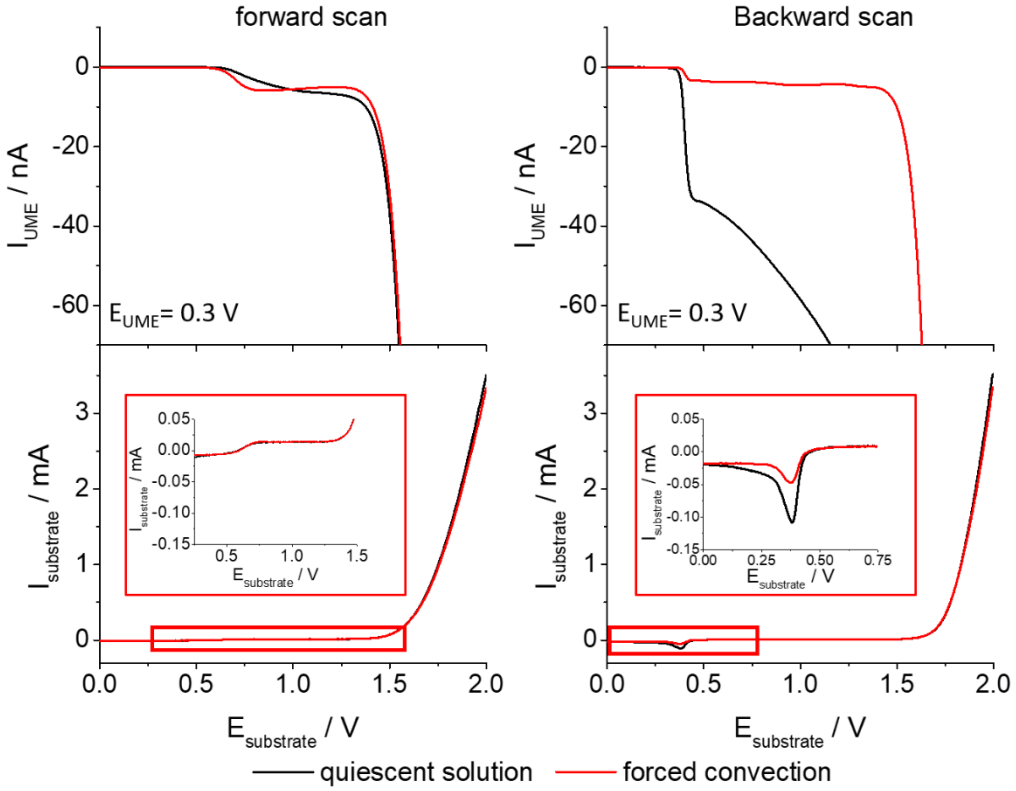

Figure 4.4.3: TSV during a potential sweep at a 2 mm Pt disk electrode (E_{start} = 0 V, E_{vertex} =2 V, scan rate: 100 mV s^{-1}) in 0.2 M $HClO_4$. Red: forced convection (f_{rot} = 25 s^{-1}), black: quiescent solution. The potential of the UME was fixed at E_{UME} = 0.3 V for oxygen detection. The tip-to-substrate distance was ≈ 11 µm. Copyright © 2018 Elsevier Ltd.

A small current was measured during the forward scan at the substrate electrode at potentials between $E_{substrate}$ = 0.6 V and 1.5 V (inset). The oxygen gas formation occurred independently

from the convective environment at potentials higher than $E_{substrate}$ > 1.5 V. The corresponding signal at the UME showed a small current which increased fast into overload during strong oxygen evolution. Forced convection generated a constant current between $E_{substrate}$ = 0.6 V and 1.5 V. During the backward scan, a higher cathodic current was measured at the substrate electrode in quiescent solution (inset). The current at the UME showed a decreasing signal for oxygen in quiescent solution. In contrast, a relatively fast decay of the oxygen signal followed by a constant current showed the effect of forced convection. With forced convection, a stable and uniform mass transport of oxygen towards the UME was achieved. In both cases, oxygen was detected until the competing reduction at the substrate electrode started.

ROS detection at a Pt disk electrode

Since highly reactive oxygen radical species decay very fast in solution producing H_2O_2, the capability of Pt to produce H_2O_2 during OER was studied. In the upper part of Fig. 4.4.4, the amperometric signal at the UME during CV at the substrate is shown.

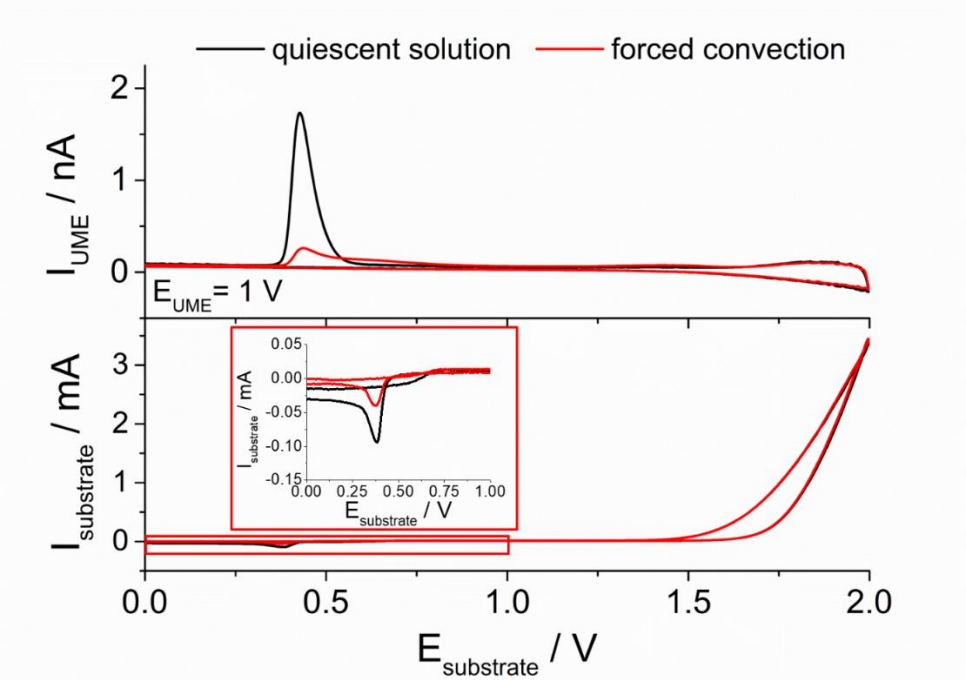

Figure 4.4.4: TSV during a potential sweep at a 2 mm Pt disk electrode (E_{start} = 0 V, E_{vertex} = 2 V, scan rate: 100 mV s^{-1}) in 0.2 M $HClO_4$ (red: forced convection (f_{rot} = 25 s^{-1}), black: quiescent solution). The potential of the UME was fixed at E_{UME} = 1 V for ROS detection. The tip-to-substrate distance was ≈ 11 µm. Copyright © 2018 Elsevier Ltd.

With an applied detection potential of E_{UME} = 1 V, an anodic current, which was attributed to H_2O_2 oxidation was detected. A CV of 5 mM H_2O_2 in $HClO_4$ showed the oxidation of H_2O_2 at this potential. At potentials higher than $E_{substrate}$ = 1.6 V, no difference between the measurements in quiescent solution and with forced convection was visible. In the region of oxygen reduction at the substrate electrode, an anodic signal occurred during the backward scan. H_2O_2 production alongside the oxygen reduction is consistent with reports in the literature [34]. The signal height showed a dependence on the convective situation. Stirring enhanced the transport processes and a smaller signal was measured.

ROS formation at BDD

Characterization of the BDD electrode

To characterize the BDD electrode, several imaging techniques were used. SECM imaging of BDD disk electrode (Fig. 4.4.5A) was done in constant height feedback mode. The minor differences in the feedback current across the surface could not be correlated to surface morphology as the subsequent AFM image (Fig. 4.4.5B) shows a flat topology nearly ideal for feedback imaging in constant height mode. The randomly distributed surface attachments of a few micrometers in length and width and up to 160 nm in height visible in the AFM image are relatively small and are thus invisible to the SECM probe of 25 µm diameter. The SEM image (Fig. 4.4.5C) of the BDD revealed a heterogenic boron distribution across the surface represented as darker (more conductive) and brighter (less conductive) areas of a few tenths of micrometers in size.

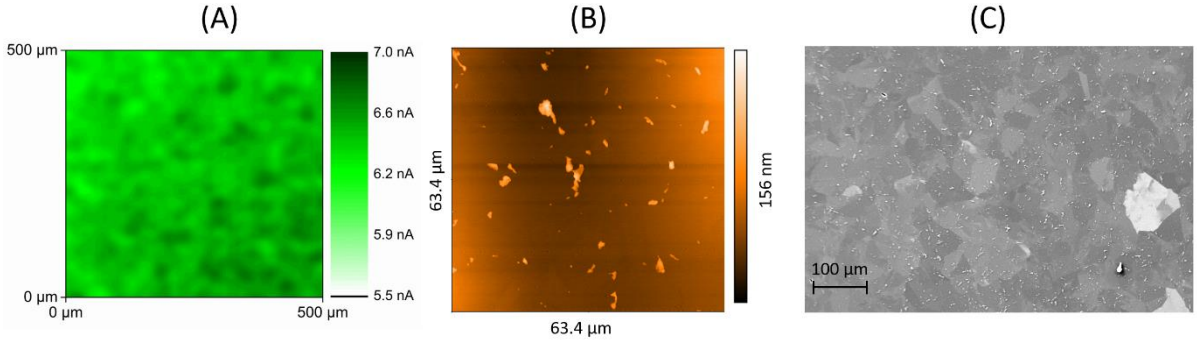

Figure 4.4.5: Surface characterization of the 3 mm BDD disk electrode. (A) SECM image of the BDD electrode in feedback mode in quiescent solution with a Pt probe of 25 µm diameter and a scan speed of 125 µm s^{-1} (E_{UME} = 0.5 V, 1.5 mM FcMeOH in 0.2 M KNO_3, pixel size: 5 × 5 µm, image resolution: 100 × 100 pixels), (B) AFM image and (C) SEM image of the BDD electrode.

A similar observation was made earlier by Neufeld et al. [24]. More recent reports clearly correlated the spatial resolution of electrochemical activity differences with the boron doping level of the electrode [29,30]. However, imaging of exactly the same area segment for a direct comparison of SECM, AFM, and SEM images is a challenging task which was not tackled in the present work. The use of dual AFM/SECM techniques would be an attractive approach for related studies [25].

ROS detection at BDD disk electrode

As an example of an inactive electrode material, a 3 mm BDD disk electrode was used. For the characterization of the OER and the simultaneous ROS production at BDD, similar experiments as with Pt were performed. As expected, Fig. 4.4.6 shows a wider potential range for BDD compared to Pt. The fast combination of ·OH and the kinetically limited H_2O_2 oxidation at BDD [52] led to the production of H_2O_2 detected as anodic current at the UME during the OER.

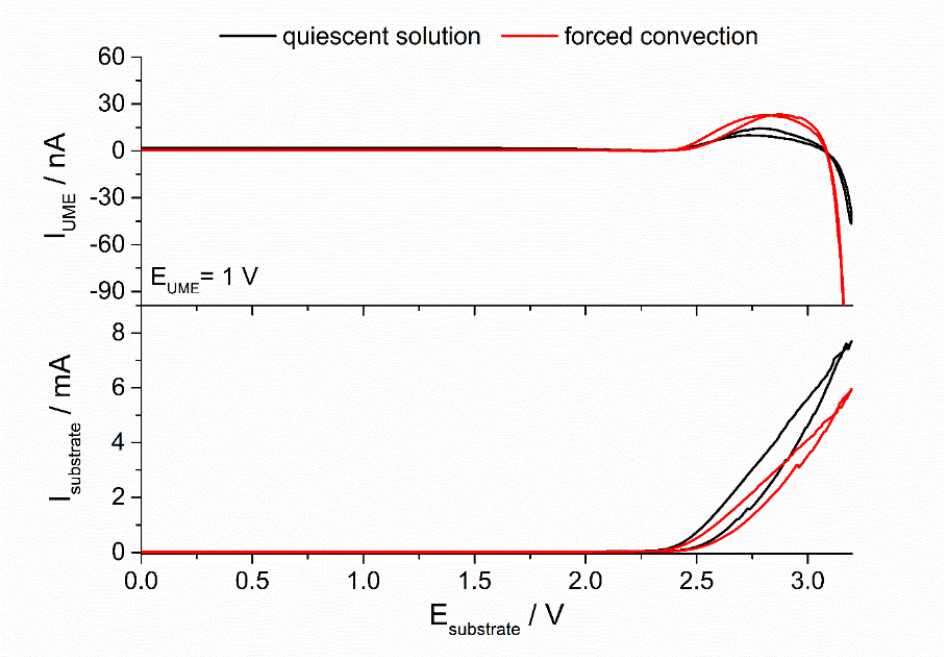

Figure 4.4.6: TSV during a potential sweep at a 3 mm BDD disk electrode (E_{start} = 0 V, E_{vertex} = 3.2 V, scan rate: 100 mV s^{-1}) in 0.2 M $HClO_4$ (red: forced convection (f_{rot} = 25 s^{-1}), black: quiescent solution). The potential of the UME was fixed at E_{UME} = 1 V for ROS detection. The tip-to-substrate distance was ≈ 11 µm. Copyright © 2018 Elsevier Ltd.

The H_2O_2 signal decreased with increasing substrate potential and the followed change from anodic to cathodic current showed the production of another very strong oxidizing species that could be reduced at the UME. With applied forced convection, the species were detected with higher current. O_3 is known to be produced at high overpotentials at BDD electrodes [21,53]. Some studies [54,55] reported the reduction of O_3 at similar potentials as applied in this work. Nevertheless, the occurrence of O_3 could not be proved.

Imaging of ROS production at BDD disk electrode

To investigate the spatial resolution of the ROS production at BDD, different SECM imaging experiments of a 300 x 300 µm area were performed. All enlargements in Fig. 4.4.7 show the same 150 x 150 µm area. The surface was characterized concerning the conductivity using the feedback mode (Fig. 4.4.7A). The evaluation of the H_2O_2 production at a fixed substrate potential of $E_{substrate}$ = 2.8 V (Fig. 4.4.7B) showed significant differences in the surface activity. The correlation with the image of the same area recorded in feedback mode revealed that at domains with small feedback currents considerable amounts of H_2O_2 were produced. Imaging with a higher substrate potential ($E_{substrate}$ = 3.4 V, Fig. 4.4.7C) showed the production of the reducible ROS species predominantly at domains with decreased ·OH evolution. This observation shows that both species are produced simultaneously, but at different areas of the electrode. The size of these areas varied from 100 to several 1000 µm^2 and was in the same range as the darker and brighter domains imaged with SEM. Thus, as pointed out by Patten et al. [29], the ·OH formation can be attributed to less conductive areas with correspondingly lower boron content.

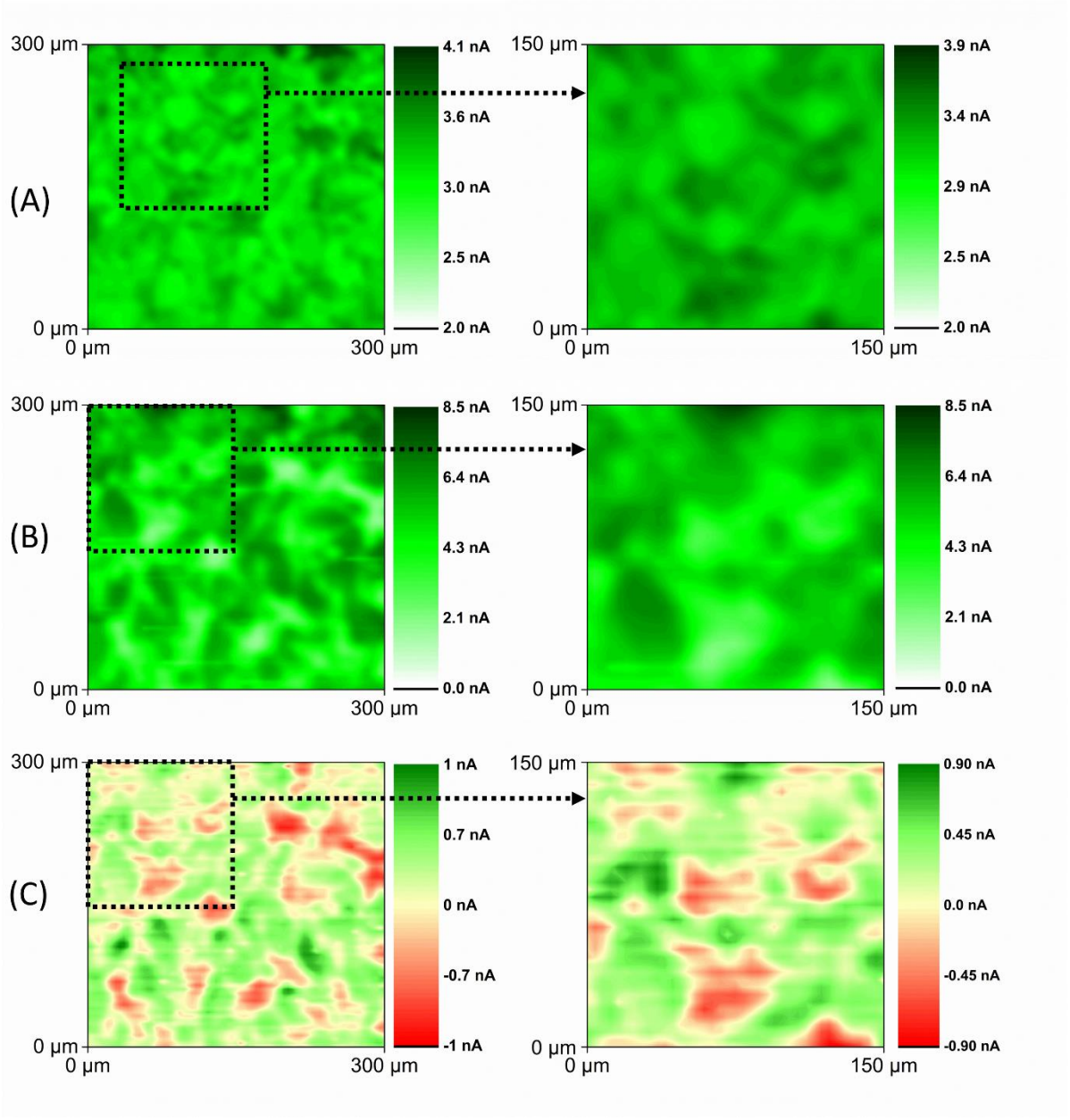

Figure 4.4.7: SECM false-color images of a 300 x 300 µm area of a 3 mm BDD disk electrode. A 12.5 µm diameter UME at a tip-to-substrate distance of 3 µm was used. All enlargements show the same area. (A) Feedback mode in quiescent solution with 1.5 mM FcMeOH in 0.2 M KNO_3 (E_{UME} = 0.5 V) and a scan speed of 50 µm s^{-1} (pixel size: 2 × 2 µm, image resolution: 150 × 150 pixels). (B) and (C) SECM images in hydrodynamic SG/TC mode (f_{rot} = 25 s^{-1}) during amperometric OER in 0.2 M $HClO_4$ with $E_{substrate}$ = 2.8 V (B) and $E_{substrate}$ = 3.4 V (C). UME potential was fixed at E_{UME} = 1 V and the scan speed was 100 µm s^{-1} (pixel size: 4 × 4 µm, image resolution: 75 × 75 pixels). Anodic currents are illustrated in green and cathodic currents in red.

4.4.4 Conclusions

The work presented here showed that the combination of SECM with forced convection increases the capability and the applicability of the SECM for material characterization and surface analysis during gas evolution at the investigated surface. Tip-substrate voltammetry in combination with forced convection gained similar information as with RRDE. The exploitation of the hydrodynamic effect forming a steady-state diffusion layer resulted in additional knowledge of the special localization of in situ produced electrochemically active species. The characterization of ROS production at BDD showed the production of H_2O_2 and a reducible ROS species. Imaging in hydrodynamic SG/TC mode revealed a local production of both species simultaneously at different domains. The possibility to localize and image reactive species at macroscopic electrodes is a great advantage of hydrodynamic SECM and increases the accessible analytical information for a better understanding of electrochemical processes. The methods described in this work can pave the way for extended studies of important OER catalysts used in various applications.

References

[1] M.P. Murphy, How mitochondria produce reactive oxygen species, Biochem. J. 417 (2009) 1–13.

[2] H. Tsukagoshi, W. Busch, P.N. Benfey, Transcriptional regulation of ROS controls transition from proliferation to differentiation in the root, Cell 143 (2010) 606–616.

[3] F. Randow, J.D. MacMicking, L.C. James, Cellular self-defense: How cell-autonomous immunity protects against pathogens, Science 340 (2013) 701–706.

[4] H.J. Forman, M. Torres, Reactive oxygen species and cell signaling, Am. J. Respir. Crit. Care Med. 166 (2002) S4–S8.

[5] R. Mittler, S. Vanderauwera, N. Suzuki, G. Miller, V.B. Tognetti, K. Vandepoele, M. Gollery, V. Shulaev, F. Van Breusegem, ROS signaling: The new wave?, Trends Plant Sci. 16 (2011) 300–309.

[6] C. Fleury, B. Mignotte, J. Vayssière, Mitochondrial reactive oxygen species in cell death signaling, Biochimie 84 (2002) 131–141.

[7] G. Xu, M.R. Chance, Hydroxyl radical-mediated modification of proteins as probes for structural proteomics, Chem. Rev. 107 (2007) 3514–3543.

[8] H.J.H. Fenton, LXXIII.—Oxidation Of tartaric acid in presence of iron, J. Chem. Soc. Trans. 65 (1894) 899–910.

[9] K. Barbusiński, Fenton reaction - Controversy concerning the chemistry, Ecol. Chem. Eng. S 16 (2009) 347–358.

[10] J.J. Pignatello, E. Oliveros, A. MacKay, Advanced oxidation processes for organic contaminant destruction based on the fenton reaction and related chemistry, Crit. Rev. Environ. Sci. Technol. 36 (2006) 1–84.

[11] B.P. Chaplin, Critical review of electrochemical advanced oxidation processes for water

treatment applications, Environ. Sci. Process. Impacts 16 (2014) 1182–1203.
[12] I. Sirés, P.L. Cabot, F. Centellas, J.A. Garrido, R.M. Rodríguez, C. Arias, E. Brillas, Electrochemical degradation of clofibric acid in water by anodic oxidation. Comparative study with platinum and boron-doped diamond electrodes, Electrochim. Acta 52 (2006) 75–85.
[13] M. Panizza, G. Cerisola, Direct and mediated anodic oxidation of organic pollutants, Chem. Rev. 109 (2009) 6541–6569.
[14] C.A. Martínez-Huitle, E. Brillas, Decontamination of wastewaters containing synthetic organic dyes by electrochemical methods: A general review, Appl. Catal. B Environ. 87 (2009) 105–145.
[15] I. Sirés, E. Brillas, M.A. Oturan, M.A. Rodrigo, M. Panizza, Electrochemical advanced oxidation processes: Today and tomorrow. A review, Environ. Sci. Pollut. Res. 21 (2014) 8336–8367.
[16] D.B. Miklos, C. Remy, M. Jekel, K.G. Linden, J.E. Drewes, U. Hübner, Evaluation of advanced oxidation processes for water and wastewater treatment – A critical review, Water Res. 139 (2018) 118–131.
[17] G.V. Buxton, C.L. Greenstock, W.P. Helman, A.B. Ross, Critical review of rate constants for reactions of hydrated electrons, hydrogen atoms and hydroxyl radicals in aqueous solution, J. Phys. Chem. Ref. Data 17 (1988) 513–886.
[18] D.T. Sawyer, J.S. Valentine, How super is superoxide?, Acc. Chem. Res. 14 (1981) 393–400.
[19] D. Wabner, C. Grambow, Reactive intermediate during oxidation of water at lead dioxide and platinum electrodes, Reactions 195 (1985) 95–108.
[20] T.A. Ivandini, Y. Einaga, Polycrystalline boron-doped diamond electrodes for electrocatalytic and electrosynthetic applications, Chem. Commun. 53 (2017) 1338–1347.
[21] P.A. Michaud, M. Panizza, L. Ouattara, T. Diaco, G. Foti, C. Comninellis, Electrochemical oxidation of water on synthetic boron-doped diamond thin film anodes, J. Appl. Electrochem. 33 (2003) 151–154.
[22] B. Marselli, J. Garcia-Gomez, P.-A. Michaud, M.A. Rodrigo, C. Comninellis, Electrogeneration of hydroxyl radicals on boron-doped diamond electrodes, J. Electrochem. Soc. 150 (2003) D79–D83.
[23] K.B. Holt, A.J. Bard, Y. Show, G.M. Swain, Scanning electrochemical microscopy and conductive probe atomic force microscopy studies of hydrogen-terminated boron-doped diamond electrodes with different doping levels, J. Phys. Chem. B 108 (2004) 15117–15127.
[24] A.K. Neufeld, A.P. O'Mullane, Effect of the mediator in feedback mode-based SECM interrogation of indium tin-oxide and boron-doped diamond electrodes, J. Solid State Electrochem. 10 (2006) 808–816.
[25] N.R. Wilson, S.L. Clewes, M.E. Newton, P.R. Unwin, J.V. Macpherson, Impact of grain-dependent boron uptake on the electrochemical and electrical properties of polycrystalline boron-doped diamond electrodes, J. Phys. Chem. B 110 (2006) 5639–5646.
[26] N. Yang, J.S. Foord, X. Jiang, Diamond electrochemistry at the nanoscale: A review, Carbon 99 (2016) 90–110.
[27] Y. Einaga, J.S. Foord, G.M. Swain, Diamond electrodes: Diversity and maturity, MRS Bulletin 39 (2014) 525–532.
[28] J.H.T. Luong, K.B. Male, J.D. Glennon, Boron-doped diamond electrode: Synthesis,

characterization, functionalization and analytical applications, Analyst 134 (2009) 1965–1979.
[29] H.V. Patten, S.C.S. Lai, J.V. MacPherson, P.R. Unwin, Active sites for outer-sphere, inner-sphere, and complex multistage electrochemical reactions at polycrystalline boron-doped diamond electrodes (pBDD) revealed with scanning electrochemical cell microscopy (SECCM), Anal. Chem. 84 (2012) 5427–5432.
[30] H.V. Patten, K.E. Meadows, L.A. Hutton, J.G. Iacobini, D. Battistel, K. McKelvey, A.W. Colburn, M.E. Newton, J.V. MacPherson, P.R. Unwin, Electrochemical mapping reveals direct correlation between heterogeneous electron-transfer kinetics and local density of states in diamond electrodes, Angew. Chem. Int. Ed. 51 (2012) 7002–7006.
[31] A.A. Dalle, L. Domergue, F. Fourcade, A.A. Assadi, H. Djelal, T. Lendormi, I. Soutrel, S. Taha, A. Amrane, Efficiency of DMSO as hydroxyl radical probe in an electrochemical advanced oxidation process − Reactive oxygen species monitoring and impact of the current density, Electrochim. Acta 246 (2017) 1–8.
[32] A. Hájková, J. Barek, V. Vyskočil, Electrochemical DNA biosensor for detection of DNA damage induced by hydroxyl radicals, Bioelectrochemistry 116 (2017) 1–9.
[33] E. Finkelstein, G.M. Rosen, E.J. Rauckman, Spin trapping of superoxide and hydroxyl radical: Practical aspects, Arch. Biochem. Biophys. 200 (1980) 1–16.
[34] N.M. Marković, T.J. Schmidt, V. Stamenković, P.N. Ross, Oxygen reduction reaction on Pt and Pt bimetallic surfaces: A selective review, Fuel Cells 1 (2001) 105–116.
[35] J. Kwak, A.J. Bard, Scanning electrochemical microscopy. Apparatus and two-dimensional scans of conductive and insulating substrates, Anal. Chem. 61 (1989) 1794–1799.
[36] D. Polcari, P. Dauphin-Ducharme, J. Mauzeroll, Scanning electrochemical microscopy: A comprehensive review of experimental parameters from 1989 to 2015, Chem. Rev. 116 (2016) 13234–13278.
[37] J.-M. Noël, Y. Yu, M.V. Mirkin, Dissolution of Pt at moderately negative potentials during oxygen reduction in water and organic media, Langmuir 29 (2013) 1346–1350.
[38] S.J. Percival, J.E. Dick, A.J. Bard, Cathodically dissolved platinum resulting from the O_2 and H_2O_2 reduction reactions on platinum ultramicroelectrodes, Anal. Chem. 89 (2017) 3087–3092.
[39] X. Zhao, P.M. Diakowski, Z. Ding, Deconvoluting topography and spatial physiological activity of live macrophage cells by scanning electrochemical microscopy in constant-distance mode, Anal. Chem. 82 (2010) 8371–8373.
[40] C. Amatore, S. Arbault, C. Bouton, K. Coffi, J.C. Drapier, H. Ghandour, Y. Tong, Monitoring in real time with a microelectrode the release of reactive oxygen and nitrogen species by a single macrophage stimulated by its membrane mechanical depolarization, ChemBioChem. 7 (2006) 653–661.
[41] J. Rodríguez-López, M.A. Alpuche-Avilés, A.J. Bard, Interrogation of surfaces for the quantification of adsorbed species on electrodes: Oxygen on gold and platinum in neutral media, J. Am. Chem. Soc. 130 (2008) 16985–16995.
[42] H.S. Park, K.C. Leonard, A.J. Bard, Surface interrogation scanning electrochemical microscopy (SI-SECM) of photoelectrochemistry at a W/Mo-$BiVO_4$ semiconductor electrode: Quantification of hydroxyl radicals during water oxidation, J. Phys. Chem. C 117 (2013) 12093–12102.
[43] D. Zigah, J. Rodríguez-López, A.J. Bard, Quantification of photoelectrogenerated hydroxyl radical on TiO_2 by surface interrogation scanning electrochemical microscopy, Phys. Chem. Chem. Phys. 14 (2012) 12764-12772.

[44] D. Khamis, E. Mahé, F. Dardoize, D. Devilliers, Peroxodisulfate generation on boron-doped diamond microelectrodes array and detection by scanning electrochemical microscopy, J. Appl. Electrochem. 40 (2010) 1829–1838.
[45] J. Kwak, A.J. Bard, Scanning electrochemical microscopy. Theory of the feedback mode, Anal. Chem. 61 (1989) 1221–1227.
[46] R.D. Martin, P.R. Unwin, Theory and experiment for the substrate generation tip collection mode of the scanning electrochemical microscope: Application as an approach for measuring the diffusion coefficient ratio of a redox couple, Anal. Chem. 70 (1998) 276–284.
[47] C.G. Zoski, C.R. Luman, J.L. Fernández, A.J. Bard, Scanning electrochemical microscopy. 57. SECM tip voltammetry at different substrate potentials under quasi-steady-state and steady-state conditions, Anal. Chem. 79 (2007) 4957–4966.
[48] J. Kang, Y. Yang, F. Jiang, H. Shao, Study on the anodic reaction of Ni in an alkaline solution by transient pH detection based on scanning electrochemical microscopy (SECM), Surf. Interface Anal. 39 (2007) 877–884.
[49] C. Iffelsberger, P. Vatsyayan, F.-M. Matysik, Scanning electrochemical microscopy with forced convection introduced by high-precision stirring, Anal. Chem. 89 (2017) 1658–1664.
[50] P. Vatsyayan, C. Iffelsberger, C.C. Mayorga, F.-M. Matysik, Imaging of localized enzymatic peroxidise activity over individual unbiased gold nanowires by scanning electrochemical microscopy, Anal. Methods 8 (2016) 6847–6855.
[51] Y. Shao, M.V. Mirkin, Probing ion transfer at the liquid/liquid interface by scanning electrochemical microscopy (SECM), J. Phys. Chem. B 102 (1998) 9915–9921.
[52] I. Kisacik, A. Stefanova, S. Ernst, H. Baltruschat, Oxidation of carbon monoxide, hydrogen peroxide and water at a boron-doped diamond electrode: The competition for hydroxyl radicals, Phys. Chem. Chem. Phys. 15 (2013) 4616–4624.
[53] L.M. Da Silva, M.H.P. Santana, J.F.C. Boodts, Electrochemistry and green chemical processes: Electrochemical ozone production, Quim. Nova 26 (2003) 880–888.
[54] C. Fabjan, Die kathodische Reduktion von Ozon in sauren Elektrolyten, Electrochim. Acta 20 (1975) 863–870.
[55] C. Fabjan, A study of the cathodic reduction of ozone at the rotating disc electrode in acid electrolyte, J. Electroanal. Chem. 76 (1977) 91–99.

4.5 Imaging of localized enzymatic peroxidase activity over unbiased individual gold nanowires by scanning electrochemical microscopy

Preety Vatsyayan, Christian Iffelsberger, Carmen C. Mayorga-Martinez and Frank-Michael Matysik,

Analytical Methods 8 (2016) 6847–6855

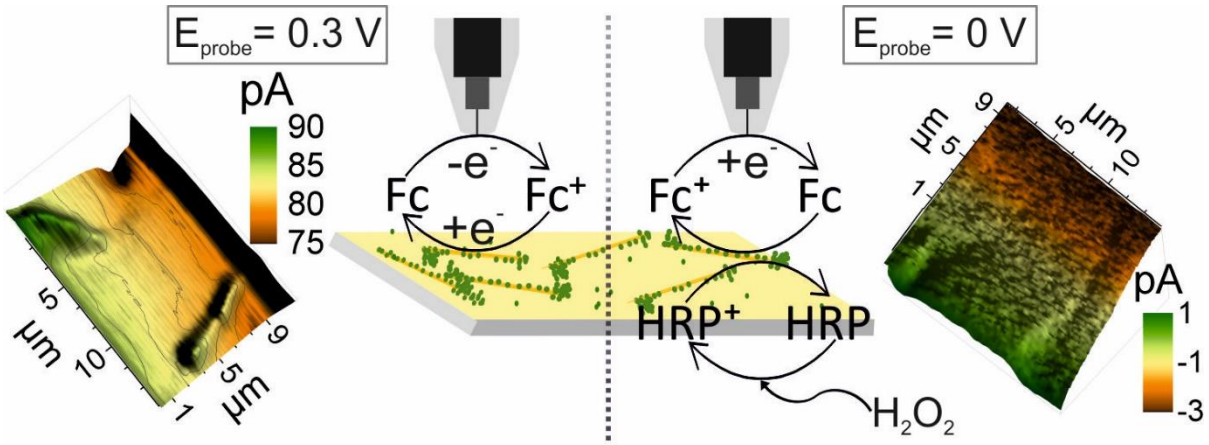

Published by the Royal Society of Chemistry

Abstract

Scanning electrochemical microscopy (SECM) in constant-height mode was used to image individual gold nanowires (AuNWs, 2-3 µm long and ~140 nm diameter). High-resolution negative and positive feedback current images of individual AuNWs immobilized on glass and gold-coated glass slides, respectively were recorded with a Wollaston-based platinum disk ultramicroelectrode (UME) of radius 300 nm at 0.3 V probe potential using ferrocene methanol as mediator. The negative and positive feedback current responses were dependent on the effective recycling of mediator on the unbiased AuNWs.

4.5.1 Introduction

Scanning electrochemical microscopy (SECM) is known to be a powerful tool for the investigation and imaging of topography and surface reactivity of microstructured substrates [1,2]. It is a non-contact scanning probe imaging technique that has evolved from a low resolution electrochemical imaging system after its introduction by Bard et al. in 1989, to a high resolution topographic imaging technique in recent years [3,4]. Recently, SECM has been used for imaging both living and non-living substrates with nanoscale resolution. However, the imaging at nanoscale is largely dependent on the size of the probes. Lately, with the development of methods for fabrication of sub-micrometer and nanometer sized probes for SECM, the high-resolution topographic imaging has frequently been possible. The fabrication of SECM probes by pulling annealed Pt wires in capillaries through a laser puller enables the fabrication of probes with diameters as small as 50 nm with very small RG values (ratio of glass sheath radius and probe electrode radius). Such probes can be used to image living cells and non-living substrates with lateral resolutions as high as 100-200 nm [5,6]. However, frequent use of such nanoprobes is still limited for many applications because of the difficulty in their handling and operation.

Besides providing topographic details, a very interesting aspect of SECM is the ability to study surface reactivity. This feature gives SECM an advantage over other microscopic techniques such as atomic force microscopy (AFM), scanning and transmission electron microscopy (SEM and TEM) etc. which cannot provide information about the chemical reactivity of the surface. Thus, SECM has potential applications in biosensors research to study localized enzymatic activity over transducer surfaces independent of transducer itself. It also allows imaging of relative positions of active spots of immobilized enzymes. Furthermore, SECM is also efficiently used for imaging of enzymatic activity over protein-tagged DNA or protein microarrays or chips. Although, SECM has been used as a tool in biosensor studies since long [7], most of the works with SECM imaging in biosensing studies were limited to rather large enzyme spots with microscale resolution.

Lately, there has been a tremendous increase in the use of nanomaterials for bioelectrochemical applications for developing new nanoscale sensing devices for future biological, medical, and electronic applications [8–10]. The reasons for such increase are high surface to volume ratio provided by nanomaterials over the transducer surface (that results in higher sensitivity and lower detection limit), their fast electron transfer efficiency and their specific electronic and

optical properties. Among nanomaterials, nanotubes and nanowires are extensively used materials for sensor applications [11–13]. They are also termed as one dimensional (1-D) nanostructures because of a high ratio of their length (μm) to their diameter (nm). Gold nanowires (AuNWs) are fast gaining ground in sensing applications due to their high chemical and thermal stability, biocompatibility and excellent electrical conductivity [14–24]. Their ease of self-assembly over thiol modified transducer surfaces provides a stable matrix for electrochemical studies and/or for biomolecule assembly via chemical cross-linking. The recent trend towards miniaturization of sensing devices encourages the use of single AuNW for electrochemical studies [25,26]. Thus, it would be interesting to carry out SECM studies of individual AuNW and to utilize its potential to map enzymatic activity distribution over it. Some of the recent publications have already established the role of SECM in imaging and characterization of the electrochemical activity of individual nanomaterials [27–29]. Unwin and coworkers have extensively used scanning electrochemical cell microscopy (SECCM) to study individual biased single walled carbon nanotube and its catalytic activity [30,31]. However, SECCM is not yet explored for electrochemical studies of unbiased individual nanomaterials. Besides, the immobilization and imaging of redox proteins over individual nanomaterial are not reported so far. The classical constant height mode of SECM can be reliably used to image individual nanomaterials topographically and to study redox (enzymatic) activity over them. The distribution and stability of enzymatic activity (after immobilization) over individual nanostructure can also be visualized via this technique.

In this work, we used SECM to image individual AuNWs over glass and gold-coated glass slides with high resolution using Wollaston-based Pt nanoprobes. The work was further extended by imaging the enzymatic peroxidase activity over individual AuNWs using ferrocene methanol as the mediator system. The enzyme horseradish peroxidase (HRP) was used as the model enzyme for peroxidase activity imaging as in addition to having an extensive biosensor potential, it is a commonly used tagging enzyme (enzyme label) for antibody or ligand molecules for molecular recognition or signal amplification in immunoassays, protein microarrays and SECM imaging studies [17,23,32–34].

4.5.2. Materials and Methods

Reagents

For all the SECM experiments, an aqueous solution of 1.5 mM ferrocene methanol (99 %, ABCR, Karlsruhe, Germany) containing 0.25 M KNO_3 as supporting electrolyte was used as the mediator solution. The reagents (3-mercaptopropyl)triethoxysilane (MPTES), 1,4-butanedithiol, 11 mercaptoundecanoic acid, N-hydroxysuccinimide (NHS) were from Aldrich, Steinheim, Germany. N-(3-Dimethylaminopropyl)-N'-ethylcarbodimide hydrochloride (EDC) was obtained from Fluka, Steinheim, Germany. The enzyme horseradish peroxidase (HRP) was obtained from Serva GMBH, Germany. All other chemicals were of analytical reagent grade. The solutions were prepared in ultrapure water with a resistivity greater than 18 MΩ cm (membraPure, Bodenheim, Germany).

Synthesis of gold nanowires and their immobilization on substrates

Gold nanowires (AuNWs) were synthesized by electrodeposition of gold in a polycarbonate membrane template by modification of the procedure described by Mayorga-Martinez et al. [24]. Prior to AuNWs synthesis, an ultrathin gold-film was first sputtered on one side of the 0.1 µm isopore polycarbonate membrane (Merck Millipore) by using a conventional ion sputtering method to make the template conductive to be used as the working electrode. The membrane was then assembled in a plating cell by using an aluminum foil as contact. An Ag/AgCl electrode (CH Instruments, Austin, USA) and a 0.3 mm diameter platinum wire were used as reference and counter electrodes, respectively. Gold was electrodeposited at -0.9 V for 60 s from a commercial plating solution (AMI DODUCO, Spain). After electroplating, the sputtered gold layer was removed mechanically with a 3–4 µm alumina slurry. To release the nanowire from the polycarbonate template, the membrane was dissolved by immersing it in methylene chloride solution for 10 min. Finally, the solution was centrifuged at 6000 rpm for 2 min to pellet the nanowires. The pellet was then washed repeatedly with methylene chloride and ethanol with intermittent centrifugation and dissolution. The synthesized AuNWs were then inspected by TEM (JEOL Ltd., Japan).

AuNWs were immobilized on thiol-modified glass and gold-coated glass slides. The microscopic glass slide was cleaned overnight in concentrated nitric acid. The cleaned glass slide was rinsed with water followed by drying with nitrogen gas and kept at 110 °C in oven for 1 h. The oven dried slide was immediately immersed in a 5 % solution of MPTES in

anhydrous toluene for 30 min. After rinsing the thiosilane-modified glass slide with toluene and acetone several times, it was then dried at 110 °C in oven for 1 h prior to use. The gold-coated glass slide (commercial surface plasmon resonance slide with 50 nm thin film of gold) was thoroughly cleaned with ethanol and dried with nitrogen gas. A 10 mM ethanolic solution of 1,4 butanedithiol was drop-coated on the slide and left overnight. The dithiol modified slide was rinsed thoroughly with water before use.

An ethanolic solution of AuNWs was drop-coated on thiol-modified glass and gold-coated glass slides and left for ~6 h. The slides with immobilized AuNWs were rinsed thoroughly with water prior to SECM imaging to remove any unbound AuNWs. AuNWs were imaged electrochemically in constant height mode at 0.3 V probe potential in ferrocene methanol mediator solution.

Covalent-linking of HRP with AuNWs was achieved by partial modification of the procedure described by Saxena et al. [35]. Briefly, 0.5 mM freshly prepared ethanolic solution of 11 mercaptoundecanoic acid was added to AuNWs in an Eppendorf cup and left for 5 h to obtain carboxylic group functionalized AuNWs. The solution was then centrifuged at 10,000 ×g for 5 min to pellet AuNWs. The pellet was then washed with ethanol to remove unbound 11-mercaptoundecanoic acid. The carboxyl functionalized AuNWs were then treated with a solution of EDC (10 mg ml^{-1}) and NHS (50 mg ml^{-1}) for 10 min to activate the carboxylic group on the AuNWs. Freshly prepared HRP solution (10 mg ml^{-1}) in sodium phosphate buffer (SPB, 50 mM, pH 6) was added to that and kept at 4 °C for 12 h to obtain HRP-linked AuNWs. The HRP-linked AuNWs were then immobilized on the thiol modified gold-coated glass slide for subsequent feedback and peroxidase activity imaging by SECM. The localized HRP activity on AuNWs was imaged in constant height mode by adding 0.3 % H_2O_2 to the ferrocene methanol solution and applying a probe potential of 0 V. The ferrocene methanol solution for activity imaging was prepared in SPB.

Electrochemical and AFM instrumentation

A commercial SECM system CHI 920c (CH Instruments, Austin, USA) was used for all experiments. It consisted of a bipotentiostat and a motor control unit that controls both the stepper motor and the piezo positioner. A tailor-made electrochemical cell (Teflon) with two clamps (PEEK) and four integrated screws (Teflon) for substrate fixation was used. The electrochemical cell was bolted on a stainless-steel carrier that was levelled using three

micrometer adjustment screws. A Pt electrode was used both as reference and counter electrodes throughout the SECM experiments. All the potentials mentioned in this paper refer to this quasi-reference electrode.

AFM imaging of all the AuNWs modified substrates was performed with a commercial system Nanosurf easyScan 2 (Nanoscience Instruments, Phoenix, USA) and AFM probes PPP-NCLR (Nanoscience Instruments, Phoenix, USA) in the tapping mode.

4.5.3 Results and discussion

Feedback Imaging of AuNWs

The characterization of synthesized AuNWs with TEM showed that the average AuNWs were 2-3 µm long and ~140 nm in diameter (Fig. 4.5.S1, supporting information). Later, an approach for immobilization of AuNWs on a thiosilane-modified glass slide was developed. The nanowires immobilized on the glass substrate were stable for frequent SECM scans in mediator solution. The AuNWs on glass slides did not show positive feedback current response by mediator recycling despite being a conductor. Instead, negative topographic images were recorded for individual AuNWs by a 300 nm radius probe within 70-80 % I_∞ (Fig. 4.5.1A). Figure 4.5.1B shows a representative AFM image of immobilized AuNWs on glass slide. The negative feedback image of individual AuNWs immobilized on an insulating glass surface was intriguing and the reason could be attributed to their inability to act as efficient bipolar substrates (enabling an anodic reaction at some distance from the cathodic mediator regeneration at the unbiased AuNWs in the probe vicinity). Normally, when a conducting substrate has a smaller area compared to that of the probe, positive feedback is significantly limited by the substrate's ability to act as an efficient bipolar electrode and the substrate could get charged with time. However, in one of the recent reports by Oleinick et al. [36] it has been shown experimentally that if the substrate extends beyond the area covered by the tip, the constraints due to the bipolar function become negligible because the extended parts of the conductor may act as an efficient second pole of the bipolar substrate exchanging electrons with the bulk solution. In our experiment, the diameter of the AuNW (~140 nm) was significantly smaller than the Pt probe diameter (600 nm). However, the relatively extended length of the nanowire (2-3 µm) was still not sufficient for effective recycling of the electrons with the bulk mediator solution resulting in negative feedback current response. Previously, Amemiya and co-workers [27,28] were able to record positive feedback images of lithographically casted gold

nanoband (100 nm broad and 50 µm long) and single walled carbon nanotube (~1.6 nm diameter and ~2 mm long) on insulating surfaces with probes of diameters ~2 µm and 10 µm, respectively. Although, the diameters of probes used to record these images were rather large compared to the one used in our studies with AuNWs, the extreme extended lengths of these bands and nanowires were sufficient to exchange electrons with the bulk solution and to behave as bipolar substrates. Thus, a certain minimum ratio of length of the nanowire to the Pt tip diameter was necessary to have an effective second pole, which could exchange electrons with the bulk solution and facilitate positive feedback response from the unbiased AuNWs. Additionally, a significantly larger *RG* (between ~15-30) of the 300 nm radius probe could also have had a shielding effect for the flow of bulk mediator solution towards the far ends of individual AuNWs below the tip, hindering the exchange of electrons from them. A similar effect of *RG* was observed by Xiong et al. [37] where the positive feedback from an unbiased conducting substrate was found to depend on the thickness of the insulating layer surrounding the metal disk probe of comparable radius, which hindered mediator diffusion from the bulk solution to the substrate.

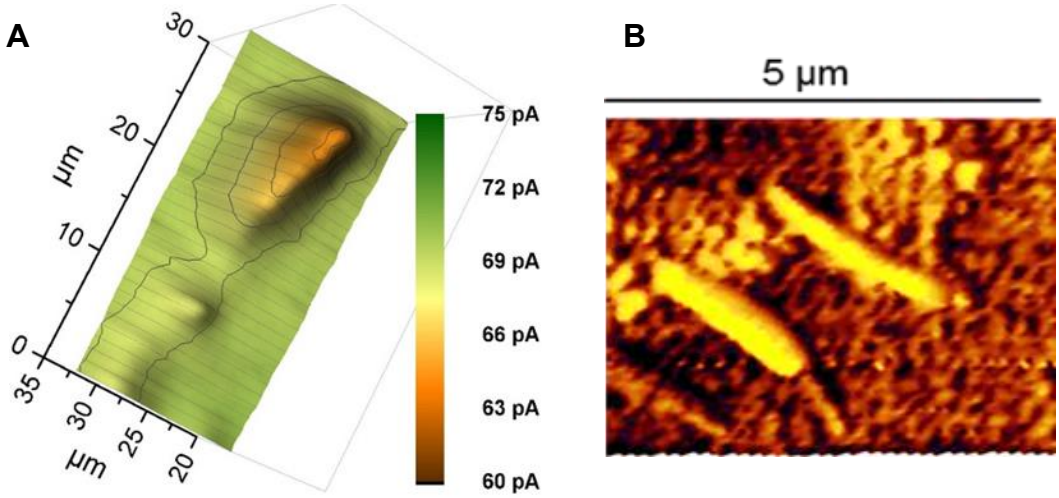

Figure 4.5.1: (A) Negative feedback SECM image of individual AuNWs immobilized on a glass slide. The image was recorded with a 300 nm radius Pt probe at a potential of 0.3 V and a scan rate of 5 µm s^{-1} in 1.5 mM ferrocene methanol solution. (B) Representative AFM image of AuNWs immobilized on a glass slide. Published by the Royal Society of Chemistry.

However, they also showed that the current approach curves changed from negative to positive as *RG* was changed from 50 to 1.1. Although, the length of 1-D nanostructures compared to the probe diameters (including *RG*) is well known to have an effect on the feedback response (negative or positive) from the unbiased conducting substrates [27,37], a clear negative feedback current image of an individual unbiased conducting nanowire immobilized over an insulating substrate has not been reported before.

To further investigate the above observation, AuNWs were immobilized on glass slide coated with thin-film of gold. A well-dispersed assembly of AuNWs over thiol-modified gold-coated glass slide was achieved as seen in the representative AFM images (Fig. 4.5.2C and D). The AuNWs immobilized on a gold coated slide were stable enough to be scanned frequently by SECM probes. Positive feedback approach curves over an entire thiol-modified gold surface were recorded which showed that thiol-modification did not interfere with the recycling of mediator over the bulk gold surface. Well-resolved positive feedback images of both clustered as well as individual AuNWs were recorded with a 300 nm radius probe within 105-110 % I_∞ over conducting gold surface (Fig. 4.5.2A and B). The extended conducting surface (thin conducting gold film in this case) beyond the tip area facilitated the recycling of electrons of nanowires with the bulk mediator solution resulting in positive feedback response. The visibly differentiated contrast of AuNWs over a bulk gold surface was the result of the differences in topography (effectively exposed surface area for recycling of mediator) and in intrinsic conductivity of AuNWs and thin-film gold surface. However, the positive feedback on the AuNWs supported the fact that the immobilized AuNWs were effectively electrically connected with the bulk gold surface. This result supports the fact that SECM can be used as a method of choice for characterization of immobilization of nanomaterials as support matrix for biomolecule assembly over transducer surfaces in addition to other physical and electrochemical methods.

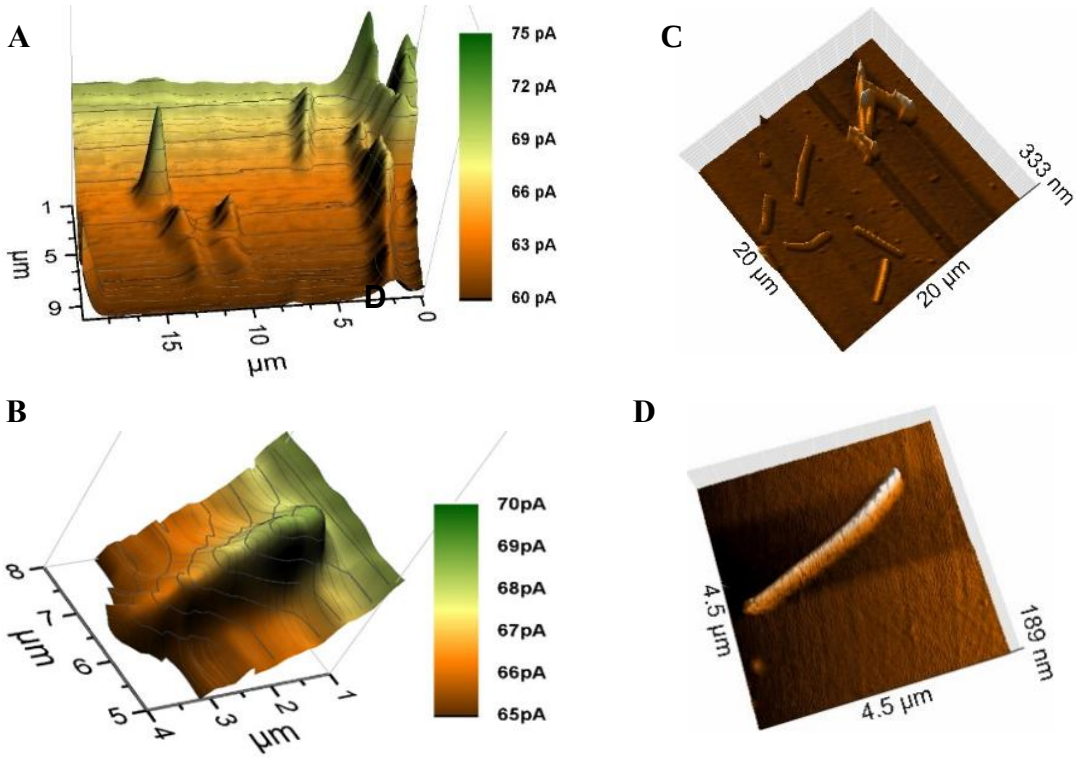

Figure 4.5.2: (A and B) Positive feedback SECM images of clustered and individual AuNWs immobilized on a gold-coated glass slide. The image was recorded with a 300 nm radius Pt probe at a potential of 0.3 V and a scan rate of 5 μm s^{-1} in 1.5 mM ferrocene methanol solution. (C and D) Representative AFM images of AuNWs immobilized on a gold-coated glass slide. Published by the Royal Society of Chemistry.

An apparent width of ~10 μm with ~5 pA of negative feedback current was recorded for individual AuNWs immobilized on a glass slide (Fig. 4.5.3A). On the other hand, an apparent width of ~1.5-2 μm with ~2 pA positive feedback current was recorded for individual AuNWs immobilized on a gold-coated glass slide (Fig. 4.5.3B). The apparent width of the nanowire in negative feedback image was largely affected by the big *RG* of the probe, whereas in positive feedback image over bulk gold substrate, it was almost independent of the *RG*. When compared to negative feedback current, a smaller difference in positive feedback current over individual AuNWs from the bulk substrate was recorded because of the positive background current contributed from the bulk gold film. The differences in overall current between negative and positive feedback current images (Fig. 4.5.1A and 4.5.2B) and even between different positive feedback current images of individual AuNWs (Fig. 4.5.2B and 4.5.6A) were due to different batches of mediator solutions and sometimes due to partial fouling of the probes used.

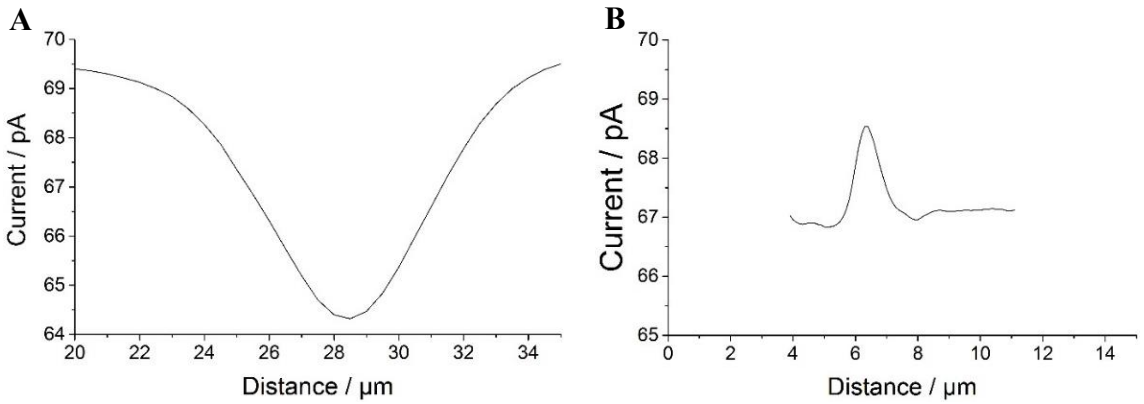

Figure 4.5.3: SECM line scans across individual AuNWs with (A) negative (over glass slide) and (B) positive (over gold-coated glass slide) feedback current responses. The line scans were obtained with a 300 nm radius Pt probe at a potential of 0.3 V in 1.5 mM ferrocene methanol solution. Published by the Royal Society of Chemistry.

Although, the apparent width of AuNW in positive feedback image was almost independent of the *RG* of the tip, it was largely dependent on the Pt disk diameter. The AuNW appeared wider than its actual diameter (Fig. 4.5.2B and 4.5.3B), whereas, the apparent length of the nanowire was similar to its actual length as seen in the representative AFM image (Fig. 4.5.2D). Since the apparent dimensions of the nanostructures in high-resolution SECM are largely dependent on the probe diameters, the nanostructures appeared even broader in the earlier reports by Amemiya and co-workers [27,28], where they used relatively larger diameter probes to image the gold nanoband and carbon nanotube. However, the broadening of the carbon nanotube was significantly decreased when scanned across with a 1.5 µm diameter Pt probe. The apparent width of the nanotube was around 4 times the diameter of the Pt disk [28]. The observation correlated closely to our studies with 300 nm radius probe, where the apparent width in positive feedback image was around 3 times the diameter of the Pt disk. The recent publications by Mirkin and co-workers have reported the imaging and catalytic efficiency of individual gold nanoparticles (AuNPs, 10-20 nm diameter) with an extremely small probe of radius ≥ 3 nm [29,38]. Although, they could record a positive feedback current over individual AuNPs with a probe of radius 42 nm (where the AuNPs were electrically connected via underlying highly ordered pyrolytic graphite surface), the image resolution impressively improved with the decreasing probe sizes. With the probes of radii 14 nm and 3 nm, the SECM measurements

quite close to actual diameters were made for 20 nm and 10 nm diameter AuNPs, respectively. Although, a closer correlation of apparent and actual nano-dimensions could be achieved in SECM images with decreasing probe sizes, the Wollaston-based 300 nm radius Pt probe appeared to be an appropriate choice to image immobilized AuNWs in our case. As seen in representative AFM images (Fig. 4.5.2C and inset of Fig. 4.5.5), the assembly of AuNWs over substrates was not even. Entangled AuNWs bundles of various sizes were frequently encountered during the constant height scans of substrates which could have easily destroyed etched or capillary pulled nano-probes with smaller *RG*s. The probes used in our studies were robust enough to be used again after crashing to these bundles with intermittent cleaning and polishing.

Since the apparent dimensions of individual AuNWs immobilized on gold coated glass slides correlated better with the actual AuNWs dimensions, the same was chosen for enzyme (HRP) activity imaging studies.

Subsequent feedback and activity imaging of HRP-linked AuNWs

For imaging of peroxidase activity, HRP was covalently linked to AuNWs by EDC-NHS method. The HRP-linked AuNWs were then immobilized on the gold-coated glass slide. Generally, the catalytic cycle of HRP involves the reaction of ferric form of the protein (Fe^{III}) with H_2O_2 to give the ferryloxy radical (Fe^{IV}=O) of the enzyme known as compound I. The ferryloxy radical reacts with an electron donor to give the non-radical ferryloxy form (Fe^{IV}=O) of the enzyme known as compound II which then reacts with H_2O_2 to give an oxyperoxidase form of the enzyme that decomposes to superoxide and Fe^{III}. The resulting HRP activity could either be imaged by recording the peroxide consumption at high overpotential (~1 V) [39] or by imaging the reduction of electron donor oxidized by HRP. Ferrocene methanol was used as electron donor for HRP in this work which was then reduced at the Pt probe at a potential of 0 V. A similar mechanism was used previously for SECM imaging of HRP-labelled protein microarrays [33]. As shown in Fig. 4.5.4, at 0.3 V probe potential, the AuNWs were imaged in feedback mode, whereas, by switching the probe potential to 0 V after addition of H_2O_2, peroxidase activity of HRP covalently linked to AuNWs can be imaged subsequently in the same experiment.

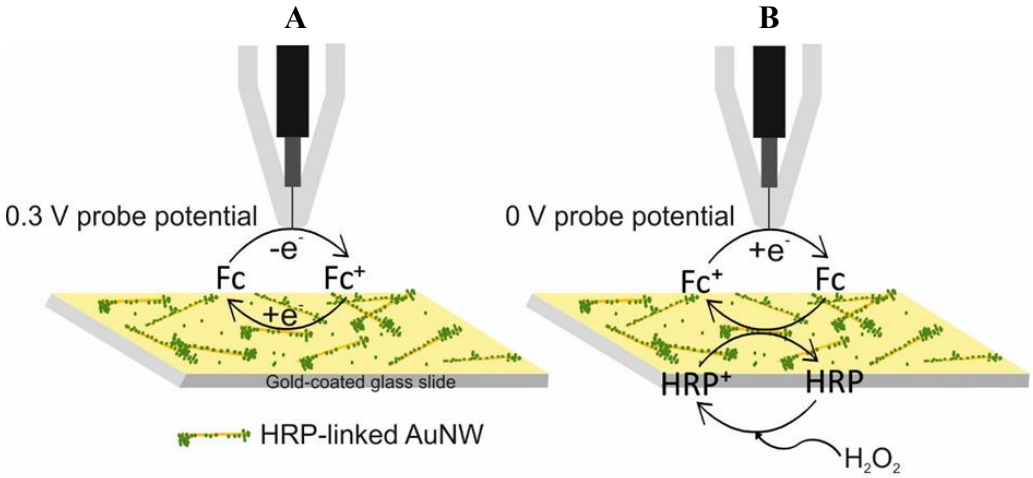

Figure 4.5.4: Schematic representation of (A) positive feedback at 0.3 V probe potential and (B) SG/TC at 0 V probe potential over HRP-linked AuNWs in ferrocene methanol solution. (Diagram not to scale). Published by the Royal Society of Chemistry.

Figure 4.5.5A shows the positive feedback image of ferrocene methanol recycling at AuNWs clusters (representative AFM image inset of Fig. 4.5.5) at probe potential of 0.3 V. When the potential was switched to 0 V, no current was recorded at the probe (Fig. 4.5.5B). However, when H_2O_2 was added to the same mediator solution, HRP activity was imaged at AuNWs clusters by reduction of HRP oxidized ferrocene methanol at Pt UME in substrate generation/tip collection (SG/TC) mode (Fig. 4.5.5C). Interestingly, although the measured current in SG/TC imaging of AuNWs clusters was nearly half of the measured current in positive feedback image, a current difference of ~30 pA was recorded over the AuNWs clusters from the bulk substrate in SG/TC mode. This difference was significantly higher than the current difference (~20 pA) recorded in positive feedback mode. The observation suggests the localization of HRP activity over and around AuNWs clusters rather than on bulk substrate surface resulting in less background current in SG/TC mode at 0 V. This also confirms the stable covalent linking of HRP with the AuNWs. In positive feedback image at 0.3 V, the bulk gold substrate surface contributed towards higher background current, thus resulted in lesser current difference over AuNWs. However, a considerably higher positive feedback response from the AuNWs from the bulk gold substrate further supported our above observation that covalent-linking of HRP with the carboxyl groups of thiol-modified AuNWs did not interfere with recycling of ferrocene methanol mediator at 0.3 V probe potential (Fig. 4.5.5A). The same was also observed by

unhindered positive feedback response from individual AuNWs (HRP-modified) at 0.3 V probe potential in Fig. 4.5.6A.

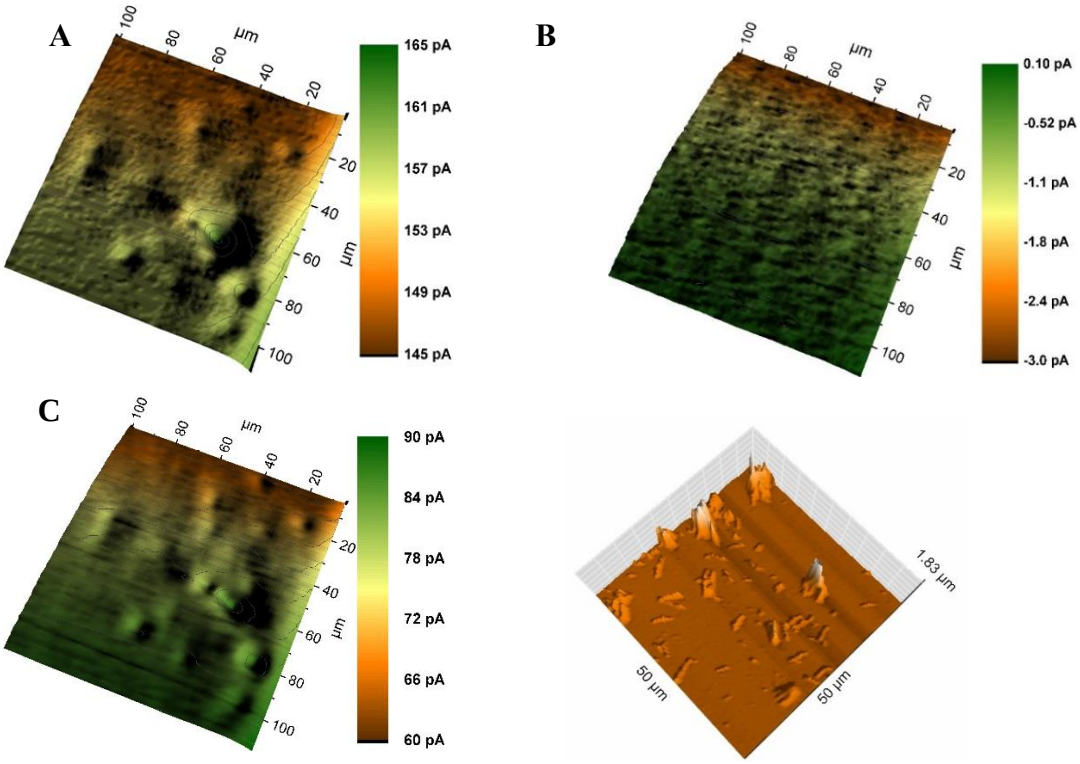

Figure 4.5.5: SECM images of HRP-linked AuNWs clusters immobilized on a gold-coated glass slide at (A) 0.3 V probe potential (positive feedback), (B) 0 V probe potential, and (C) 0 V probe potential after addition of 0.3 % H_2O_2 (SG/TC). The images were recorded with Pt probes of radii 1-3 µm at a scan rate of 50 µm s^{-1} in 1.5 mM ferrocene methanol solution in pH 6 SPB. Inset: Representative AFM image of the same substrate. Published by the Royal Society of Chemistry.

Some of the recent research focused on the use of single AuNW or AuNP to study catalytic properties and sensing [25–29,35,36] which prompted us to image the distribution of HRP activity over individual AuNWs. Fig. 4.5.6A and B show the images of individual AuNWs in feedback and SG/TC modes at 0.3 V and 0 V (in presence of H_2O_2) probe potentials, respectively. Interestingly, although the HRP activity was distributed along the entire length of AuNWs, higher enzymatic activity was imaged at the ends of nanowires. The representative AFM image of the HRP-linked AuNWs (Fig. 4.5.6C) shows that HRP was immobilized

throughout the length of nanowire. However, the ends of AuNWs showed relatively larger aggregation of immobilized HRP which correlated well with the corresponding SECM image.

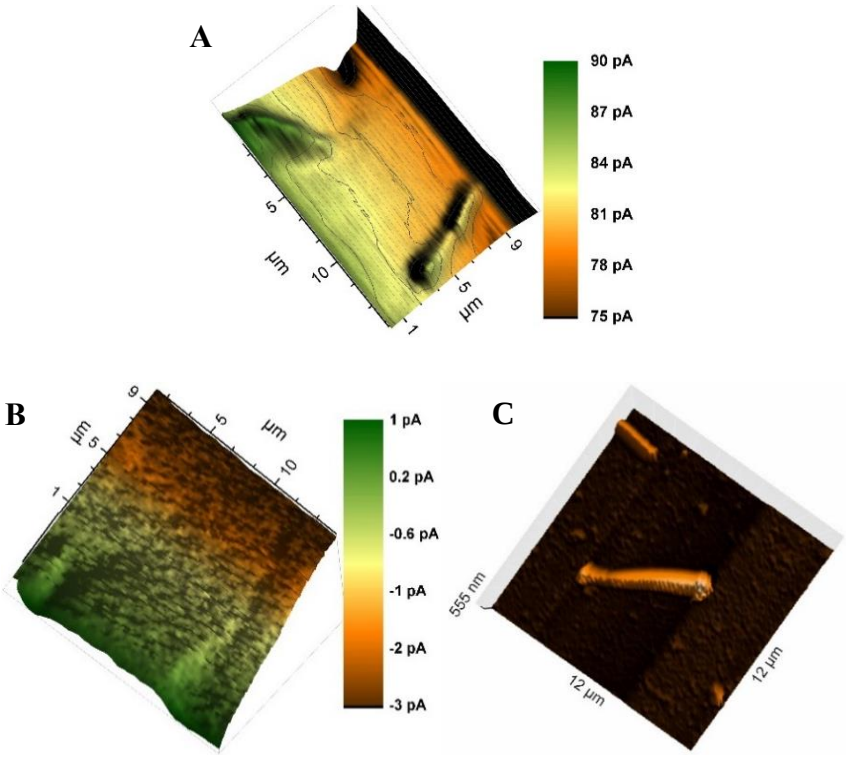

Figure 4.5.6: SECM images of individual HRP-linked AuNWs immobilized on a gold-coated glass slide at (A) 0.3 V probe potential (Positive feedback) and (B) 0 V probe potential after addition of 0.3 % H_2O_2 (SG/TC). The images were recorded with a 300 nm radius probe at a scan rate of 5 µm s^{-1} in 1.5 mM ferrocene methanol solution in pH 6 SPB. (C) Representative AFM image of the same substrate. Published by the Royal Society of Chemistry.

Since the current recorded at individual AuNWs in SG/TC mode was very small (~2 pA), a clear image from the background current could not be differentiated; so, a comparison with positive feedback current cannot be made. A drift in current along the length of the wire was observed mainly due to a slight tilt in the substrate. Since the measured enzymatic activity in SG/TC mode was small, the drift appears quite pronounced in the image. A similar drift (but not so pronounced) was also observed in the corresponding positive feedback image of AuNWs. This is one of the first reports (to the best of our knowledge), where SECM imaging of enzymatic activity at individual nanomaterial was achieved. A similar amount of current (~2 pA) was mapped at around 1 V probe potential over individual AuNPs (~200 nm diameter) with a bias potential of 0.4 V by Wain's research group [39]. Thus, the similar current over unbiased

HRP-linked AuNWs at 0 V probe potential provides a more feasible alternative for signal mapping over various DNA or protein microarrays.

4.5.4 Conclusion

Subsequent feedback and enzymatic peroxidase activity over individual AuNWs were imaged by a 300 nm radius Wollaston-based Pt probe in constant height mode of SECM. The SECM imaging of enzymatic activity at individual nanomaterial is reported for the first time. The observations could be extended to study catalytic properties of other nanomaterials or to characterize enzyme modified electrode surfaces (biased or unbiased) or to map amplified signals over HRP-linked DNA or protein microarrays with sub-micrometer resolutions. The negative and positive feedback responses of individual AuNWs immobilized on insulating and conducting film surfaces, respectively, provided an insight into the factors affecting the effective recycling of mediator by conducting nanomaterials particularly by 1-D nanostructures. The imaging with positive feedback current response of individual AuNWs (~140 nm wide) over a bulk conducting substrate by a rather large 300 nm radius Pt probe also eliminates the requirement for very small probes for imaging of unmodified or variously modified conductive nanomaterials. The work also establishes the importance of constant height mode of SECM in surface characterization of transducers after nanomaterial/biomolecule immobilization in biosensing applications providing additional electrical connectivity/activity distribution data to the topographic details provided by other microscopic methods.

4.5.5 Supporting information

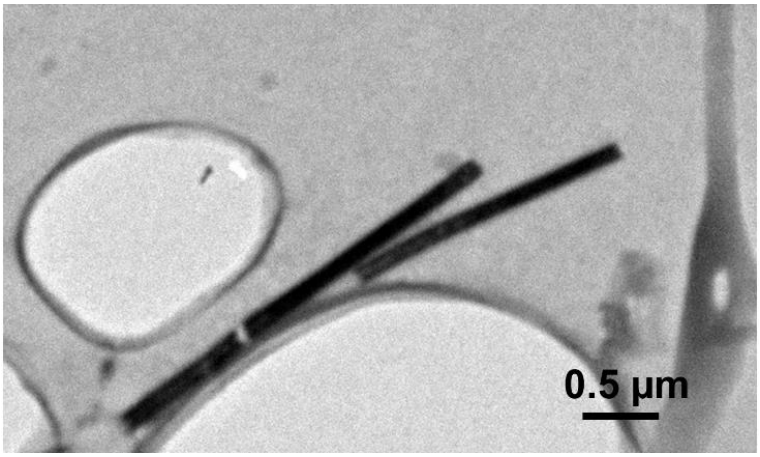

Figure 4.5.S1: Transmission electron microscopic image of synthesized gold nanowires. Published by the Royal Society of Chemistry.

References

[1] A.J. Bard, F.R.F. Fan, J. Kwak, O. Lev, Scanning electrochemical microscopy. Introduction and principles, Anal. Chem. 61 (1989) 132–138.

[2] A.J. Bard, Electronanalytical chemistry, Marcel Dekker, New York, 1994.

[3] S. Bergner, P. Vatsyayan, F.-M. Matysik, Recent advances in high resolution scanning electrochemical microscopy of living cells--a review, Anal. Chim. Acta 775 (2013) 1–13.

[4] S. Amemiya, A.J. Bard, F.R.F. Fan, M.V. Mirkin, P.R. Unwin, Scanning electrochemical microscopy, Annu. Rev. Anal. Chem. 1 (2008) 95–131.

[5] P. Sun, F.O. Laforge, T.P. Abeyweera, S.A. Rotenberg, J. Carpino, M.V. Mirkin, Nanoelectrochemistry of mammalian cells, Proc. Natl. Acad. Sci. 105 (2008) 443–448.

[6] F.O. Laforge, J. Velmurugan, Y. Wang, M.V. Mirkin, Nanoscale imaging of surface topography and reactivity with the scanning electrochemical microscopy, Anal. Chem. 81 (2009) 3143–3150.

[7] L. Stoica, S. Neugebauer, W. Schuhmann, Scanning electrochemical microscopy (SECM) as a tool in biosensor research, in: R. Renneberg, F. Lisdat (Eds.), Biosensing 21st Century, Springer Berlin Heidelberg, Berlin, Heidelberg, 2008: pp. 455–492.

[8] M. Holzinger, A. Le Goff, S. Cosnier, Nanomaterials for biosensing applications: A review, Front. Chem. 2 (2014) 63.

[9] P. Vatsyayan, Recent advances in the study of electrochemistry of redox proteins, in: F.-M. Matysik (Ed.), Trends Bioelectroanal., Springer International Publishing, Cham, 2017: pp. 223–262.

[10] D. Battistel, F. Baldi, M. Gallo, C. Faleri, S. Daniele, Characterisation of biosynthesised silver nanoparticles by scanning electrochemical microscopy (SECM) and voltammetry, Talanta 132 (2015) 294–300.

[11] A.K. Wanekaya, W. Chen, N.V. Myung, A. Mulchandani, Nanowire-based electrochemical biosensors, Electroanalysis 18 (2006) 533–550.

[12] U. Yogeswaran, S.-M. Chen, A review on the electrochemical sensors and biosensors composed of nanowires as sensing material, Sensors 8 (2008) 290–313.

[13] A. Kumar M., S. Jung, T. Ji, Protein biosensors based on polymer nanowires, carbon nanotubes and zinc oxide nanorods, Sensors 11 (2011) 5087–5111.

[14] S. Cherevko, C.H. Chung, Gold nanowire array electrode for non-enzymatic voltammetric and amperometric glucose detection, Sensors Actuators, B Chem. 142 (2009) 216–223.

[15] X. Zhang, D. Li, L. Bourgeois, H. Wang, P.A. Webley, Direct electrodeposition of porous gold nanowire arrays for biosensing applications, ChemPhysChem. 10 (2009) 436–441.

[16] M. Yang, F. Qu, Y. Li, Y. He, G. Shen, R. Yu, Direct electrochemistry of hemoglobin in gold nanowire array, Biosens. Bioelectron. 23 (2007) 414–420.

[17] J. Xu, F. Shang, J.H.T. Luong, K.M. Razeeb, J.D. Glennon, Direct electrochemistry of horseradish peroxidase immobilized on a monolayer modified nanowire array electrode, Biosens. Bioelectron. 25 (2010) 1313–1318.

[18] G. Lu, J.S. Cooper, P.J. Mcginn, SECM imaging of electrocatalytic activity for oxygen reduction reaction on thin film materials, Electrochim. Acta 52 (2007) 5172–5181.

[19] S. Aravamudhan, A. Kumar, S. Mohapatra, S. Bhansali, Sensitive estimation of total cholesterol in blood using Au nanowires based micro-fluidic platform, Biosens. Bioelectron. 22 (2007) 2289–2294.

[20] S. Aravamudhan, N.S. Ramgir, S. Bhansali, Electrochemical biosensor for targeted detection in blood using aligned Au nanowires, Sensors Actuators, B Chem. 127 (2007) 29–35.
[21] A. Cusmà, A. Curulli, D. Zane, S. Kaciulis, G. Padeletti, Feasibility of enzyme biosensors based on gold nanowires, Mater. Sci. Eng. C. 27 (2007) 1158–1161.
[22] S. Guo, D. Wen, S. Dong, E. Wang, Gold nanowire assembling architecture for H_2O_2 electrochemical sensor, Talanta 77 (2009) 1510–1517.
[23] H. Zhong, R. Yuan, Y. Chai, W. Li, Y. Zhang, C. Wang, Amperometric biosensor for hydrogen peroxide based on horseradish peroxidase onto gold nanowires and TiO_2 nanoparticles, Bioprocess Biosyst. Eng. 34 (2011) 923–930.
[24] C.C. Mayorga-Martinez, M. Guix, R.E. Madrid, A. Merkoçi, Bimetallic nanowires as electrocatalysts for nonenzymatic real-time impedancimetric detection of glucose, Chem. Commun. 48 (2012) 1686–1688.
[25] K. Dawson, M. Baudequin, A. O'Riordan, Single on-chip gold nanowires for electrochemical biosensing of glucose, Analyst 136 (2011) 4507–4513.
[26] K. Dawson, A. Wahl, R. Murphy, A. O'Riordan, Electroanalysis at single gold nanowire electrodes, J. Phys. Chem. C 116 (2012) 14665–14673.
[27] H. Xiong, J. Kim, E. Kim, S. Amemiya, Scanning electrochemical microscopy of one-dimensional nanostructure: Effects of nanostructure dimensions on the tip feedback current under unbiased conditions, J. Electroanal. Chem. 629 (2009) 78–86.
[28] J. Kim, H. Xiong, M. Hofmann, J. Kong, S. Amemiya, Scanning electrochemical microscopy of individual single-walled carbon nanotubes, Anal. Chem. 82 (2010) 1605–1607.
[29] T. Sun, Y. Yu, B.J. Zacher, M.V. Mirkin, Scanning electrochemical microscopy of individual catalytic nanoparticles, Angew. Chem. Int. Ed. 53 (2014) 14120–14123.
[30] A.G. Güell, K.E. Meadows, P.V. Dudin, N. Ebejer, J.V. Macpherson, P.R. Unwin, Mapping nanoscale electrochemistry of individual single-walled carbon nanotubes, Nano Lett. 14 (2014) 220–224.
[31] A.G. Guell, N. Ebejer, M.E. Snowden, K. McKelvey, J.V. Macpherson, P.R. Unwin, Quantitative nanoscale visualization of heterogeneous electron transfer rates in 2D carbon nanotube networks, Proc. Natl. Acad. Sci. 109 (2012) 11487–11492.
[32] H. Shiku, T. Matsue, I. Uchida, Detection of microspotted carcinoembryonic antigen on a glass substrate by scanning electrochemical microscopy, Anal. Chem. 68 (1996) 1276–1278.
[33] T. Kai, S. Chen, E. Monterroso, F. Zhou, Continuous nanoflow-scanning electrochemical microscopy: Voltammetric characterization and application for accurate and reproducible imaging of enzyme-labeled protein microarrays, Anal. Chem. 87 (2015) 4523–4529.
[34] E. Fortin, P. Mailley, L. Lacroix, S. Szunerits, Imaging of DNA hybridization on microscopic polypyrrole patterns using scanning electrochemical microscopy (SECM): the HRP bio-catalyzed oxidation of 4-chloro-1-naphthol, Analyst 131 (2006) 186–193.
[35] U. Saxena, M. Chakraborty, P. Goswami, Covalent immobilization of cholesterol oxidase on self-assembled gold nanoparticles for highly sensitive amperometric detection of cholesterol in real samples, Biosens. Bioelectron. 26 (2011) 3037–3043.
[36] A.I. Oleinick, D. Battistel, S. Daniele, I. Svir, C. Amatore, Simple and clear evidence for positive feedback limitation by bipolar conductors, Anal. Chem. 83 (2011) 4887–4893.
[37] H. Xiong, J. Guo, S. Amemiya, Probing heterogeneous electron transfer at an unbiased conductor by scanning electrochemical microscopy in the feedback mode, Anal. Chem.

79 (2007) 2735–2744.
[38] M. Zhou, Y. Yu, P. Blanchard, M.V. Mirkin, Surface patterning using diazonium ink filled nanopipette, Anal. Chem. 87 (2015) 10956–10962.
[39] M.A. O'Connell, J.R. Lewis, A.J. Wain, Electrochemical imaging of hydrogen peroxide generation at individual gold nanoparticles, Chem. Commun. 51 (2015) 10314–10317.

4.6 Complementary analytical imaging techniques for the characterization of pretreated carbon fiber reinforced plastics

Stefan Viehbeck, Christian Iffelsberger and Frank-Michael Matysik

Composite Part A 113 (2018) 32–39

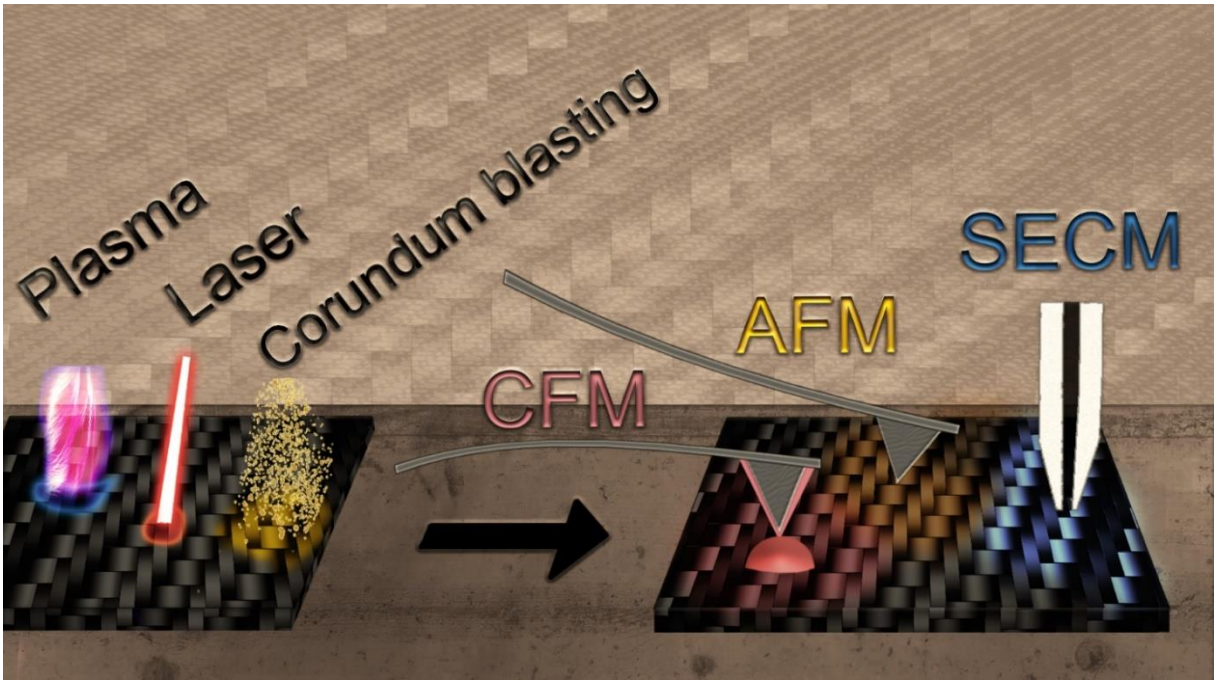

Abstract

In this work the complementary characterization of pretreatment techniques for adhesive bonding of carbon fiber reinforced plastics (CFRP) is presented. Industrial CFRP plates were pretreated with laser, plasma and corundum blasting abrasive techniques followed by chemical activation. The combined use of atomic force microscopy and chemical force microscopy enabled the characterization of the surface morphology and the specific adhesion force between a chemically functionalized cantilever and the pretreated surfaces simulating the adhesive bond. Complementary measurements with scanning electrochemical microscopy and X-ray photoelectron spectroscopy supported the experimental findings and delivered additional information about the chemical structure of the surfaces. A comparison of experimental data of mechanical tensile shear strength measurements and the applied analytical methods revealed a valid correlation of microscopic and macroscopic techniques.

4.6.1 Introduction

Carbon fiber reinforced plastics (CFRP) represent an attractive class of composite material consisting of carbon fibers immersed in a surrounding plastic matrix. The combination of the materials can strengthen their individual properties so that CFRP possess a greater ratio of modulus and tensile strength to their weight, a lower thermal coefficient and a higher internal damping compared to steel or lightweight alloys such as aluminum or titanium [1]. These characteristics lead to a broad field of commercial and industrial applications including military and commercial aircrafts, automotive, space and sporting goods [2] to name just a few examples. In the automotive industry CFRP components are used to construct body parts, chassis or engine components of lighter weight and with a better stability.

The special chemical composition of workpieces consisting of CFRP requires different joining methods than conventional aluminum, steel or iron parts. Riveting, welding or screwing are not suitable for composite lightweight car manufacturing [3]. In addition to that, adhesive bonding won't adhere properly on a recently manufactured CFRP part. Since large scale and automated production/compression tools require release agents and thereby contaminate the surface of the manufactured parts. Different pretreatment techniques are used to remove the release agent and activate the surface to enable adhesive bonding. The quality aspect of the CFRP bonding is regarded as a crucial safety issue. Thus, new methods for quality evaluation are needed. Currently only macroscopic measurements such as tensile shear strength and peel tests are applied to evaluate the adhesive bonding [4]. The surface is evaluated according to the fracturing and conclusively regarding the efficiency of the surface pretreatment technique. For detailed information on the impact of the surface pretreatment techniques and possible consequences for the adhesive bonding, further investigations and new analytical methods must be established.

In scanning probe microscopy, the information is generated through interactions between a probe, which is scanned across a substrate. The result of this measuring process is expressed as an image [5]. Beside the topographical mapping [6] atomic force microscopy (AFM) possesses the potential for the detection of interacting forces between the cantilever and a surface [7,8]. Especially for biochemical applications this measuring mode is often combined with a chemically modified cantilever [9]. Using this chemical force microscopy (CFM) recent studies show the specific interaction of functional groups and a biolayer [10]. The strength of AFM, the atomic [11,12] or molecular [13] resolution, is often compromised by the restriction to

relatively small surface areas. For studying atomic or molecular effects and correlating them with macroscopic surface properties the uniformity of the studied surface is a prerequisite. From the practical point of view the microscopic surface properties are often determined by many various effects occurring at different spots across the surface. This aspect is a limitation of many high-resolution scanning probe techniques for studying workpieces at industrial scale and size. The lack of representative characterization of larger surface areas can be considered as a disadvantage of AFM in the context of industrial applications.

Scanning electrochemical microscopy (SECM), developed and characterized by A.J. Bard and coworkers [14], is an alternative scanning probe technique. SECM has found a wide range of applications ranging from biological surfaces [15,16] to novel inorganic materials [17]. Usually the studied substrate is fixed in an electrochemical cell and immersed in a solution containing an electroactive compound as mediator substance. In the amperometric measurement mode the current of an electrochemical reaction occurring at the ultramicroelectrode (UME) is used as signal to generate analytical information about the (electro)chemical activity and/or topographical details of the scanned surface, in a noninvasive way [18]. In SECM the probe is an UME with an electrode diameter of 25 µm or less resulting in a limited resolution compared to AFM. SECM is well suited for studying properties of inhomogeneous surfaces within areas of a few square mm [19]. This is particularly attractive for surfaces which can hardly be characterized by optical methods. In addition, surfaces exhibiting regions with different (electro)chemical properties like CFRP are ideal substrates for SECM studies. With its ability to scan across rather large surface areas SECM provides additional information to AFM (surface morphology and the electrochemical activity which correlates with the material composition of the surface in particular carbon fiber and epoxy matrix). A classical amperometric measuring principle is the feedback mode [14], with its two possibilities to influence the signal. In negative feedback, isolating surface regions hinder the mass transport of the mediator towards the UME resulting in a decreased current. A conductive substrate, however, leads to an enhanced current due to redox cycling between probe and substrate. As with other scanning probe techniques the resolution of the SECM depends on the probe size. Mathematical expressions for the analytical treatment of the measured currents are described in literature [20] and a comprehensive review of applications and experimental parameters for SECM studies was published recently by Polcari et al. [21]. Further surface techniques such as X-ray photoelectron spectroscopy [22,23] or time of flight – secondary ion mass spectrometry

(ToF-SIMS) [24] complement previous methods with information on the chemical composition of the surface.

In this work, advanced scanning probe techniques such as AFM/CFM and SECM were used for the characterization of the surface of CFRP plates and to correlate the effects of different activation procedures such as corundum blasting, plasma and laser activation prior to chemical activation of the CFRP/CFRP bonding. X-ray photoelectron spectroscopy was applied for additional characterization the chemical composition of the CFRP surface.

4.6.2 Experimental

Chemicals & Materials

Industrial CFRP plates, a commercially available material (Rhein Composite GmbH), were used after a resin transfer molding process. Different pretreatment techniques were applied to activate the CFRP surface and to remove the release agent and surface contamination. In detail, the following mechanical pretreatment methods were applied: (i) corundum blasting (4-5 bar, 120 grit), (ii) CO_2-laser activation (λ = 10.6 µm with 80 W), and (iii) atmospheric plasma treatment (~200°C with 10 kV). All techniques were applied with optimized settings as used under industrial conditions for comparable composites. In addition to mechanical pretreatment a chemical activator [25] (e.g. organometallic compound) was subsequently used to activate functional surface groups and to catalyze the reaction of an adhesive to the surface. The AFM and CFM studies were done either after mechanical pretreatments or after mechanical pretreatments combined with chemical activation.

Prior to all scanning probe experiments the CFRP plates were cut into squares with an area of a few square cm. The obtained squares were cleaned with ultrapure water and isopropanol (MS grade, Merck KGaA, Darmstadt, Germany). For a better correlation of the measured area with the different analytical techniques the examined surface was restricted by laying a square (1 cm^2) of a pierced (diameter 2.1 mm) silicone foil on the CFRP surface. The foil had a thickness of 100 µm (Elastosil, Wacker Chemie AG, Burghausen, Germany). The roughness of the corundum blasting treated sample made a fixation of the silicone foil with a fast curing 2-componenent epoxy resin (UHU GmbH & Co. KG, Buhl, Germany) necessary. All imaging experiments were performed within the restricted area. For all SECM experiments an aqueous solution of 1.5 mM ferrocene methanol (FcMeOH, 99 %, ABCR, Karlsruhe, Germany) as mediator and 0.2 M KNO_3 (analytical grade, Merck KGaA, Darmstadt, Germany) as supporting

electrolyte were used. The solution was prepared in ultrapure water with a resistivity higher than 18 MΩ cm (membraPure, Bodenheim, Germany).

As adhesive system a two-component polyurethane mixture (1:1) was used. The first component was formulated as a multicomponent polyol mixture [26]. A prepolymeric alcohol functionalized polybutadiene mixture (52.5 w.%, Polyvest EP HT, EVONIK Resource Efficiency GmbH, Marl, Germany) was used as reactive polyol. Thiodiethanol (9.0 w.%, Fluka Analytical) was used as chain extending component. The filler, kaolin (35.7 w.%), and the adhesion agent, trimethoxysilan (0.4 w.%), were obtained from Sigma-Aldrich. Dimethoxypolysiloxan (0.04 w.%, Sigma-Aldrich) was used as antifoaming agent. Pentaerythrit (2.0 w.%, Sigma-Aldrich) was used for crosslinking. To increase the reaction speed zirconium(IV)acetylacetonate was used as catalyst (0.4 w.%, Sigma-Aldrich) [27]. All components were homogenized with a Thinky Mixer ARE 250 (Thinky corp., Tokyo, Japan) for 2 minutes at 2000 rpm. The second component was a prepolymeric MDI isocyanate mixture (DOW Chemicals). Each component was filled in a cartridge and applied with the help of a two-component adhesive gun with multi-chamber mixing nozzle.

Instrumentation & Measurements

All AFM measurements were done with a commercial AFM (Nanosurf - FlexAFM). The topographical measurements were done in tapping mode and with Tap300Al-G cantilevers and the force measurements with Tap300GB-G and HQ:NSC19/Cr-Au cantilevers. For each cantilever calibrations of the deflection-sensitivity and the spring constant were done. The modification with functional alcohol groups was done via a self-assembled monolayer (SAM) process (Fig. 1B). For this a 5 mM solution of 11-mercapto-1-undecanol in ethanol (Sigma Aldrich) was used. To facilitate the handling, the cap of a micro vial was used and provided an ideal storing space for the cantilever and the thiol solution. The respective vial was filled with argon gas and used as cap to assure a clean reaction environment and was stored for 48 hours. XPS measurements were done to verify a successful monolayer formation.

During CFM measurements, the functionalized cantilever approaches the surface with a constant speed and the force of interactions (e.g. van der Waals interactions) between the surface and the cantilever is detected. At a certain distance the cantilever is deflected and attracted to the surface, which can be seen in a force distance diagram. During the retracting process the cantilever interacts with the surface and is retarded due to adhesion forces.

Consequently, two issues are obtained with force spectroscopy – the attractive forces for approaching the surface and the adhesion forces for retracting the cantilever [28]. With functionalized cantilevers specific interaction forces are detected (Fig. 4.6.1A). All AFM experiments were performed within an acoustic enclosure, defined laboratory environment and an active damping system to ensure reproducible results.

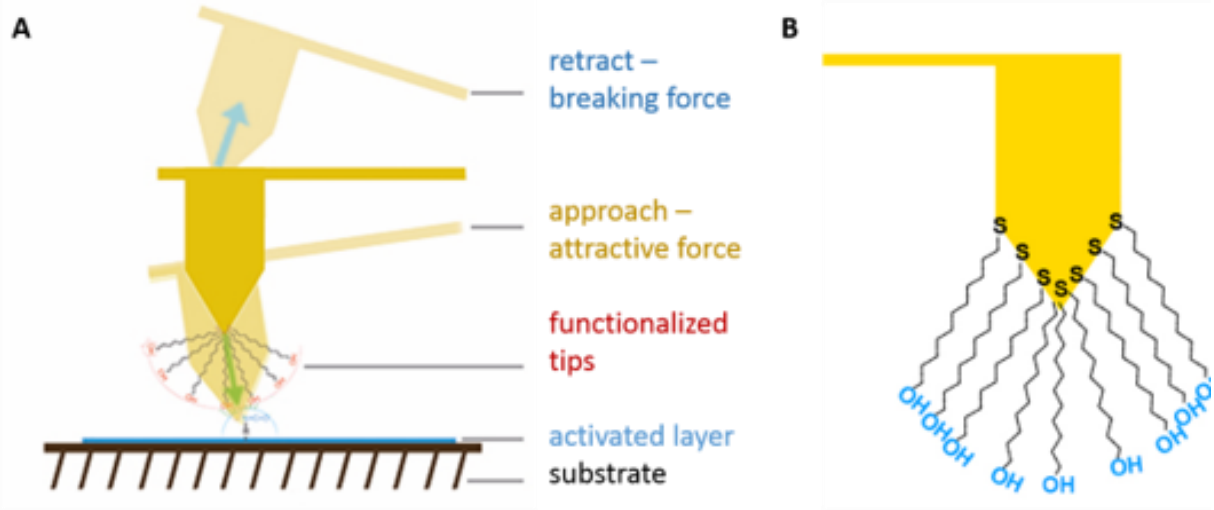

Figure 4.6.1. Schematic representation of the principle of AFM/CFM measurements (A) and functionalized cantilever (B).

SECM imaging was performed with a commercial SECM system CHI 920C (CH Instruments, Austin, USA) in a two-electrode setup with a Pt wire (0.5 mm diameter) as counter and quasi-reference electrode. All potentials refer to this quasi-reference electrode. A Pt disk UME with an electrode diameter of 25 µm and an RG of 2-3 was used as SECM probe. The probe was fabricated according to the procedure described elsewhere [17]. Prior to the imaging the substrate was levelled until a tilt less than 10 µm per mm^2 was achieved. The imaging for the reference, laser- and plasma-activated sample was performed at a tip-to-substrate distance of d < 10 µm, according to the measured current (I_M) of 60 % in relation to the current measured in the bulk phase (I_∞). For the corundum blasting treated sample I_M was 125 % relative to I_∞ corresponding to a tip-to-substrate distance of about 17 µm. The scan speed was 100 µm s^{-1} with a pixel size of 4 µm. After imaging by scanning probe techniques optical images of the studied area were taken using a Leica M205 C stereo microscope.

Tensile shear strength experiments

For macroscopic characterization, tensile shear strength measurements were conducted. For all tensile shear tests the substrates were cut into plates with a width of 45 mm and a length of 100 mm. The adhesive was applied onto the two substrates with a two-component adhesive gun and a multi chamber mixing nozzle. The two plates overlapped and adhered with an area of 45 mm x 20 mm. After 7 days of curing the complementary ends of both plates were fixed in the tensile shear testing device and sheared with a constant speed of 0.4 mm s^{-1}. Five independent measurements were done, and the result is calculated as mean value.

XPS experiments

X-ray photoelectron spectroscopy (XPS) was performed with a commercial system Phi 5000 VersaProbe III (Ulvac PHI, Hagisono, Chigasaki, Kanagawa, Japan). The same samples as used for the SECM experiments were studied at several positions with an incoming Al-K_α X-Ray of 100 µm with 100 W and 20 kV. First, a survey spectrum was measured to study all components on the surface. Afterwards a detail spectrum with 3 spots on each sample for C1s (278-298 eV), O1s (523-543 eV), N1s (391-411 eV), Si2p (94-114 eV) and Sn3d5 (480-500 eV) was recorded.

4.6.3 Results and discussion

Untreated CFRP surface

The optical characterization of the untreated CFRP plate is shown in Fig. 4.6.2A. It shows surface defects induced by mechanical stress. As expected, in the scanning electrochemical microscopy image (Fig. 4.6.2B), recorded with a 25 µm UME in 1.5 mM FcMeOH (bulk phase current of $I_\infty \approx 5.5$ nA, supporting information, Figure 4.6.S1), the predominant negative feedback (decreased current due to hindered mediator diffusion towards the UME and insulating surface) signal indicates a complete isolation of the carbon fiber by the epoxy resin. At spots where the epoxide layer is damaged the exposed carbon fibers show a positive feedback (increased current due to redox mediator recycling between UME and conductive surface). The adhesion force measured before the chemical activation (Fig. 4.6.2C) was predominantly in the range of 10 to 25 nN at some spots adhesion forces of up to 60 nN were measured. After chemical activation the chemical force measurements (Fig. 4.6.2D) showed an increase for the adhesion at the examined area proving the effectiveness of the chemical activation process.

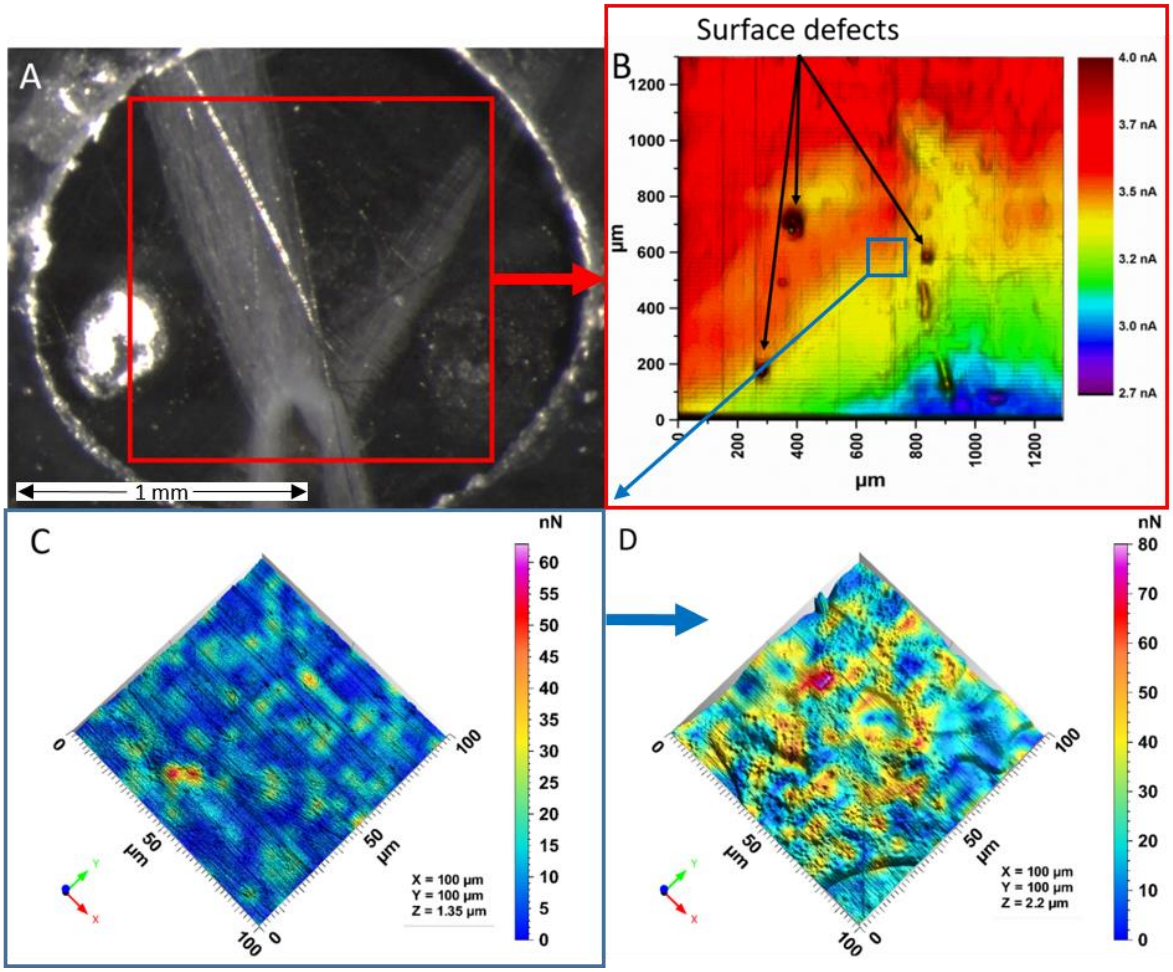

Figure 4.6.2. Characterization of untreated CFRP. (A) Optical image of the CFRP, the red square corresponds to the area imaged by SECM. (B) SECM false color image of the CFRP. AFM topography and adhesion force (false coloring) images before (C) and after (D) chemical activation.

Plasma pretreated CFRP surface

In case of plasma activation, the optical image shown in Fig. 4.6.3A indicates an increased roughness and topographical changes of the CFRP surface associated with several surface defects. With the SECM (Fig. 4.6.3B) a significantly increased current is shown in the plasma pretreated area. The intense energy of the plasma burned the epoxy resin and exposed carbon fibers at the outermost layer. Thus, the fibers are clearly imaged by a positive feedback response. The diameter of the 7 µm carbon fibers is magnified by the larger probe diameter of 25 µm. The generally increased current within the activated area could be derived from graphite

depositions due to pyrolysis of the epoxy resin. Further surface defects can be seen in the SECM image. For both AFM images (Fig. 4.6.3C and 4.6.3D) a localization within a defined area of the SECM image was possible.

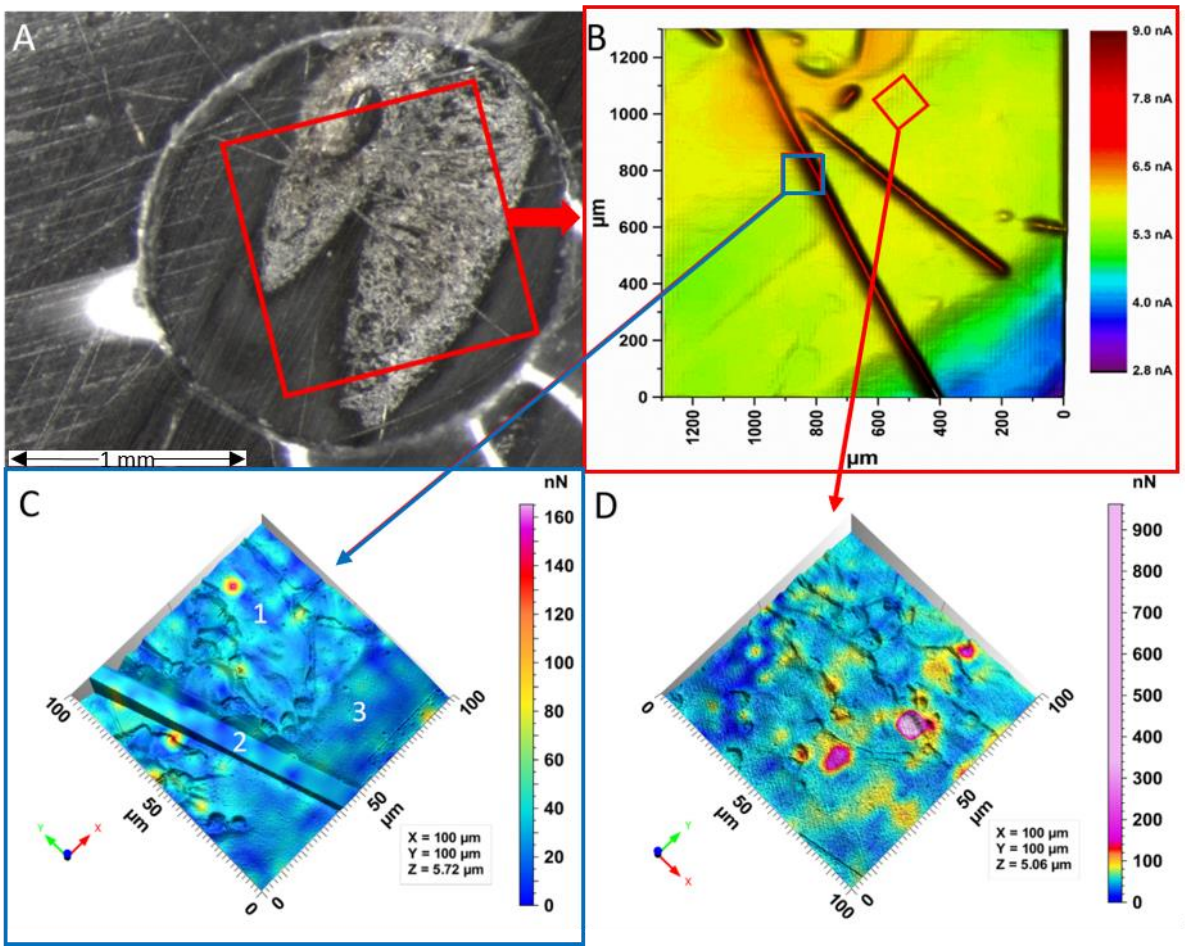

Figure 4.6.3: Characterization of plasma treated CFRP. (A) Optical image of the CFRP, the red square corresponds to the area imaged by SECM. (B) SECM false color image of the CFRP. AFM topography and adhesion force (false coloring) image before (C) and after (D) chemical activation. The imaged areas correspond to the red squares shown in (B).

The topographical information gained with AFM indicated an increased roughness for the plasma activated area (Fig. 4.6.3C-1) with a carbon fiber of about 7 µm in width (Fig. 4.6.3C-2). Regarding the surface and the adhesion force, no significant influence can be found between the fiber and the detected forces. However, the topographical image of the plasma activated area correlates well with a slightly increased adhesion force of 30-50 nN which compares to forces of 20-30 nN (Fig. 4.6.3C-3) for partially activated areas. Thus, the overall adhesion force in the plasma activated area is significantly increased. In addition, several spots with adhesion

forces up to 140 nN were detected within the plasma pretreated area. With additional chemical activation 3D chemical force microscopy indicated a higher overall adhesion force of 50-70 nN and various areas with forces larger 200 nN correlating to the topographical image of the plasma influenced spots were found.

Laser pretreated CFRP surface

Compared to the smooth appearance of the untreated CFRP, the laser pretreatment resulted in exposing single carbon fiber strands and in a grooved surface structure (Fig. 4.6.4A). This optical change correlates with the examinations reported in literature [29]. In the SECM image (Fig. 4.6.4B) exposed carbon fiber strands are indicated by a positive feedback current of up to 7.8 nA.

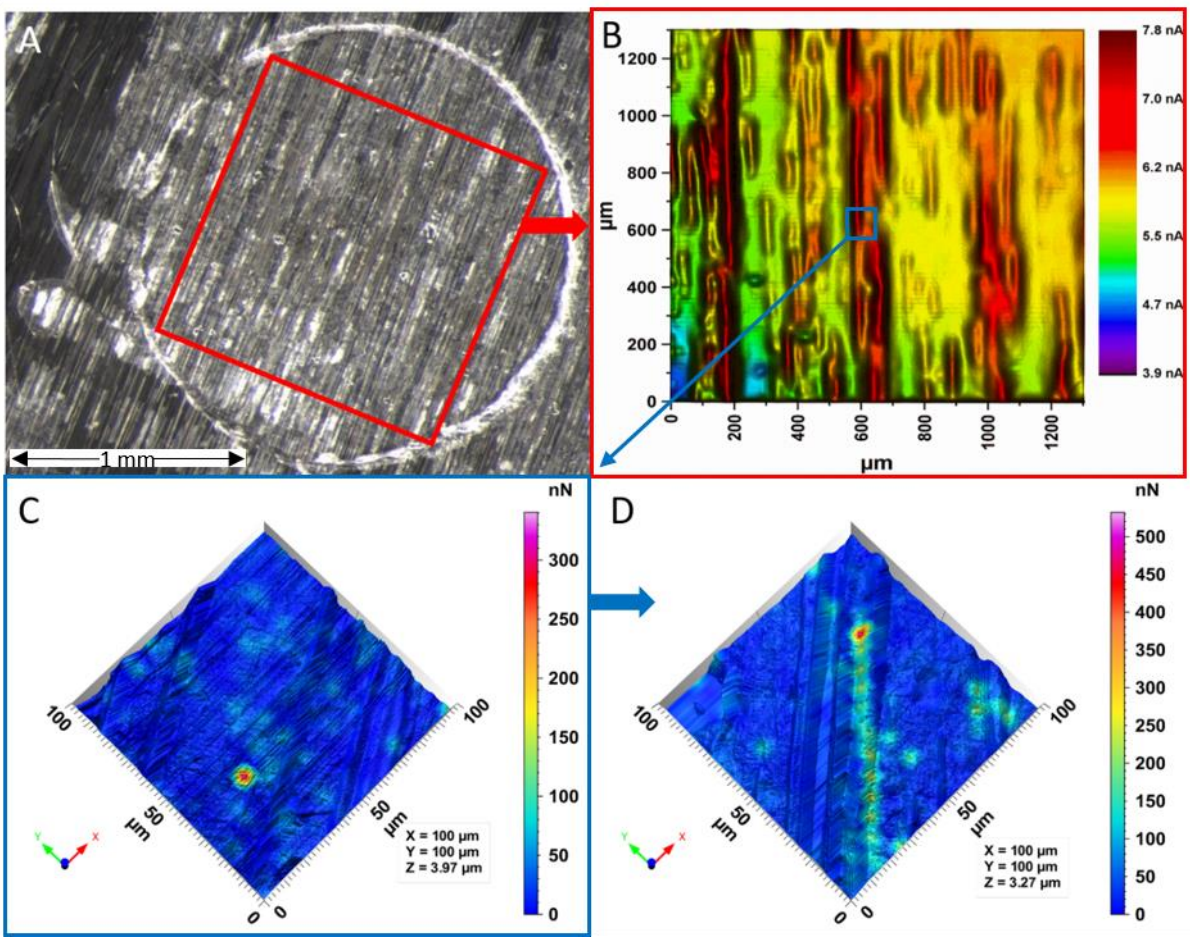

Figure 4.6.4: Characterization of laser treated CFRP. (A) Optical image of the CFRP, the red square corresponds to the area imaged by SECM. SECM false color image of the CFRP (B). AFM topography and adhesion force (false coloring) image before (C) and after (D) chemical activation.

The line by line pretreatment by the laser is clearly visible, showing the limited effectivity of a linear laser activation. Smaller currents in wide areas of the image between the fiber strands reflect the rough topography which is also shown in the AFM images (Fig. 4.6.4C and D). A reduction of the positive feedback by isolating areas of resin could also decrease the measured current. The adhesion force measured before the chemical activation (Fig. 4.6.4C) was slightly increased compared with the untreated CFRP. After chemical activation (Fig. 4.6.4D) an increased overall adhesion comparable to the untreated CFRP was detected. Interestingly, within the imaged grooves a strong increase in the adhesion force caused by a higher amount of activator could be seen. In all images the line structure of the laser induced impact can be seen.

CFRP surface pretreated by corundum blasting

With corundum blasting pretreatment a significant mechanical impact can be observed in the microscopic image (Fig. 4.6.5A). In contrast to laser pretreatment an increased erratic roughness was found. The electrochemical activity (Fig. 4.6.5B) was drastically increased reflected by an average feedback current of 7 nA and maximum currents up to 12 nA. Only small areas show a negative feedback which can be assigned to regions still covered with epoxy resin. The topographical inhomogeneity is also shown in the AFM images (Fig. 4.6.5C and D) with a maximum roughness of 8.4 µm. Compared to the untreated substrate the adhesion increases on several spots to 50-80 nN (Fig. 4.6.5C). The positive influence of the corundum blasting pretreatment is shown after applying a chemical activator (Fig. 4.6.5D). A maximum of 1.3 µN and an overall increased adhesion force within multiple activated areas of 100-250 nN were measured. Compared to the previously discussed activation techniques the adhesion forces were clearly enhanced and were distributed more homogenously over the surface.

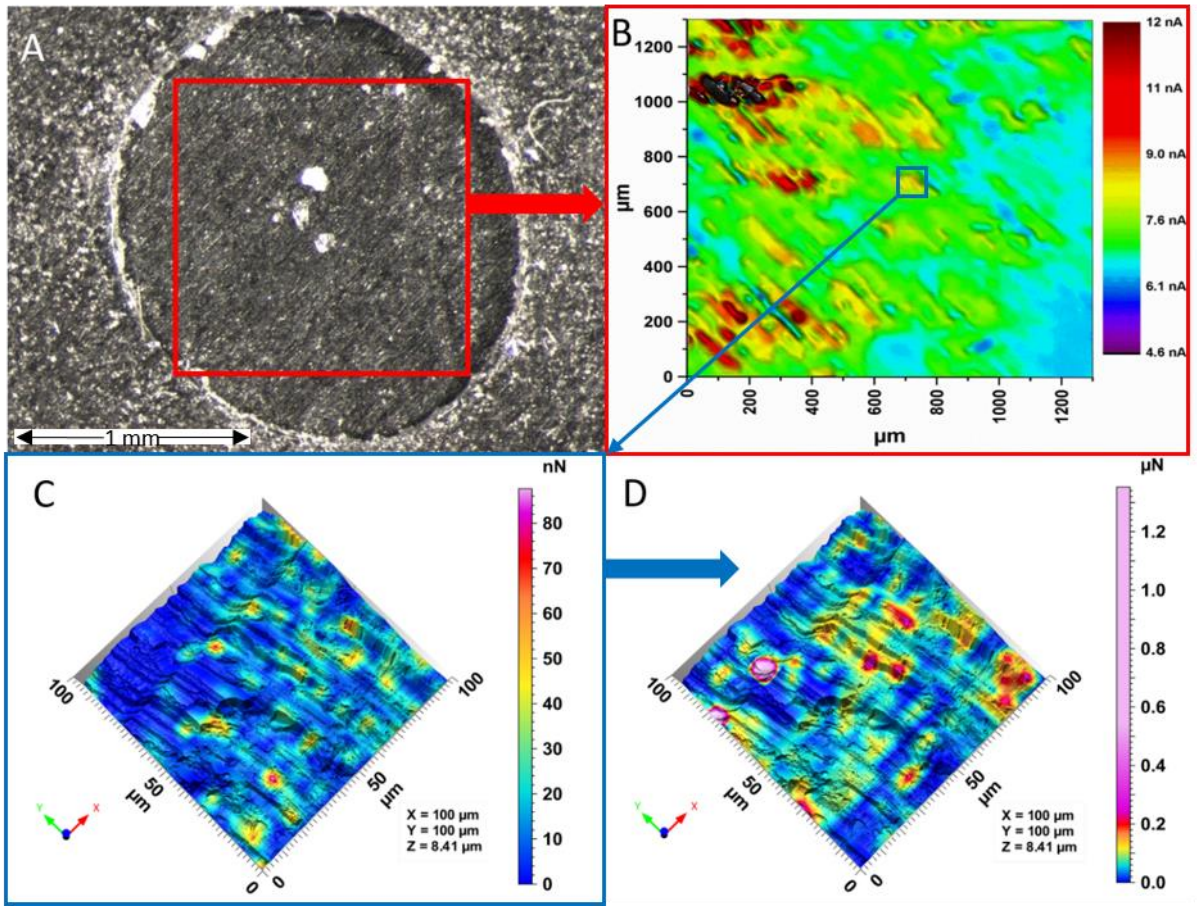

Figure 4.6.5: Characterization of CFRP treated by corundum blasting. (A) Optical image of the CFRP, the red square corresponds to the area imaged by SECM. (B) SECM false color image of the CFRP. AFM topography and adhesion force (false coloring) image before (C) and after (D) chemical activation.

XPS investigations

To study the influence of the chemical composition of the CFRP surfaces XPS measurements were carried out (Table 4.6.1). The reference sample and the surface pretreated by corundum blasting showed the highest amount of carbon. It was found that plasma and laser pretreated surfaces exhibited a high amount of oxygen.

For further evaluation the binding state of the carbon was examined (Fig. 4.6.6). Notably, the reference CFRP surface (Fig. 4.6.6A) was the only one with an intact epoxy layer represented by bound ester groups. The increased carbon signal can be deduced from surface contamination. Laser and plasma pretreatments (Fig. 4.6.6B and C) led to free functional groups, such as alcohol and carboxyl groups. However, the analysis of the binding state of the corundum

blasting pretreated surface indicated that the amount of alcohol groups was twice as much compared to the other pretreatments.

Without any pretreatment, the surface is non-reactive due to the lack of free functional groups. Laser and plasma pretreatment have a similar impact on the surface, generating reactive carboxyl and alcohol groups. The highest density of functional groups was generated with corundum blasting pretreatment. Depending on the distribution and the density of reactive groups an increased adhesion force is expected.

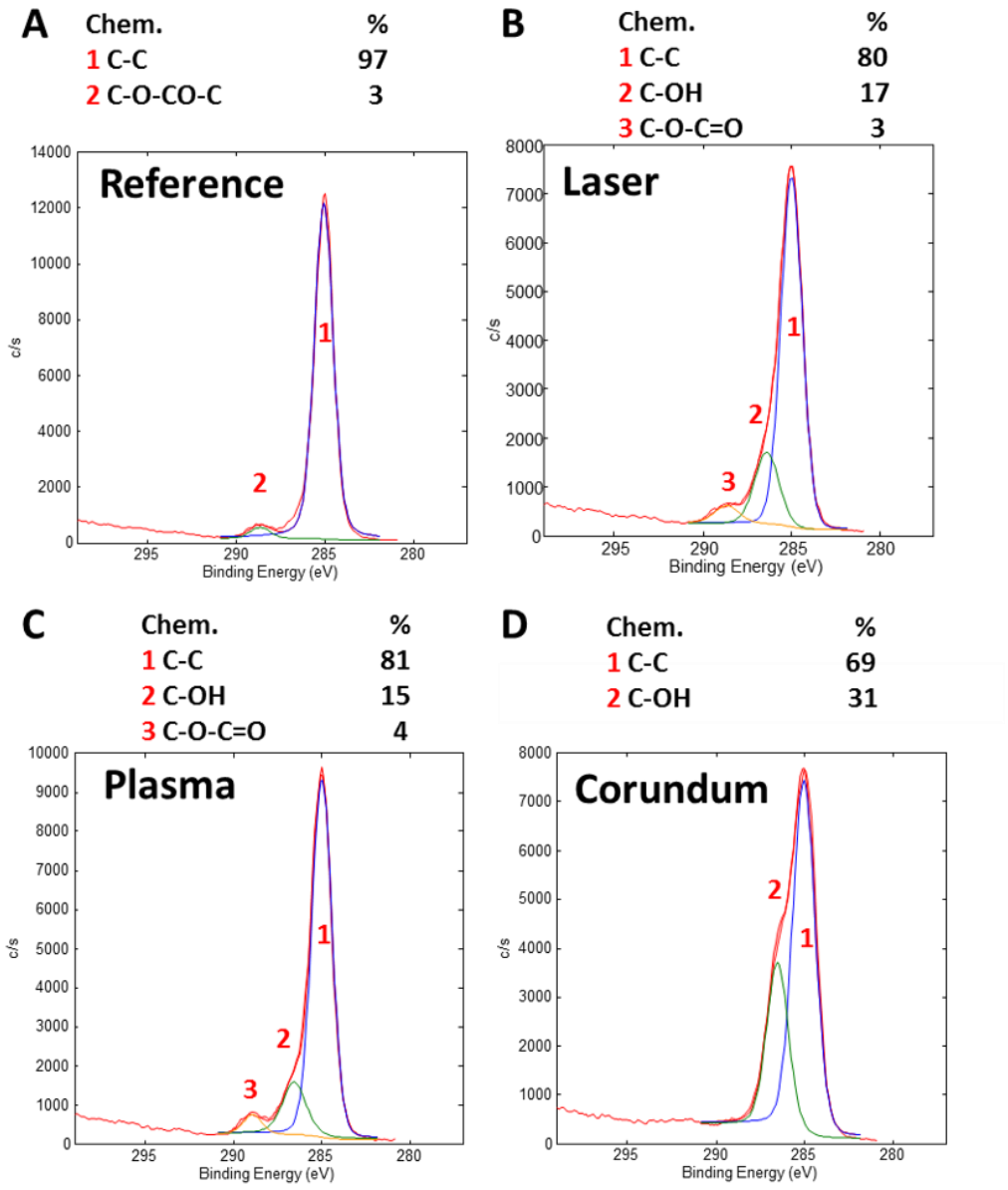

Figure 4.6.6: XPS measurements of CFRP surfaces with different pretreatment protocols. C1s signals are shown for (A) reference CFRP without pretreatment, (B) laser pretreated CFRP, (C) plasma pretreated CFRP, (D) corundum blasting pretreated CFRP.

Table 4.6.1: Quantification of surface atom distribution by XPS measurements.

XPS quantification						
sample	**C1s**	**N1s**	**O1s**	**Si2p**	**Sn3d5**	**C/O**
	Atom.-%	Atom.-%	Atom.-%	Atom.-%	Atom.-%	
reference	83.7	0.8	13.2	2.3	-	6.4
plasma	78.2	1.0	17.5	3.1	0.2	4.5
laser	77.2	1.4	17.5	3.9	-	4.5
corundum	82.7	2.0	14.8	0.5	-	5.6

Macroscopic mechanical tests

The tensile shear test was optically evaluated regarding the fracturing of the adhesive (Table 4.6.2). The samples without any mechanical pretreatment but with chemical activation (Fig. 4.6.7A) showed an adhesive failure of 70 % (N = 5). For plasma pretreatment with chemical activation (Fig. 4.6.7B) an adhesive detachment of 15 % (N = 5) was found and for laser pretreatment with chemical activation (Fig. 4.6.7C) the test showed an adhesive fracture of 35 % (N = 5). The different pretreatment techniques showed an improvement of the bonding between adhesive and CFRP. For corundum blasting with chemical activation (Fig. 4.6.7D) a 100 % cohesive fracturing was found.

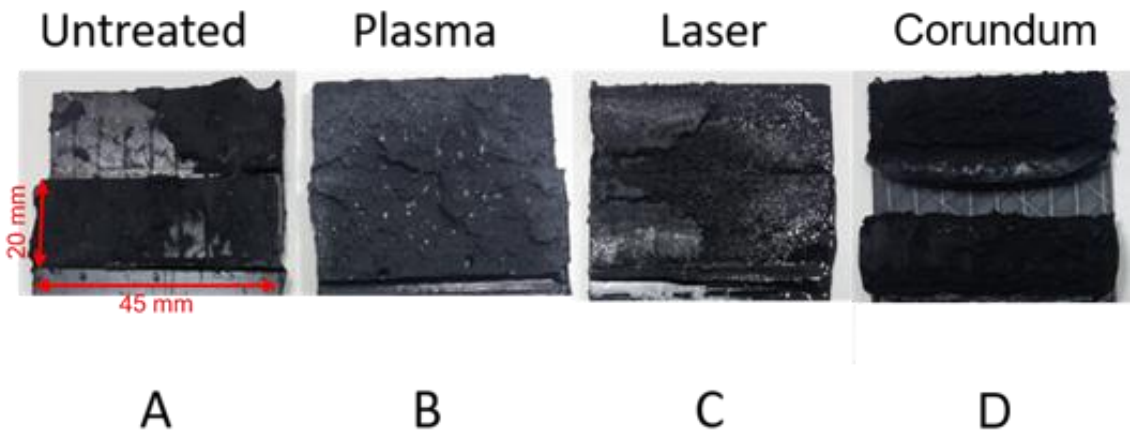

Figure 4.6.7: Representative examples for fracturing of the CFRP correlated with the different pretreatment methods.

Table 4.6.2: Tensile shear strength measurements of bonded CFRP samples pretreated with different methods.

Untreated + chemical	Plasma + chemical	Laser + chemical	Corundum blasting + chemical
70 % adhesive	15 % adhesive	35 % adhesive	100 % cohesive

4.6.4 Conclusion

The combination of optical microscopy with electrochemical imaging via SECM and adhesion force imaging via CFM was proven to be suitable for the evaluation of CFRP surface characteristics and for studying the influence of activation techniques in the context of adhesive bonding. With CFM a clear increase of adhesion forces after chemical activation of the substrate was identified and assigned to an enhancement concerning the reaction of the adhesive with the surface. With XPS the chemical activity of the substrate surface was studied supplementing the microscopic characterization. SECM imaging revealed the exposure of carbon fiber strands and enabled the characterization of the pretreatment methods for larger surface regions. The results of the macroscopic fracturing tests correlated well with the results of the advanced microscopic imaging techniques. The corundum blasting pretreatment combined with chemical activation was found to be the most effective pretreatment protocol for reliable adhesive bonding. All imaging techniques applied in this study added information for a better understanding of micro and macroscopic effects influencing the surface characteristics of CFRP substrates. Thus, the effectiveness of a bonding between CFRP substrates and adhesive can be foretold based on combined information derived from the analytical techniques applied in this report.

4.6.5 Supporting information

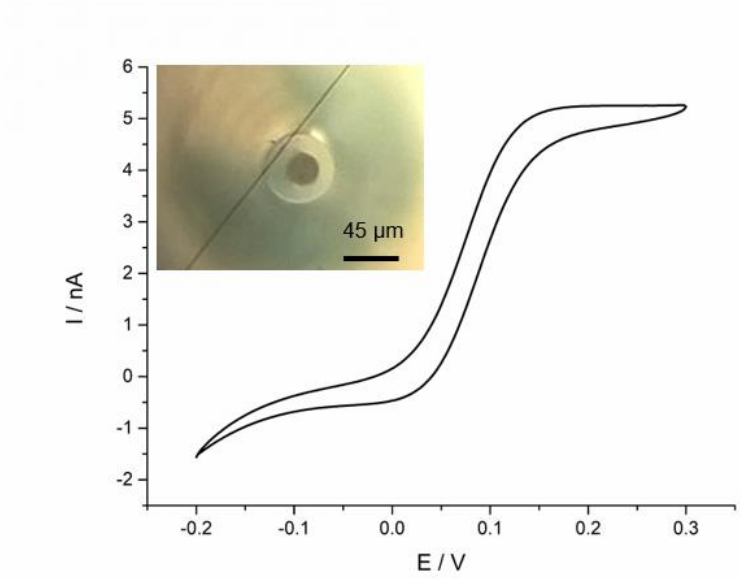

Figure 4.6.S1: Cyclic voltammogram using a SECM probe with a diameter of 25 µm (1.5 mM FcMeOH with 0.2 M KNO_3, E_{start} = -0.2 V, E_{vertex} = 0.3 V, scan rate: 50 mV s^{-1}). Inset: Optical micrograph of the SECM probe.

References

[1] B.D. Agarwel, L.J. Broutman, K. Chandrarashekhara, Analysis an performance of fiber composites, 3rd edition, John Wiley & Sons, 2006

[2] Q. Zhang, The "Black Revolution" of sports equipment: Application of carbon fiber reinforced plastics (CFRP), AMM. 440 (2013) 69–73.

[3] I.P.T. Rajakumar, P. Hariharan, L. Vijayaraghavan, Drilling of carbon fibre reinforced plastic (CFRP) composites - a review, Int. J. Mater. Prod. Technol. 43 (2012) 43.

[4] S. Ebnesajjad, A.H. Landrock, Adhesives technology handbook, 3rd edition, William Andrew, 2014.

[5] R. Wiesendanger, Scanning probe microscopy and spectroscopy: methods and applications, Cambridge University Press, Cambridge, 1994.

[6] G. Binnig, C.F. Quate, Atomic force microscope, Phys. Rev. Lett. 56 (1986) 930–933.

[7] D. Leckband, J. Israelachvili, Intermolecular forces in biology, Q. Rev. Biophys. 34 (2001) 105–267.

[8] S.S. Nair, S. Wang, D.C. Hurley, Nanoscale characterization of natural fibers and their composites using contact-resonance force microscopy, Compos. Part A 41 (2010) 624–631.

[9] U. Dürig, A. Stalder, Adhesion on the nanometer scale, in: Physics of sliding friction, Springer Netherlands, Dordrecht, 1996, 299–323.

[10] S. Raman, T. Utzig, T. Baimpos, B. Ratna Shrestha, M. Valtiner, Deciphering the scaling of single-molecule interactions using Jarzynski's equality, Nat. Commun. 5 (2014) 5539.

[11] M.P. Boneschanscher, J. Van Der Lit, Z. Sun, I. Swart, P. Liljeroth, D.

Vanmaekelbergh, Quantitative atomic resolution force imaging on epitaxial graphene with reactive and nonreactive AFM probes, ACS Nano 6 (2012) 10216–10221.
[12] D.S. Wastl, A.J. Weymouth, F.J. Giessibl, Atomically resolved graphitic surfaces in air by atomic force microscopy, ACS Nano 8 (2014) 5233–5239.
[13] E.V. Dubrovin, M. Schächtele, D.V. Klinov, T.E. Schäffer, Time-lapsed single biomolecule atomic force microscopy investigation on modified graphite in solution, Langmuir 33 (2017) 10027-10034.
[14] J. Kwak, A.J. Bard, Scanning electrochemical microscopy. Theory of the feedback mode, Anal. Chem. 61 (1989) 1221–1227.
[15] S. Bergner, J. Wegener, F.-M. Matysik, Simultaneous imaging and chemical attack of a single living cell within a confluent cell monolayer by means of scanning electrochemical microscopy, Anal. Chem. 83 (2011) 169–174.
[16] S. Bergner, P. Palatzky, J. Wegener, F.-M. Matysik, High-resolution imaging of nanostructured Si/SiO_2 substrates and cell monolayers using scanning electrochemical microscopy, Electroanalysis 23 (2011) 196–200.
[17] P. Vatsyayan, C. Iffelsberger, C.C. Mayorga, F.-M. Matysik, Imaging of localized enzymatic peroxidise activity over individual unbiased gold nanowires by scanning electrochemical microscopy, Anal. Methods 8 (2016) 6847–6855.
[18] A.J. Bard, M.V. Mirkin, Scanning electrochemical microscopy, 2nd edition,CRC Press, Boca Raton, 2012.
[19] M.A. Mezour, R. Cornut, E.M. Hussien, M. Morin, J. Mauzeroll, Detection of hydrogen peroxide produced during the oxygen reduction reaction at self-assembled thiol-porphyrin monolayers on gold using SECM and nanoelectrodes, Langmuir 26 (2010) 13000–13006.
[20] C. Lefrou, R. Cornut, Analytical expressions for quantitative scanning electrochemical microscopy (SECM), Chemphyschem. 11 (2010) 547–56.
[21] D. Polcari, P. Dauphin-Ducharme, J. Mauzeroll, Scanning electrochemical microscopy: A comprehensive review of experimental parameters from 1989 to 2015, Chem. Rev. 116 (2016) 13234–13278.
[22] J. Thomason, D. Dwight, The use of XPS for characterisation of glass fibre coatings, Compos. Part A 30 (1999) 1401–1413.
[23] R. Tao, M. Alfano, G. Lubineau, Laser-based surface patterning of composite plates for improved secondary adhesive bonding, Compos. Part A 109 (2018) 84–94.
[24] A.C. Prickett, P.A. Smith, J.F. Watts, ToF-SIMS studies of carbon-fibre composite fracture surfaces and the development of controlled mode in situ fracture, Surf. Interface Anal. 31 (2001) 11–17.
[25] S. Grunder, S. Schmatloch, A. Lutz, Polyurethanklebstoffe zum Kleben von Kunststoffen, in: Kunststoffe erfolgreich kleben, Springer Fachmedien Wiesbaden, Wiesbaden, 2018: pp. 189–206.
[26] B. Müller, W. Rath, Formulierung von Kleb- und Dichtstoffen, Vincentz Network, Hannover, 2004.
[27] W.J. Blank, Z.A. He, E.T. Hessell, Catalysis of the isocyanate-hydroxyl reaction by non-tin catalysts, Prog. Org. Coat. 35 (1999) 19–29.
[28] A. Noy, D. V. Vezenov, C.M. Lieber, Chemical force microscopy, Annu. Rev. Mater. Sci. 27 (1997) 381–421.
[29] V. Oliveira, S.P. Sharma, M.F.S.F. de Moura, R.D.F. Moreira, R. Vilar, Surface treatment of CFRP composites using femtosecond laser radiation, Opt. Lasers Eng. 94 (2017) 37–43.

5. Summary

The fabrication of high-quality ultramicroelectrodes (UME) was a prerequisite for a variety of scanning electrochemical microscopic (SECM) experiments carried out in this thesis. UMEs with diameters ranging from 1 to 25 µm with a thin soda lime glass insulation (RG 2-20) and desired electrochemical properties were routinely fabricated to accomplish these targets.

Further, for the imaging of the reactive oxygen species (ROS) generated during electrochemical oxygen evolution reaction (OER), the formation of transient diffusion layers during electrochemical reactions at large substrates was one major limitation. To overcome this limitation the well-known advantages of convective mass transport in electrochemical systems were exploited. After the integration of a high-precision stirring device into the experimental setup, the well-defined stirring led to steady-state diffusion layer characteristics near large substrate electrodes operated as generator electrodes. The imaging of the electrochemical hydrogen evolution at a 2 mm Pt disk electrode in the substrate generation/tip collection (SG/TC) mode demonstrated that SECM with forced convection increases the amount of obtained information. The added complexity of hydrodynamic methods in the theoretical description and construction of devices with known and reproducible mass transport conditions were addressed with numerical simulations. The reliability of the simulation was verified numerically and experimentally. The simulation showed that the rotation of the cylindrical stirrer resulted in a laminar convection near the substrate electrode. The flow profile within the liquid depended on the rotational speed of the stirrer. This enabled the formation of steady-state diffusion layers with a defined layer thickness. The constructed numerical model paves the way for additional numerical studies involving other cell and substrate geometries. The combination with other simulation modules (e.g.: electrochemistry) could provide interesting and valuable information for future applications.

Hydrodynamic SECM further enabled the detection and imaging of the production of ROS at Pt and boron-doped diamond (BDD) macroelectrodes during OER. The combination of the tip-substrate voltammetry with forced convection resulted in a measurement principle similar to the rotating ring disk electrode and enabled the detection of ROS at BDD and Pt. Imaging in hydrodynamic SG/TC mode revealed that both, H_2O_2 and another reducible ROS species, are produced simultaneously at different domains depending on the local boron content of the surface.

These pioneering experiments established the advantage of hydrodynamic SECM for locally resolved studies of highly reactive species produced during electrochemical gas evolution reaction. The increased amount of accessible analytical information aids toward a better understanding of electrochemical processes. The application of SECM in combination with forced convection to other heterogeneous reactions could help to expand the knowledge in other scientific fields and opens the door for new applications.

In addition, the high-resolution SECM was used to image individual gold nanowires (AuNWs) immobilized on glass and gold coated glass slides in negative and positive feedback modes, respectively. Later the enzymatic peroxidase activity of immobilized horseradish peroxidase on individual AuNWs was imaged. These images revealed a higher enzymatic activity located at the ends of the AuNWs. This work can be further extended for the characterization of other novel nanomaterials and to study their redox behavior alone or in combination with other redox enzymes.

In another work, SECM was used to provide complementary information in combination with the atomic/chemical force microscopy to evaluate the surface characteristics of pretreated carbon fiber reinforced plastics (CFRP). SECM images revealed the exposure of carbon fiber strands and delivered additional information about the chemical and morphological structure of the pretreated CFRP.

6. Zusammenfassung in deutscher Sprache

Die Herstellung von hochwertigen Ultramikroelektroden (UME) war eine Voraussetzung für eine Vielzahl der in dieser Arbeit durchgeführten Experimente mit dem elektrochemischen Rastermikroskop (SECM). Die benötigten UMEs wurden routinemäßig mit Durchmessern von 1 bis 25 µm, mit einer dünnen Isolierung (RG 2-20) aus Kalk-Natron-Glas und den gewünschten elektrochemischen Eigenschaften hergestellt.

Für die Abbildung von reaktiven Sauerstoffspezies (ROS), die während der elektrochemischen Sauerstoffentwicklungsreaktion (OER) erzeugt werden, war die Bildung transienter Diffusionsschichten während der elektrochemischen Reaktionen an großen Substratelektroden einschränkend. Um diese Einschränkung zu überwinden wurden die bekannten Vorteile des konvektiven Stofftransports genutzt. Nach der Integration eines hoch Präzision Rührers in den Versuchsaufbau führte das wohldefinierte Rühren zu einer stationären Diffusionsschicht in der Nähe von großen Substratelektroden, die als Generatorelektroden betrieben wurden. Die Abbildung der elektrochemischen Wasserstoffentwicklung an einer 2 mm Scheibenelektrode aus Pt im Messmodus Substratgenerierung/Spitzensammlung (SG/TC) zeigte, dass das SECM in Kombination mit forcierter Konvektion die Menge an erhaltenen Information erhöht. Die zusätzliche Komplexität hydrodynamischer Methoden bei der theoretischen Beschreibung und Konstruktion von Bauelementen mit bekannten und reproduzierbaren Stofftransport-bedingungen wurde mit numerischen Simulationen untersucht. Die Zuverlässigkeit der Simulation wurde numerisch und experimentell verifiziert. Die Simulation zeigte, dass die Rotation des zylindrischen Rührers zu einer laminaren Konvektion in der Nähe der Substratelektrode führte. Das Strömungsprofil in der Flüssigkeit hing von der Drehzahl des Rührers ab. Dies ermöglichte die Bildung von stationären Diffusionsschichten mit einer definierten Schichtdicke. Das konstruierte Modell ebnet den Weg für weitere numerische Studien mit anderen Zell- und Substratgeometrien. Die Kombination mit anderen Simulationsmodulen (z.B. für die Elektrochemie) könnte interessante und wertvolle Informationen für zukünftige Anwendungen liefern.

Das hydrodynamische SECM ermöglichte ferner die Detektion und Abbildung der Produktion von ROS an Pt- und Bor-dotierten Diamant (BDD) Makroelektroden während der OER. Die Kombination der Spitze-Substrat-Voltammetrie mit der forcierten Konvektion führte zu einem Messprinzip ähnlich der rotierenden Ringscheibenelektrode und ermöglichte die Detektion von

ROS an BDD und Pt. Die Abbildung im hydrodynamischen SG/TC-Modus zeigte, dass sowohl H_2O_2 als auch eine weitere reduzierbare ROS-Spezies in Abhängigkeit vom lokalen Borgehalt der Oberfläche gleichzeitig an unterschiedlichen Domänen erzeugt werden.

Diese bahnbrechenden Experimente haben den Vorteil des hydrodynamischen SECM für lokal aufgelöste Untersuchungen von hochreaktiven Spezies, die während der elektrochemischen Gasentwicklungsreaktion erzeugt werden, aufgezeigt. Die zusätzlichen analytischen Informationen helfen dabei elektrochemische Prozesse besser zu verstehen. Die Anwendung des SECM in Kombination mit forcierter Konvektion für andere heterogene Reaktionen könnte helfen, das Wissen in anderen wissenschaftlichen Bereichen zu erweitern und die Tür für neue Anwendungen zu öffnen.

Darüber hinaus wurde das SECM dazu verwendet einzelne Goldnanodrähte (AuNWs), die auf Glasobjektträgern und auf Goldbeschichteten Glasobjektträgern immobilisiert wurden, mit negativer bzw. positiver Rückkopplung hochauflösend abzubilden. Später wurde die enzymatische Aktivität von immobilisierter Meerrettich-Peroxidase auf einzelnen AuNWs abgebildet. Diese Bilder zeigten eine höhere enzymatische Aktivität an den Enden der AuNWs. Diese Arbeit kann für die Charakterisierung anderer neuartiger Nanomaterialien erweitert werden, um ihr Redoxverhalten allein oder in Kombination mit anderen Redoxenzymen zu untersuchen.

In einer weiteren Arbeit wurde das SECM dazu verwendet, um ergänzende Informationen über die Oberflächeneigenschaften von vorbehandelten kohlenstofffaserverstärkten Kunststoffen (CFRP) in Kombination mit der atomaren/chemischen Kraftmikroskopie zu liefern. SECM Bilder zeigten die Exposition von einzelnen Kohlenstofffasersträngen und lieferten zusätzliche Informationen über die chemische und morphologische Struktur des vorbehandelten CFRP-Substrats.

Erklärung

Ich habe die Arbeit selbstständig verfasst, keine anderen als die angegebenen Quellen und Hilfsmittel benutzt und bisher keiner anderen Prüfungsbehörde vorgelegt. Von den in § 27 Abs. 5 vorgesehenen Rechtsfolgen habe ich Kenntnis genommen.

Regensburg, den 14. Juni 2018

……..
(Christian Iffelsberger)